UQAC
Université du Québec
à Chicoutimi

# Solidification of hypoeutectic Al-Si alloys during high-pressure vacuum die-casting (HPVDC) of thin-walled components & the influence of subsurface microstructure variations on bending ductility

**By Xavier Tremblay**

**A thesis submitted to the University of Québec at Chicoutimi in partial fulfilment of the requirements for a Master's degree in engineering (research profile)**

Québec, Canada

# RÉSUMÉ

Le moulage sous haute pression (*HPDC*) est largement utilisé dans l'industrie automobile en raison de sa capacité à produire en masse des pièces complexes en aluminium à parois minces, y compris de grands composants structurels fabriqués à partir d'alliages spécialisés. Cependant, les vitesses de solidification rapides impliqués dans ce procédé entraînent une micro-ségrégation localisée des éléments d'alliage. L'analyse de la microstructure a révélé que la fraction eutectique Al-Si s'écarte des prédictions obtenues avec les modèles de solidification les plus couramment utilisés (équilibre et de Scheil). De plus, la taille et la complexité des pièces coulées, associées à la compréhension actuelle du processus de solidification rapide, limitent le contrôle de la microstructure. En particulier, l'écoulement rapide et turbulent de la matière pendant le remplissage entraîne la formation de variantes distinctes de la microstructure de surface, souvent visibles au sein d'une même pièce.

Premièrement, pour traiter la déviation de la fraction eutectique, nous proposons une équation de Scheil modifiée. Ce modèle actualisé incorpore des coefficients de partition dépendant de la vitesse du front de solidification de la phase primaire, offrant ainsi une représentation plus précise du comportement de la microségrégation et de la fraction eutectique. La microstructure a été caractérisée à l'aide de la microscopie optique sur des spécimens représentatifs, ce qui a permis d'évaluer proportion d'eutectique des composants. La fraction eutectique moyenne de ces échantillons a ensuite été utilisée pour étalonner le modèle proposé. Les résultats indiquent que la vitesse du front de solidification influence de manière significative la fraction du constituant primaire. De plus, l'analyse par microscopie optique suggère que l'exclusion des constituants se solidifiant en dehors de la cavité du moule des calculs de fraction de phase conduit à une évaluation plus précise de la fraction eutectique. L'intégration de cette relation de Scheil modifiée dans les simulations de solidification pourrait permettre d'améliorer les capacités à prédire la microstructure des matériaux pour le HPDC.

Deuxièmement, étant donné que la ductilité en flexion est un indicateur de performance clé pour les pièces moulées à haute intégrité, et qu'elle est généralement influencée par la microstructure proche de la surface, cette étude vise à caractériser les variations de microstructure observées dans les échantillons d'aluminium moulés sous pression, à évaluer leur impact sur le comportement local en pliage et à comprendre leurs conditions de formation. Les variations de la microstructure ont été caractérisées à l'aide de la microscopie optique sur des spécimens représentatifs, qui ont révélé des variantes distinctes de la microstructure de surface. Des échantillons présentant chacune des variantes de microstructure de surface identifiées ont été soumis à des essais de flexion VDA afin d'évaluer leurs performances mécaniques. Les essais mécaniques ont démontré que les variantes de la microstructure sous la surface affectent effectivement le comportement en pliage.

Ces résultats soulignent l'importance d'une compréhension plus approfondie des mécanismes impliqués dans le processus de remplissage et de solidification rapide, ce qui pourrait conduire à des améliorations dans les pratiques de conception des moules. En outre, ces connaissances pourraient permettre de contrôler la formation et distribution des constituants de la microstructure ainsi que d'améliorer l'homogénéité globale des propriétés mécaniques des composants produits par moulage haute pression (HPDC).

# ABSTRACT

High-pressure die casting (HPDC) is widely used in the automobile industry due to its ability to mass-produce complex aluminum parts, including large thin-walled structural components made from specialized alloys. However, the rapid solidification rates involved in this process result in localized microsegregation of alloying elements. Microstructural analysis reveals that the Al-Si eutectic fraction deviates from predictions made by traditional equilibrium and Scheil models. Furthermore, the size and complexity of the castings, coupled with the current understanding of the rapid solidification process, limit the control over the microstructure. Specifically, the fast, turbulent material flow during filling leads to the formation of distinct subsurface microstructure variants, often visible within a single casting.

Firstly, to address the deviation in eutectic fraction, we propose a modified Scheil equation. This updated model incorporates velocity-dependent partition coefficients at the solidification front, offering a more accurate representation of both microsegregation behavior and the eutectic fraction. Secondly, given that bending ductility is a key performance indicator for high-integrity castings, and is typically influenced by near-surface microstructure, this study aims to characterize the observed microstructure variations in die-cast aluminum specimens and evaluate their impact on local bending behavior.

Microstructure variations were characterized using optical microscopy on representative, small-scale die-cast specimens, which revealed distinct subsurface microstructure variants. The average eutectic fraction of these specimens was then used to calibrate the proposed model. Samples from regions exhibiting different subsurface microstructure variants underwent VDA bending tests to evaluate their mechanical performance.

Optical microscopy analysis suggests that excluding constituents solidifying outside the die cavity from phase fraction calculations leads to a more accurate evaluation of the eutectic fraction. Additionally, the results indicate that melt front velocity significantly influences the volume fraction of the primary constituent. By integrating this modified Scheil relationship into solidification simulations, the capabilities of integrated computational materials engineering for HPDC can be enhanced.

Mechanical testing demonstrated that subsurface microstructure variants do, indeed, affect bending behavior. These findings underscore the importance of a deeper understanding of the mechanisms involved in the filling process, which could lead to improvements in die design practices. Furthermore, this knowledge could aid in controlling microstructure formation and enhance the overall homogeneity of mechanical properties throughout HPDC components.

# TABLE OF CONTENTS

# LIST OF TABLES

# LIST OF FIGURES

# LIST OF ABBREVIATIONS

| | |
|---|---|
| Al | Aluminium |
| $\alpha$-Al | Primary aluminium phase |
| CFD | Computational fluid dynamics |
| ESC | Externally solidified crystal |
| HPDC | High Pressure Die-Casting |
| HPVDC | High pressure vacuum die-casting |
| KGT model | Kurz-Giovanola-Trivedi model |
| PI | Pressure intensification |
| RSP | Rapid solidification process |
| SDAS | Secondary dendrite arms spacing |
| SFV | Solidification front velocity |
| Si | Silicon |
| SLM | Selective laser melting |
| VDA | Verband der automobilindustrie |
| VOF | Volume of fluid |

# ACKNOWLEDGMENTS

I wish to acknowledge the opportunity that was given to me by my directors Alexandre Gariépy and Mousa Javidani. I appreciate the trust and confidence you showed in my competence to lead this project in a promising direction. This experience helped me a lot to progress both personally and professionally.

I would like to extent my appreciation to Roghayeh (Layla) Mohammadzadeh and Ali Eliashery for their time and support along the way, as well as Alexandre Morin, Keven Lepage-Potvin and Myriam Poliquin for their help with the experimental work. Lastly, I want to thank the National Research Council for providing the HPDC components necessary to make this project possible.

# INTRODUCTION

High-pressure die casting (HPDC) is a widely used method for producing aluminium products, particularly automotive components made from Al-Si-based alloys [1, 2]. Production of net-shape high integrity components require a good control on solidification. However, it is well known that during the solidification of Al alloys in HPDC, alloying elements are often unevenly distributed at different length scales, resulting in a wide range of microstructural features within a single component. While the microstructure of Al-Si-based alloys has been extensively studied, in-situ experimental observations within casting cells remain both challenging and costly, making it difficult to accurately describe, quantify or predict the local solidification conditions that lead to the highly heterogeneous microstructure. Moreover, the formation of the microstructure—particularly the kinetics of phase transformation during rapid solidification processes like HPDC—is not yet fully understood. In structural applications, this heterogeneous microstructure plays a crucial role in determining the mechanical properties of the components [3-6]. Therefore, gaining a better understanding of microstructure formation and its impact on mechanical performance is essential to continually improve product quality even as complexity increases.

In hypoeutectic Al-Si die-cast alloys, the primary constituents typically include externally solidified crystals (ESCs), the primary aluminum phase (α-Al), and the eutectic. While the α-Al phase and eutectic constituents solidify within the die cavity, ESCs form in the shot sleeve before injection, as the material is shoved by the plunger [7]. Additionally, the material flow during the HPDC process generates a layered microstructure, generally consisting of three distinct regions: the core, the segregation bands, and the skin layer. These regions can typically be distinguished based on the distribution of their main constituents. Despite local variations, microstructural characterization of hypoeutectic Al-Si and Al-Mg alloys in previous studies has shown that solidification under these conditions can result in a considerably lower eutectic fraction than predicted by conventional solidification models (e.g., equilibrium and Scheil models) [8]. As a result, it is challenging to accurately predict and control the microstructure observed in HPDC. In practice, the addition of other alloying elements will lead to the formation of intermetallic, and the microstructure will present porosities. However, both features have not been studied in this project.

The first objective of this project is therefore to investigate rapid solidification theories and models, with the aim of adapting the conventional equilibrium phase diagram to better predict the proportions of the main constituents and align more closely with observations in HPDC components. As thermodynamic calculations can be quite complex, an easily applicable solution is required for this problematic. The results of the proposed model will be compared with experimental eutectic fractions from two different castings made of two different hypoeutectic Al-Si based alloys. As one alloy will be used to calibrate the model and the other for validation purposes.

A common requirement for structural castings, particularly in terms of crashworthiness and self-piercing riveting capability, is bendability, which is often evaluated using tests such as the VDA bend test [9]. Since this test primarily concentrates strain on the surface, it is likely that the skin layer plays a critical role in determining this aspect of service performance.

As a result, the second objective of this project is to investigate how microstructure variations in HPDC thin-walled components affect bending ductility. Specifically, the experimental work aims to characterize microstructure variations in a simple prototype casting, focusing on the distribution of the main constituents within the plate and, in particular, the skin layer. The goal is to correlate bending performance with local microstructural characteristics. Despite the simplicity of the components used, efforts are being made to scale to real-life geometrical complexity.

The first chapter of this document provides a comprehensive literature review on both conventional and rapid solidification models, along with an in-depth analysis of the various stages of the High-Pressure Die Casting (HPDC) process and their impact on microstructure formation. The following chapters describe the methodology, present the results corresponding to the two primary objectives of this project as well as an in-depth analysis of the results in relation to the mechanism involved during the solidification process. Lastly, conclusions resulting from this project will be presented with recommendation regarding future work on this subject.

# CHAPTER 1
# LITERATURE REVIEW

## 1.1 BASICS OF SOLIDIFICATION

### 1.1.1 HEAT EXTRACTION

The transformation of an alloy from its superheated liquid to the ambient temperature solid state involves the removal of heat from the system. Solidification is a process closely linked to enthalpy through:

1. Lowering the temperature (cooling) of a liquid or solid results in a decrease in enthalpy.
2. The phase transformation itself is accompanied by a decrease in enthalpy, a phenomenon known as the latent heat of solidification.

Heat extraction is achieved by applying appropriate cooling methods to the melt, which generates a heat flux ($\dot{q}$). It is important to note that heat extraction is directional, meaning it can be controlled to influence solidification patterns. This control affects the nucleation and growth direction of the solid phase (*Figure 1*) [10].

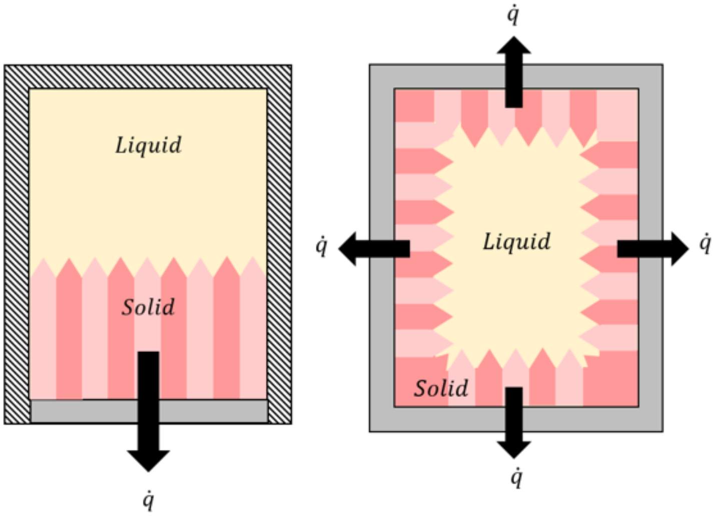

**Figure 1:** Schematic representation of the Influence of heat extraction direction on solidification

In the case of casting processes, the heat extraction rate is regulated by the mould material thermal properties, the geometry of the cavity and the temperature regulation of the mould. In practice, the mould cavity geometry is set by the part design and can influence the solidification process resulting in a suboptimal microstructure. In order to fix this problem, the mould temperature can be regulated with oil and/or water circuits. This way, it is possible to affect specific regions during solidification, resulting in a more uniform process. Finally, the regulation of the mould's temperature can be used to control the solidification patterns. As the medium temperature goes up, the resulting heat flux reduces, resulting in less heat extraction and longer solidification times of the material [11].

### 1.1.2 NUCLEATION

The formation of a new phase begins with the rearrangement of atoms, a process heavily influenced by the thermodynamic state of the system. Solidification starts when the system's temperature allows for the stabilization and survival of atomic clusters. Clusters that are too small to stabilize are referred to as embryos, while those large enough to persist are called nuclei (N).

For nucleation to occur, the liquid solution must first reach the equilibrium temperature ($T_E$, *Figure 2A*). Next, a certain degree of undercooling ($\Delta T$) is required to promote the agglomeration of atoms into clusters within the melt. When the appropriate clusters size and undercooling level are met, *Figure 2B* illustrates how the nucleation rate ($I$) quickly increases, leading to the formation of a stable nucleus colony. Once the temperature gets low enough, the nuclei in the melt enter the growth phase, eventually forming the grains of the final microstructure (*Figure 2C*).

As previously mentioned, nucleation requires a certain degree of undercooling to be applied to the melt. This is necessary because the small radius of curvature (r) of atomic-sized clusters creates a pressure difference between the solid and the melt. This pressure causes a reduction in the equilibrium temperature ($T_E$) by an amount $T_{E\Delta}$. The critical size ($r^{\circ}$) represents the minimum radius a cluster must have to achieve equilibrium with the melt at a given level of undercooling. Therefore, the relationship between the undercooling ($\Delta T$) and the critical size ($r^{\circ}$) is as follows:

$$r^{\circ} = \frac{2\sigma}{\Delta T * \Delta s_f}$$

Where $\sigma$ is the solid/liquid interface energy and $\Delta s_f$ is the entropy of fusion. This relation exposes that small amount of undercooling requires bigger crystals for nucleation to happen. Considering the cluster size depends on an arbitrary rearrangement of atoms in the melt, nucleation is less improbable for large critical radius.

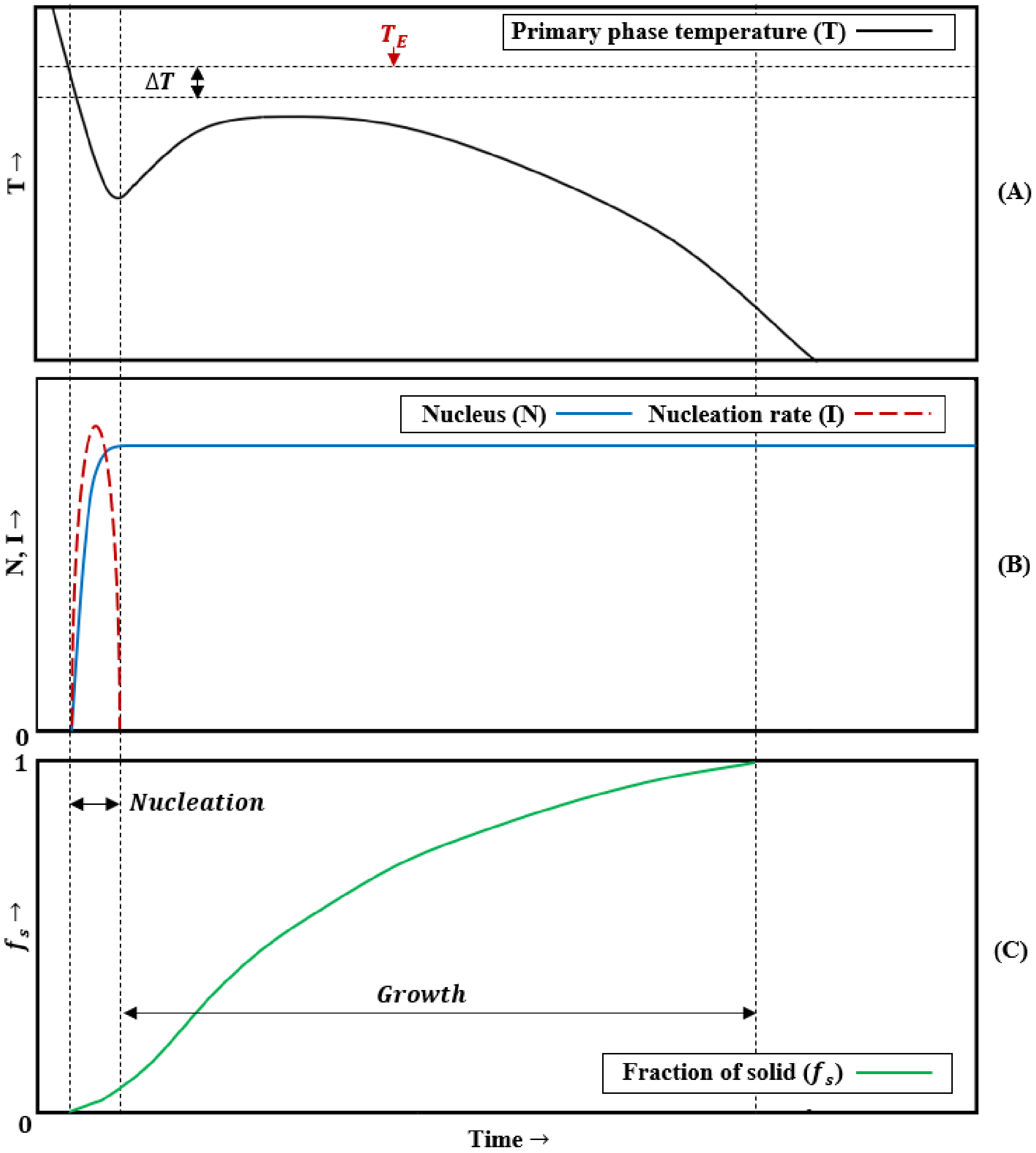

**Figure 2:** Thermal history of nucleation in the solidification process (single phase)

From a thermodynamic perspective, the nucleation of a crystal from its melt depends on the driving force, or the change in free energy ($\Delta G$, *Figure 3*), at the solid/liquid interface. This phenomenon is primarily governed by two processes:

1. Arbitrary thermal fluctuations that lead to the creation of embryos of various sizes ($\Delta G_v$).
2. The creation and cohesion of an interface between the melt and the embryo surface ($\Delta G_i$).

Assuming a spherical form for nucleus, the equation for the total free energy change at the interface is the following:

$$\Delta G = \Delta G_i + \Delta G_v = \sigma 4\pi r^2 + \frac{\Delta g 4\pi r^3}{3}$$

Where, $\Delta g$, the Gibbs free energy difference between the liquid and the solid per unit volume equals to:

$$\Delta g = -\Delta s_f (T_E - T) = -\Delta s_f \Delta T$$

For temperatures above equilibrium ($T > T_E$), *Figure 3A* shows that both the volume free energy ($\Delta G_V$) and the surface free energy ($\Delta G_i$) are positive, indicating that the formation of the solid phase is not energetically favorable. At the equilibrium temperature (*Figure 3B*), thermodynamic equilibrium exists between the solid and liquid phases ($\Delta G_V = 0$), but the surface free energy ($\Delta G_i$) remains unfavorable for nucleation. When the temperature drops below equilibrium (*Figure 3C*), the volume free energy term ($\Delta G_V$) becomes negative. As a result, or a given temperature, the total free energy ($\Delta G$) reaches a maximum ($\Delta G^{\circ}$) at the critical embryo size (r°). Once the embryo reaches this critical size, it becomes a nucleus, and its growth leads to a decrease in total free energy ($\Delta G$), which is energetically favorable for the system. As the system approaches the equilibrium temperature ($T_E$), fluctuations in energy may cause random addition or removal of atoms from the nucleus, resulting in a back-and-forth movement along the embryo size curve (r) (*Figure 4*). When a fluctuation results in the formation of a cluster of critical size (r°), the resulting decrease in total free energy ($\Delta G$) triggers nucleation and growth.

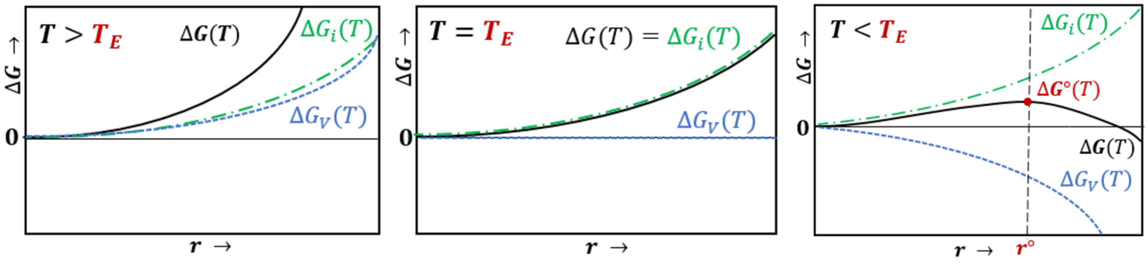

(A) (B) (C)

**Figure 3:** Free energy variation during the nucleation process

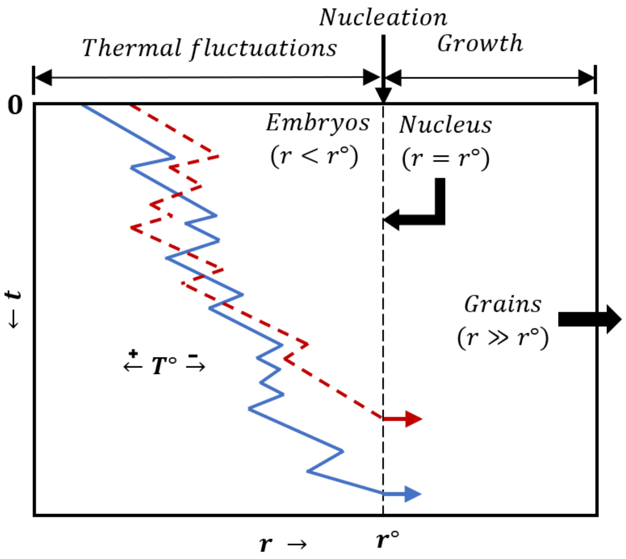

**Figure 4:** Thermal fluctuation leading to a change of the embryo's radius in the solidification process

### 1.1.3 GROWTH

After nucleation, the solidification process is driven by growth, which ultimately shapes the final microstructure and its properties. In nearly all alloy systems, solidification results in a microstructure that can be classified into two main constituent types: single-phase primary crystals and polyphase structures, such as eutectic or peritectic morphologies.

The primary constituent, composed of single-phase primary crystals, is typically a significant constituent of the microstructure for alloys outside the eutectic composition. In the case of Al-Si hypoeutectic alloys, the primary constituent results from dendritic growth of the face-centered cubic aluminium lattice. Dendrites are tree-like crystal structures that form as the nucleus grows. Furthermore, the size and growth direction of the dendrites are heavily influenced by the heat flux within the system.

The second group consists of a polyphase structure that arise from the eutectic reaction. These morphologies are characterized by the simultaneous growth of two distinct phases from the liquid. In systems undergoing a eutectic reaction, the final microstructure often consists of primary dendritic crystals surrounded by the eutectic phase.

**Dendrite morphology:**

Dendrites are tree-like structures that form when a crystal solidifies from its melt. Depending on the solidification conditions, dendrites develop branches of various orders. In practice, dendritic morphologies are characterized by the following properties:

1. Form (columnar or equiaxed)
2. The primary arm spacing ($\lambda_1$)
3. The secondary arm spacing ($\lambda_2$)

*Figure 5* illustrates the primary arm spacing ($\lambda_1$) and secondary dendrite arm spacing (SDAS, $\lambda_2$), which corresponds to the main trunk's diameter and distance between secondary branches. In addition to arm spacing, equiaxed dendritic crystals are often approximated to a sphere geometry and characterized by their diameter.

The primary arm spacing represents the size of the dendrite trunk, and the value measured in a solidified microstructure is the same as that formed during growth. In other words, the trunk size of a dendrite remains unchanged by further growth. In contrast, the secondary dendrite arm spacing (SDAS, $\lambda_2$) increases due to the curvature of the branched structure and its prolonged contact with the melt.

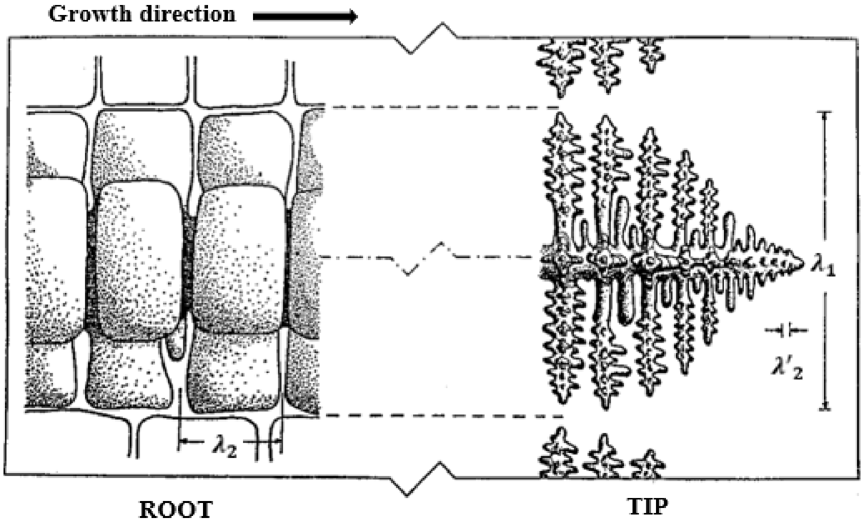

**Figure 5:** Dendritic structure representation [10]

**Dendritic growth:**

As mentioned previously, the direction of dendrite growth is heavily influenced by the direction of the heat flow. When a directional heat flow is imposed on the system (or melt), constrained (or columnar, or directional) growth occurs. In this scenario, the growth direction is opposite to the direction of heat flow. Additionally, the intensity of the heat flow affects the dendrite tip growth velocity.

In regions influenced by directional growth, the grain boundaries are aligned parallel to the dendrite trunks and remain continuous throughout the affected zone.

As heat flows from the crystal to the melt, the process is referred to as unconstrained growth or equiaxed solidification. In this case, the dendrites can grow freely in a radial, six-fold morphology, growing as quickly as the imposed undercooling allows. This free growth phase continues until the dendrites begin to impinge on those originating from other nuclei. Once solidification is complete, the grain boundaries form a continuous network throughout the solid.

In practice, conventional casting products may exhibit both columnar and equiaxed dendrites. At the start of solidification, the undercooled mold wall induces the nucleation of smaller equiaxed crystals, forming a skin layer. From this layer, as shown in *Figure 6*, crystals with the most favorable orientation will overgrow the others, eventually forming the columnar dendritic zone. The growth of the columnar dendrites continues until the melt loses its superheat and becomes slightly undercooled. At this point, equiaxed growth resumes until the melt is fully solidified.

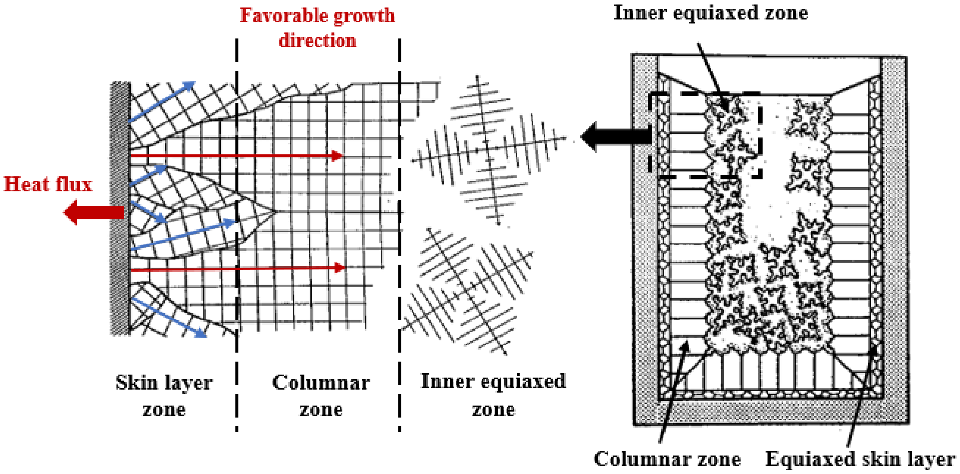

**Figure 6:** Dendritic microstructure formation resulting from conventional casting processes [10]

**Eutectic growth:**

The microstructure of alloys with compositions within the eutectic range typically consists of two main constituents. The primary constituent, which is dendritic for Al-Si hypoeutectic alloys, solidifies first. The second constituent, the eutectic phase, fills the "free space" between the trunks and arms of the dendrites (*Figure 7*).

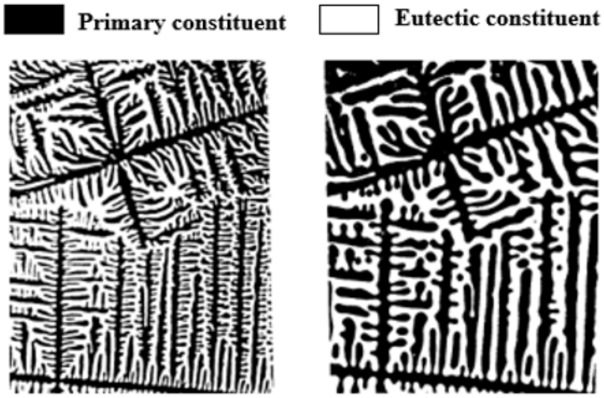

**Figure 7:** Representation of the dendritic and eutectic constituents [10]

The key characteristic of the eutectic solidification process is the simultaneous growth of two phases from the liquid (L → α + β). As a result, eutectic morphologies can exhibit various geometric arrangements. When both phases are present in approximately equal volume fractions ($f_s \cong 50\%$), a lamellar structure is typically formed (*Figure 8A*). However, when one phase is present in a lower proportion than the other, the less abundant phase will exhibit fibrous growth (*Figure 8B*). In addition to phase proportions, the entropy of fusion ($\propto$) also influences the eutectic morphology. If both phases have a low entropy of fusion, the eutectic forms a regular structure. Conversely, if one phase has a high entropy of fusion, its fibers become faceted, leading to an irregular eutectic morphology.

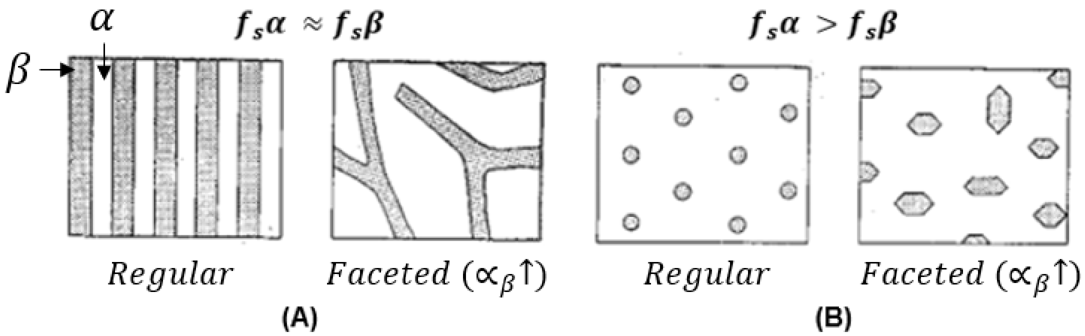

**Figure 8:** Types of binary eutectic morphologies [10]

### 1.1.4 Al-Si EQUILIBRIUM BINARY PHASE DIAGRAM (2D)

This chapter introduces phase diagrams by explaining the fundamentals of binary systems. As the name suggests, binary systems are used to describe the phases of an alloy composed of two soluble metals. To construct a complete phase diagram, three external variables must be considered: pressure, temperature, and composition. The resulting three-dimensional space, as illustrated in *Figure 9A*, allows for the determination of the phases present in the system for a given set of independent variables [12].

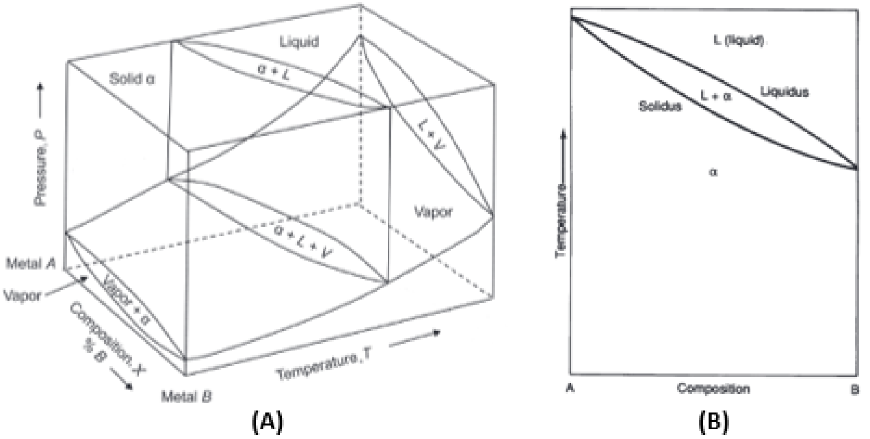

**Figure 9:** (A) Full phase diagram representation and (B) Typical Temperature-Composition binary phase diagram [12]

In practice, pressure is often assumed to be constant at 1 atm. As a result, the phase diagram is typically represented as a 2D cross-section, illustrating the phase relationships in alloys composed of metals A and B at normal pressure [13]. On the other hand, HPDC involves very high transient pressures on the other of 40 to 120 MPa during part of the solidification time. In the case of the Al-Si system, pressure of this order of magnitude only slightly increases the eutectic temperature and the solubility of the solute element [14], and the phase diagram at normal pressure is generally used. The phase diagram for the solidification of a binary alloy is highly dependent on the nature of the two metals involved. For example*, Figure 9B* depicts an isomorphous system, which is typical for metals that are completely soluble in each other. However, most metals are not fully soluble in all proportions, meaning that most phase diagrams involve more complex solidification reactions. *Table 1* outlines the known binary reactions, but this work specifically focuses on the eutectic reaction, as it is a key feature of the Al-Si system.

**Table 1:** Possible transformation reactions in binary alloy systems [13]

| Name | General Form | Diagram Form |
|---|---|---|
| Eutectic | $Liquid \rightleftharpoons Solid_1 + Solid_2$ | 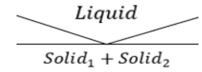 |
| Eutectoid | $Solid_1 \rightleftharpoons Solid_2 + Solid_3$ | 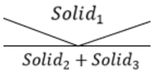 |
| Monotectic | $Liquid_1 \rightleftharpoons Liquid_2 + Solid$ | 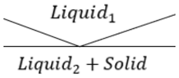 |
| Peritectic | $Liquid + Solid_1 \rightleftharpoons Solid_2$ | 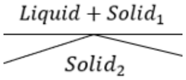 |
| Peritectoid | $Solid_1 + Solid_2 \rightleftharpoons Solid_3$ | 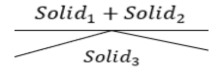 |

**Interpretation of the equilibrium phase diagram for an isomorphous system:**

A binary isomorphous system is one in which two metals are completely soluble in all proportions and states. Typically, the metals in such a system share the same crystalline structure and have similar atomic radii. Isomorphous systems are represented by two points and two curves, as shown in *Figure 10*. The two points, $T_A$ and $T_B$, correspond to the solidification temperatures of the pure metals A and B, respectively. The left and right axes of the diagram represent the unary systems for the solidification of the pure metals, while the x-axis (abscissa) indicates the composition of the alloy in terms of the percentage of metal B. The upper curve, known as the liquidus, marks the beginning of solidification (or end of fusion), while the lower curve, the solidus, indicates the end of solidification. The area above the liquidus represents a monophasic liquid solution, while the area below the solidus represents a monophasic solid solution. The region between the liquidus and solidus is a biphasic zone, consisting of both a solid solution and a liquid solution, with each phase having a unique composition of metals A and B [13]. It is crucial to understand how to interpret the information contained in a phase diagram. At first glance, and as the name suggests, a phase diagram reveals all the possible phases of a given alloy across a range of compositions and temperatures. Additionally, it can be used to determine the relative quantities of phases present at equilibrium in an alloy with a specified composition and temperature. This capability allows for the analysis of phase and composition changes during the solidification process of an alloy with a known overall composition.

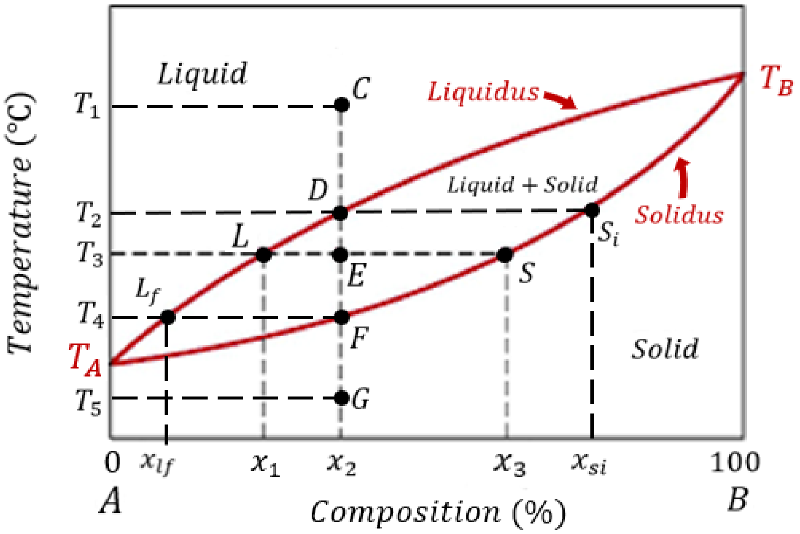

**Figure 10:** Example of an isomorphous binary phase diagram

The main use for phase diagrams is to characterize the proportions and compositions of phases along a specific solidification path. For example, let us detail the solidification of an alloy of composition $x_2$ along the solidification path C→G, as shown in *Figure 10*.

***State C:*** Consider an alloy composed of metals A and B with a composition of $x_2$. At temperature $T_1$, we can determine that the alloy exists in a monophasic liquid solution state with a nominal composition of $x_2$. This holds true for any point above the liquidus curve.

***State D:*** The monophasic state of the alloy remains unchanged until temperature $T_2$ is reached. At this point, the alloy crosses the liquidus line, and solidification begins. The composition of the first solid, $x_{Si}$, is determined at the intersection of a horizontal line $(D - S_i)$ at temperature $T_2$ and the solidus curve. This principle, known as the lever rule, is crucial for determining phase proportions in alloys under equilibrium conditions, particularly when multiple phases are present.

***State E:*** At this stage of solidification, the alloy is in the biphasic domain, meaning it consists of both a liquid solution and a solid solution. By applying the lever rule at temperature $T_3$, the compositions of both phases ($x_1$ and $x_3$) can be determined at the intersections of the tie-line $L \rightarrow S$ with the liquidus and solidus curves.

In the biphasic domain, the lever rule can also be used to calculate the proportion of each phase. If the $L \rightarrow S$ segment represents 100% of the phases at $T_3$, the phase proportions can be determined as follows:

$$Liquid\ (\%) = \frac{E \rightarrow S}{L \rightarrow S} \times 100 = \frac{x_3 - x_2}{x_3 - x_1} \times 100$$

$$Solid\ (\%) = \frac{L \rightarrow E}{L \rightarrow S} \times 100 = \frac{x_2 - x_1}{x_3 - x_1} \times 100$$

***State F:*** At this point, the remaining liquid phase is about to completely solidify. The same principle can be applied to determine the final composition of the liquid phase. Specifically, at temperature $T_4$, just before crossing the solidus line, the horizontal line ($L_f \rightarrow F$) indicates that the composition of the liquid phase is $x_{if}$.

**State G:** At temperatures lower than $T_4$, we can assume that the liquid phase has fully solidified. As a result, the alloy is now a homogenous monophasic solid solution with a nominal composition of $x_2$.

**Eutectic reaction:**

Eutectic reactions occur in alloys composed of two elements that are fully soluble in the liquid state but have limited solubility in the solid state. In a eutectic system, adding either component metal lowers the melting point below that of the pure elements. The melting point decreases until the liquidus curve reaches a temperature minimum, known as the eutectic point, as illustrated in the Al-Si system shown in *Figure 11* [15]. At the eutectic composition ($x_E$), the liquidus and solidus curves coincide. As a result, when the system reaches the eutectic temperature ($T_E$), the liquid phase undergoes an isothermal solidification resulting in eutectic constituent [13]. The general eutectic reaction can be represented as follows:

$$Liquid \rightleftharpoons Solid\ \alpha + Solid\ \beta$$

The result is a fine mix of two immiscible solid phases (the eutectic) of compositions corresponding to the extremities of the isotherm. Alloys that have a lower composition than the eutectic ($x_E$) are called hypoeutectic, as opposed to hypereutectic for higher compositions. In these cases, solidification will start before the eutectic temperature. For that reason, the final microstructure for these compositions presents primary and eutectic constituents [15].

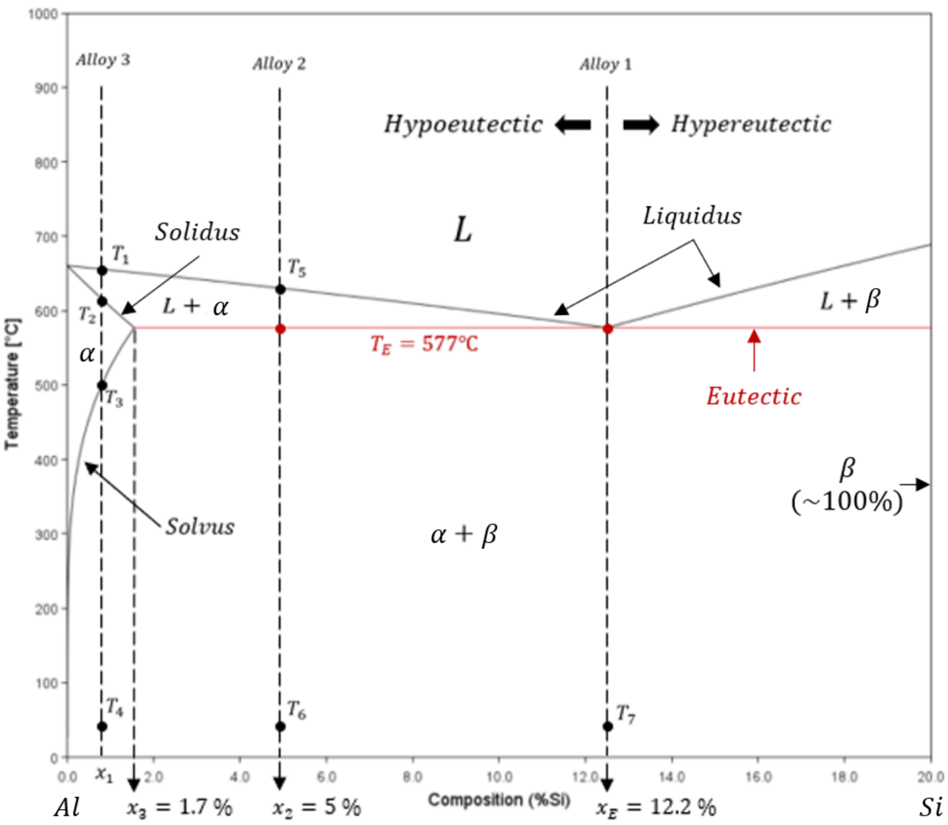

**Figure 11:** Aluminium-Silicon (Al-Si) binary phase diagram (Produced with ThermoCalc and adapted)

To fully understand the eutectic reaction phase diagram, the solidification paths shown in *Figure 11* are explained in detail. Alloy 1 represents an alloy with eutectic composition. Alloy 2 is an example of a hypoeutectic composition, while Alloy 3 has a composition outside the eutectic reaction range.

***Alloy 1*:** Alloys of eutectic composition ($x_E$) remain in a liquid state until the eutectic temperature ($T_E$) is reached. At this point, the liquid phase undergoes isothermal eutectic solidification. The resulting microstructure consists of fine aggregates of the solid phases that make up the eutectic [15]. The phases involved in the eutectic correspond to the endpoints of the eutectic isotherm. In the Al-Si system shown in *Figure 11*, the eutectic consists of pure silicon (β phase) and an Al-Si solid solution of composition $x_3$ (α phase). The proportion of each eutectic phase can be calculated as follows:

$$\alpha(eutectic) = \frac{100 - x_E}{100 - x_3} \times 100 = \frac{100 - 12.2}{100 - 1.7} \times 100 = 89.3\ \%$$

$$\beta(eutectic) = \frac{x_E - x_3}{100 - x_3} \times 100 = \frac{12.2 - 1.7}{100 - 1.7} \times 100 = 10.7\ \%$$

***Alloy 2*:** Alloys can be classified as hypoeutectic or hypereutectic. While these alloys do not have a eutectic composition, their solidification process still results in the formation of the eutectic phase. Upon reaching the liquidus temperature ($T_5$), a solid aluminum phase begins to precipitate from the liquid solution. This primary solid phase is referred to as the pre-eutectic or primary constituent [13]. When the eutectic isotherm is reached (at $T_E$), the remaining liquid phase solidifies according to the eutectic reaction. The proportion of each phase can be determined as follows:

$$\alpha(primary) = \frac{x_E - x_2}{x_E - x_3} \times 100 = \frac{12.2 - 5}{12.2 - 1.7} \times 100 \approx 68.6\ \%$$

$$\alpha + \beta(eutectic) = \frac{x_2 - x_3}{x_E - x_3} \times 100 = \frac{5 - 1.7}{12.2 - 1.7} \times 100 \approx 31.4\ \%$$

At a temperature of $T_6$ (below $T_E$), the alloy is fully solidified. Cooling from the eutectic temperature results in a minor change in composition due to diffusion. It is important to note that solid-state diffusion is only accounted for under equilibrium conditions.

***Alloy 3*:** For temperatures above $T_1$, alloy 1 exists as a liquid solution. Upon reaching the liquidus temperature ($T_1$), the solid phase begins to precipitate until the temperature reaches the solidus ($T_2$), at which point the liquid phase is fully solidified. The solidification path of this alloy lies outside the eutectic isotherm ($x_2 < x_3$). Under equilibrium conditions, this path does not lead to the formation of the eutectic phase. As a result, the solidification process produces a monophasic, undersaturated solid solution of silicon in aluminum. The monophasic solid solution remains unchanged until temperature $T_3$ is reached. At this point, the solvus curve indicates the solubility limit, meaning further cooling causes a decrease in the solubility of silicon in aluminum. This reduction in solubility leads to the precipitation of a silicon phase within the primary aluminum phase. The compositions and proportions of the phases can be calculated in the same manner as for an isomorphous alloy.

## 1.2 CONVENTIONAL SOLIDIFICATION MODELS

### 1.2.1 EQUILIBRIUM SOLIDIFICATION

During equilibrium solidification, a phase change occurs at each progressively lower temperature. As discussed previously, these phase changes and composition shifts can be tracked using the phase diagram of the system. A key characteristic of equilibrium solidification is the assumption of infinite and instantaneous diffusion (or complete diffusion) within both the liquid and solid phases. This assumption implies that the solid phase has sufficient time to reach its equilibrium composition before further solidification occurs. As a result, the lever rule can be applied to calculate the proportion of each phase at any given temperature. The conservation rule that governs equilibrium conditions is expressed as follows:

$$\%S = V_S = \frac{C_L - C_0}{C_L - C_S} = \frac{d_L}{C_L - C_s} \rightarrow C_L - C_S = \frac{d_L}{V_S}$$

$$\%L = V_L = \frac{C_0 - C_S}{C_L - C_S} = \frac{d_S}{C_L - C_s} \rightarrow C_L - C_S = \frac{d_S}{V_L}$$

$$=> \frac{d_L}{V_S} = \frac{d_S}{V_L} \rightarrow d_L * V_L = d_S * V_S$$

*Figure 12* illustrates the relationship between instantaneous diffusion in the solid phase and the lever rule. It is important to note that the composition of the solid phase is represented by the horizontal lines, which reflect the assumption of instantaneous diffusion. This indicates that only a single solid phase composition is considered at each temperature. Additionally, it is noteworthy that the solid phase composition never exceeds the nominal value ($C_0$) and is only reached at the final stage of solidification ($V_{S4}$).

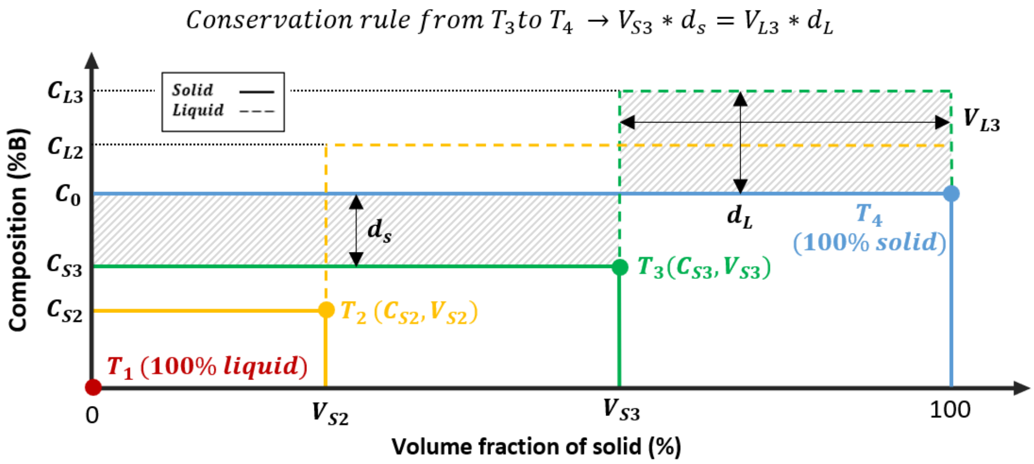

$$Conservation\ rule\ from\ T_3 to\ T_4\ \rightarrow V_{S3} * d_s = V_{L3} * d_L$$

**Figure 12:** Conservation rule under equilibrium solidification conditions

As an example, let $C_0$ (*Figure 13*) represent the nominal composition of an alloy composed of elements A and B. At $T_0$, the alloy is completely molten, and no phase change occurs until the liquid reaches temperature $T_1$, at which point solidification begins with the formation of crystals of composition $C_{S1}$ (point $x_{S1}$). The first solid phase generally contains the lowest amount of solute element (component B), which results in an increase in solute element in the liquid phase. As cooling progresses, the solidification of a phase with a higher content of component B occurs. Throughout this process, diffusion and crystal growth continue until the alloy is completely solidified ($x_4$), at which point the liquid phase disappears. The resulting solid has a microstructure of grains with a homogeneous nominal composition (point $x_4$, where $C_{S4} = C_0$). It is important to note that under equilibrium conditions, the final solid microstructure's composition never exceeds the nominal value of component B.

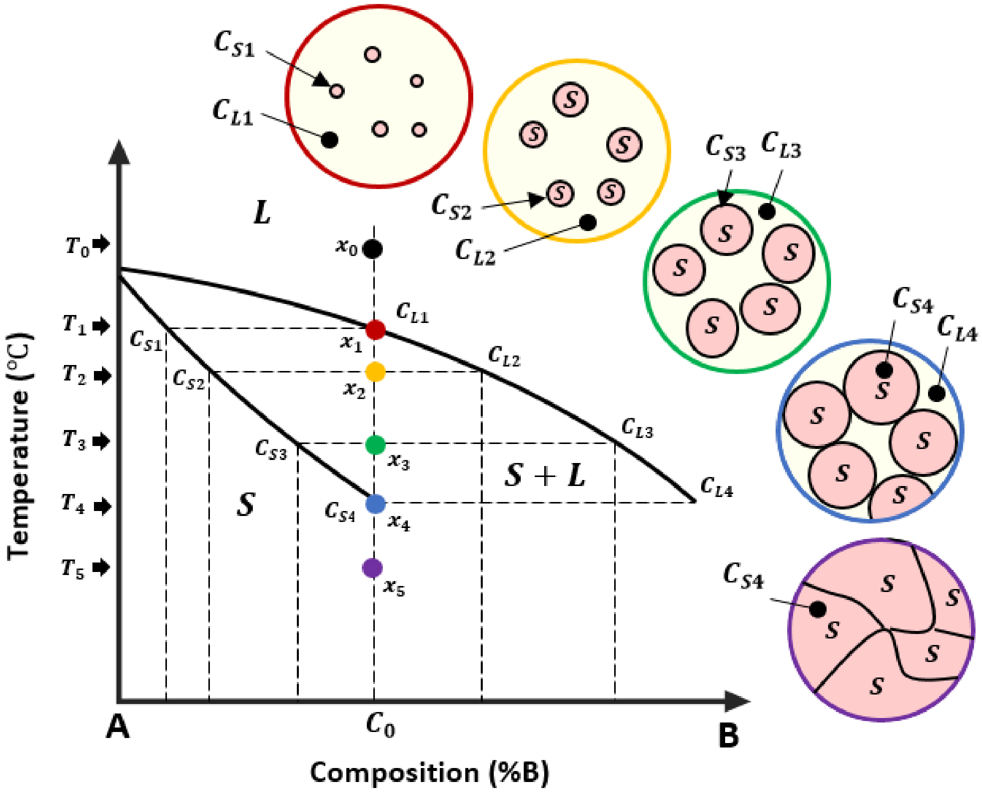

**Figure 13:** Phase diagram for a solidification under equilibrium condition

**Equilibrium eutectic solidification:**

In these systems, the unique microstructure formed during the eutectic reaction plays a crucial role in determining the mechanical properties of the alloy. Under equilibrium conditions, changes in composition primarily affect the final phase proportions. *Figure 14* illustrates a typical eutectic phase diagram, along with the most relevant solidification paths.

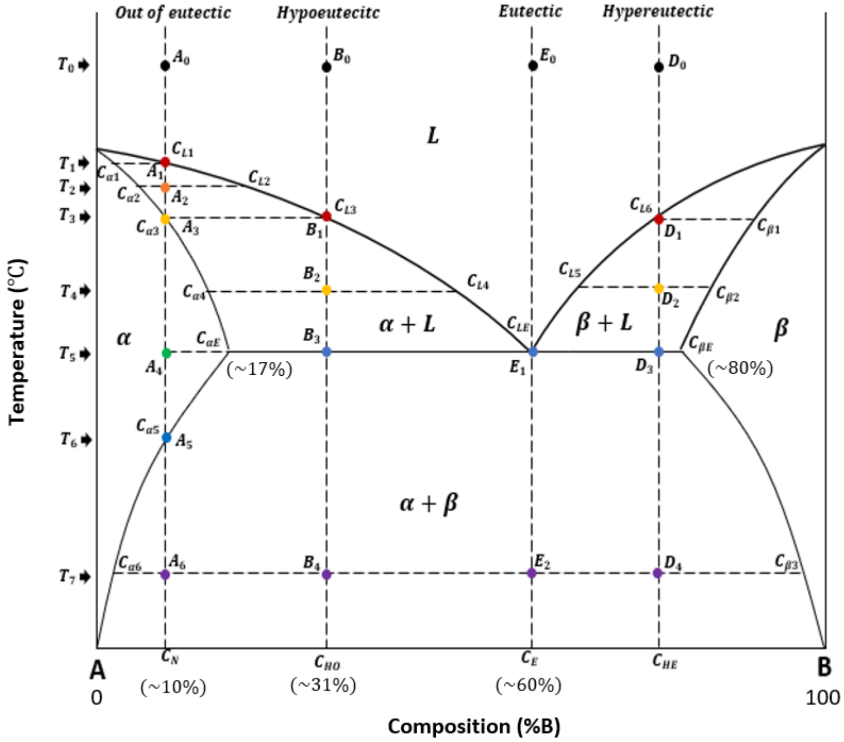

**Figure 14:** Typical solidification paths of a eutectic system. (schematic representation, hypothetical alloy)

**Eutectic composition:**

In the case of alloys with eutectic composition ($C_E$), solidification begins only when the eutectic temperature (*Figure 14 point* $E_1$) is reached. At this point, the two eutectic phases are assumed to begin solidifying simultaneously, forming the eutectic structure (*Figure 15A*). Since the eutectic reaction is isothermal, the compositions of the phases ($C_{\alpha E}$ and $C_{\beta E}$, *Figure 14*) remain constant throughout the solidification process. As a result, the lever rule can be applied to determine the relative proportions of the phases within the whole of the eutectic constituent.

$$\%\alpha = \frac{C_{\beta E} - C_{LE}}{C_{\beta E} - C_{\alpha E}} \times 100 \approx 32\% \ ; \ \%\beta = \frac{C_{LE} - C_{\alpha E}}{C_{\beta E} - C_{\alpha E}} \times 100 \approx 68\%$$

Under equilibrium conditions, the final microstructure consists entirely of grains with eutectic composition. *Figure 15B* illustrates a typical Al-Si eutectic phase. It is important to note that the length, spacing, and orientation of the lamellar structure can vary significantly as a function of the nominal composition (*Figure 8*) and solidification conditions (process driven). In alloys, specific elements such as strontium (Sr) can be used to modify the eutectic morphology [16]. Consequently, the microstructure of eutectic alloys can differ widely depending on the relative proportions of the two solid phases and the interaction between the alloying elements.

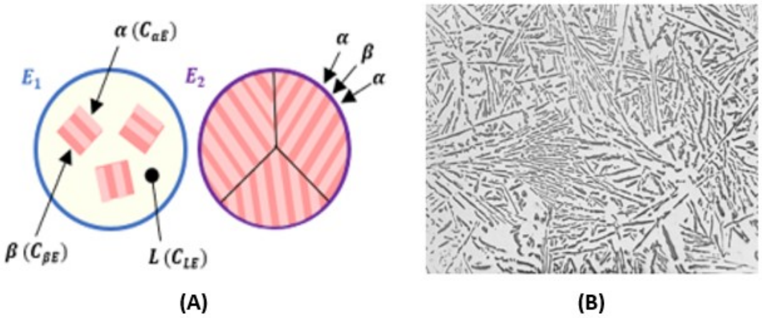

**Figure 15:** (A) Theoretical representation of the eutectic solidification; (B) Typical eutectic structure observed in Al-Si alloys [17]

**Hypoeutectic and hypereutectic compositions:**

In addition to alloys with eutectic composition, the solidification paths leading to eutectic solidification also include hypoeutectic ($C_{\alpha E} < C_x < C_E$) and hypereutectic ($C_E < C_x < C_{\beta E}$) alloys. During solidification, these alloys first form a primary phase before the eutectic, resulting in a microstructure with two main phases. The key difference between hypoeutectic and hypereutectic alloys lies in the primary constituent, which consists of distinct phases, α and β, respectively (*Figure 14*). However, regardless of the solidification path, the phases composing the eutectic constituent always correspond to the system's eutectic compositions ($C_{\alpha E}$ and $C_{\beta E}$). The following figure illustrates the microstructure of hypoeutectic (*Figure 16A*) and hypereutectic (*Figure 16B*) Al-Si based alloys, where the eutectic phase can be observed solidifying around the primary constituent grains in both cases.

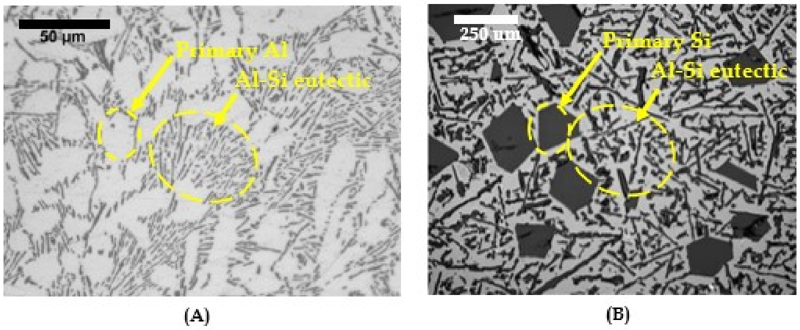

**Figure 16:** Typical microstructure of Al-12.6%Si hypoeutectic [18] (A) and Al-17% hypereutectic [19] (B) alloys

To fully understand the equilibrium solidification process of these alloys, let's consider the hypoeutectic composition ($C_{HO}$) shown in *Figure 14*. Upon reaching the liquidus, the primary constituent begins to solidify with a composition of $C_{\alpha 3}$. As cooling continues, the whole primary constituent ($\alpha'$) grows and its content in the B component progressively increases, with its composition shifting from $C_{\alpha 3}$ to $C_{\alpha 4}$. This process persists until the alloy reaches the eutectic temperature ($T_5$). At this stage (point $B_3$), the primary constituent ($\alpha'$ phase) and the remaining liquid phase both have the eutectic compositions, $C_{\alpha E}$ and $C_{LE}$, respectively. The relative proportions of each phase can be estimated as follows:

$$\%\alpha'\ (primary) = \frac{C_{LE} - C_{HO}}{C_{LE} - C_{\alpha E}} \times 100 \approx 67.4\ \%$$

$$\%L\ (eutectic) = \frac{C_{HO} - C_{\alpha E}}{C_{LE} - C_{\alpha E}} \times 100 \approx 32.6\ \%$$

Since the eutectic reaction is isothermal, no further cooling occurs until the remaining liquid solidifies into the eutectic phase around crystal and within the liquid. The relative proportions of the phases forming the eutectic constituents can be determined using the lever

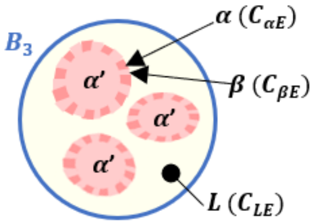

$$\%\alpha\ (eutectic) = \frac{C_{\beta E} - C_{LE}}{C_{\beta E} - C_{\alpha E}} \times 100 \approx 31.7\ \%$$

$$\%\beta(eutectic) = \frac{C_{LE} - C_{\alpha E}}{C_{\beta E} - C_{\alpha E}} \times 100 \approx 68.3\ \%$$

Considering some α phase solidified as the primary constituent during the initial stage of solidification, at temperatures above the eutectic, the final proportion of phases in the fully solidified alloy can be calculated as follows:

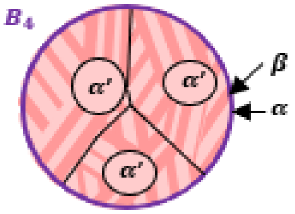

$$\%\alpha\ (total) = \frac{C_{\beta E} - C_{HO}}{C_{\beta E} - C_{\alpha E}} \times 100 \approx 77.8\ \%$$

$$\%\beta\ (total) = \frac{C_{HO} - C_{\alpha E}}{C_{\beta E} - C_{\alpha E}} \times 100 \approx 22.2\ \%$$

Finally, during equilibrium solidification, further diffusion of the elements occurs at lower temperatures. As a result, the composition of the eutectic constituents continues to evolve until the final temperature ($T_7$, point $B_4$) is reached. At this point, the α and β phases forming the eutectic have compositions of $C_{\alpha 6}$ and $C_{\beta 3}$, respectively. The lever rule can again be applied to determine the final relative proportions of the phases in both the eutectic and the entire solid.

$$\%\alpha\ (eutectic) = \frac{C_{\beta 3} - C_E}{C_{\beta 3} - C_{\alpha 6}} \times 100 \approx 39\ \%\ ;\ \%\alpha\ (total) = \frac{C_{\beta 3} - C_{HO}}{C_{\beta 3} - C_{\alpha 6}} \times 100 \approx 69\ \%$$

$$\%\beta (eutectic) = \frac{C_E - C_{\alpha 6}}{C_{\beta 3} - C_{\alpha 6}} \times 100 \approx 61\ \%\ ;\ \ \%\beta\ (total) = \frac{C_{HO} - C_{\alpha 6}}{C_{\beta 3} - C_{\alpha 6}} \times 100 \approx 31\ \%$$

**Composition out of the eutectic isotherm:**

In the case of alloys with compositions outside the eutectic isotherm ($C_x$ < $C_{\alpha E}$ and $C_x$ > $C_{\beta E}$), the resulting microstructure does not contain any eutectic constituents. For example, consider the alloys with composition $C_N$, as shown in *Figure 14*. Solidification begins at $T_1$, where the first crystals of the α phase form with a composition of $C_{\alpha 1}$. As cooling continues, the α phase becomes increasingly enriched in the B component until the solidus is reached at $T_3$. At this point ($A_3$), the alloy is fully solid. Between $T_3$ and $T_6$, the alloy exists as an undersaturated solid solution in the B component. At temperature $T_6$, the alloy composition reaches the solvus, and any further cooling results in the precipitation of the β phase (*Figure 17*). This characteristic is well understood and is often utilized to optimize the mechanical properties alloys through heat treatments.

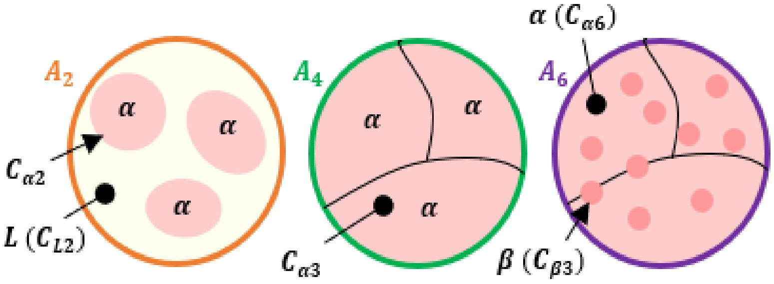

**Figure 17:** Theoretical representation of the solidification for alloys of composition outside the eutectic isotherm

As with any other solidification process under equilibrium conditions, the final relative proportions of the phases can be calculated using the lever rule:

$$\%\alpha\ (total) = \frac{C_{\beta 3} - C_N}{C_{\beta 3} - C_{\alpha 6}} \times 100 \approx 92\ \%$$

$$\%\beta\ (total) = \frac{C_N - C_{\alpha 6}}{C_{\beta 3} - C_{\alpha 6}} \times 100 \approx 8\ \%$$

### 1.2.2 DEPARTURE FROM EQUILIBRIUM

Equilibrium solidification conditions are primarily theoretical approximations, as true equilibrium is rarely achievable in practice due to the extremely long time required to readjust the composition of the phases and achieve complete diffusion. Since diffusion is mainly driven by atomic movement, which is much slower in the solid phase, it is often unrealistic to expect perfect diffusion in the solid. Therefore, some departure (or deviation) from equilibrium is inevitable under realistic cooling rates. To better understand this, let's consider the alloy of composition $C_0$ shown in *Figure 18*, where complete diffusion is maintained in the liquid but negligeable diffusion in the solid. Solidification begins with the deposition of crystals having composition $C_{S1}$ when temperature $T_1$ is reached. At $T_2$, the liquid composition shifts to $C_{L2}$, while the new solid that forms have a composition of $C_{s2}$. However, the solid that initially formed has not fully adjusted to this new composition. As a result, the average solid composition, $C'_{s2}$, is lower than the expected equilibrium composition, $C_{s2}$. As the temperature continues to decrease to $T_3$, additional solid forms with a composition of $C_{s3}$, causing the average solid composition, $C'_{s3}$, to diverge further from the equilibrium composition.

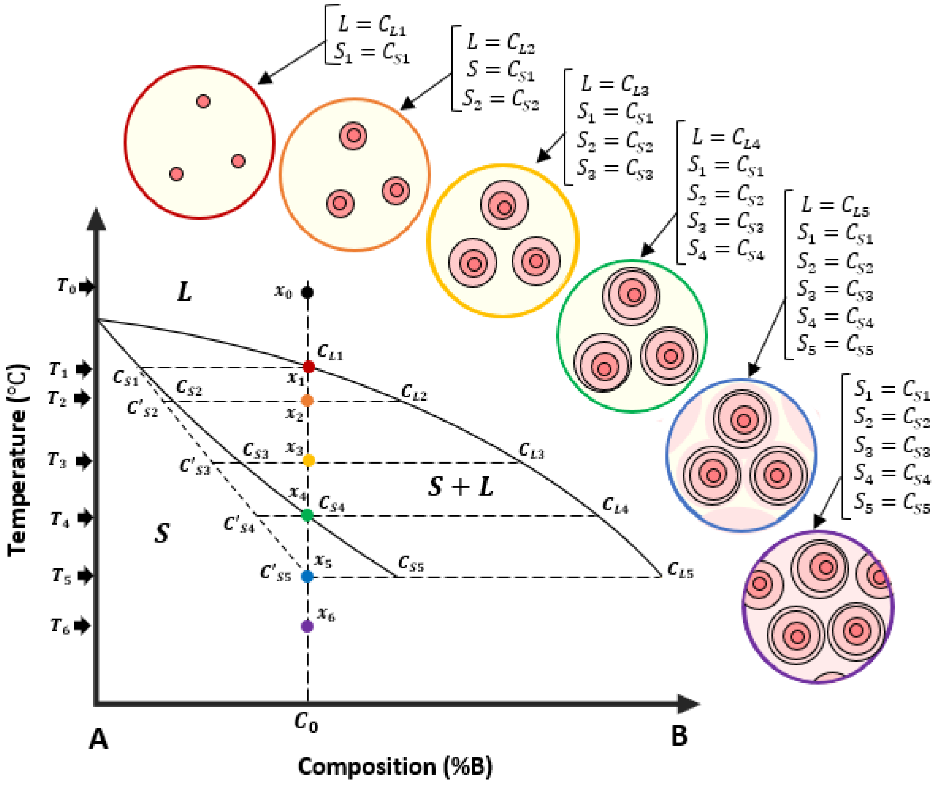

**Figure 18:** Non-equilibrium solidification with partial diffusion in the solid phase. Dashed line ($C_{S1} \rightarrow C'_{S5}$) represents the average solid composition

Under equilibrium solidification, the alloy would be fully solidified upon reaching temperature $T_4$. However, as shown in the composition–volume fraction of solid relationship in *Figure 19*, this is not the case ($V_{s4} < 1$). Although the solid formed at $T_4$ has the nominal composition, the average solid composition ($C'_{s4}$) is still lower than the nominal composition ($C_0$). As a result, mass balance can only be maintained if some liquid remains. This results in an extended temperature range over which both liquid and solid phases coexist. As cooling continues from $T_4$, the solid formed becomes richer in component B than the nominal composition ($C_{s5} > C_0$). Eventually, at $T_5$, the average solid composition ($C'_{s5}$) matches the nominal composition, and the alloy is fully solidified.

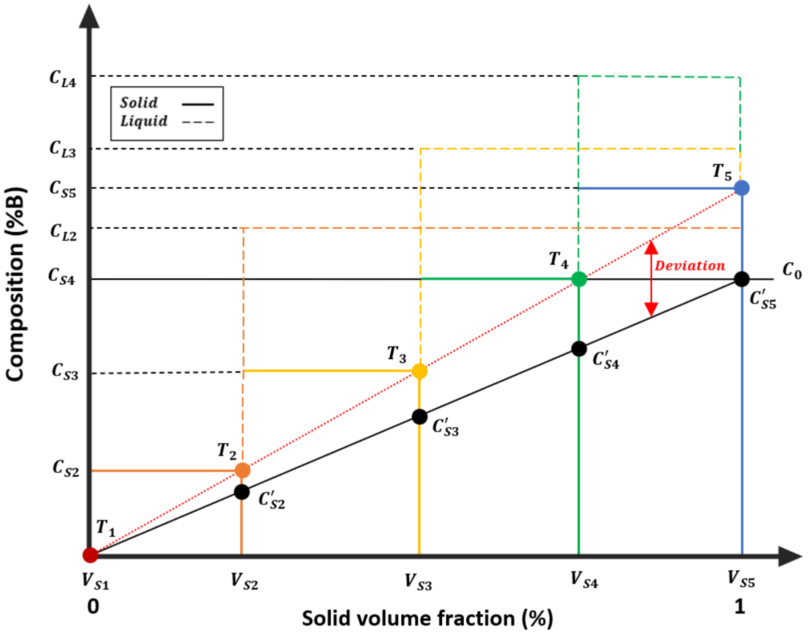

**Figure 19:** Relation between composition and solid volume fraction under non-equilibrium conditions

From a microstructural perspective, the change in composition of the solid phase during solidification is known as coring [10]. Each successive layer of solid is progressively richer in solute element than the previous one, creating a composition gradient in the fully developed crystals. A theoretical representation of this cored microstructure is presented in *Figure 18*, along with the corresponding phase diagram.

**Hypoeutectic and hypereutectic compositions:**

Assuming, complete diffusion in the liquid and no diffusion in the solid, the solidification of alloys with eutectic composition remains unchanged ($C_{Eutectic}$, *Figure 20*). However, the solidification of hypoeutectic and hypereutectic alloys results in coring of the primary constituent. This coring effect causes the average composition to deviate from equilibrium, progressing as shown in *Figure 20* ($\alpha_1 \rightarrow \alpha_4'$). As shown in the diagram, for an alloy of nominal composition $C_{nom}$ the shift in solid composition from $\alpha_4$ to $\alpha_4'$ results in a greater proportion of liquid as the temperature approaches the eutectic isotherm. As a result, the proportion of the eutectic constituent at the end of solidification is expected to be higher under non-equilibrium conditions compared to equilibrium conditions. In rapid solidification processes, past studies have established that solute trapping mitigate the increase in eutectic fraction resulting from the coring effect [20, 21]. Finally, since the eutectic reaction is isothermal, the composition of the eutectic constituents remains the same as under equilibrium conditions.

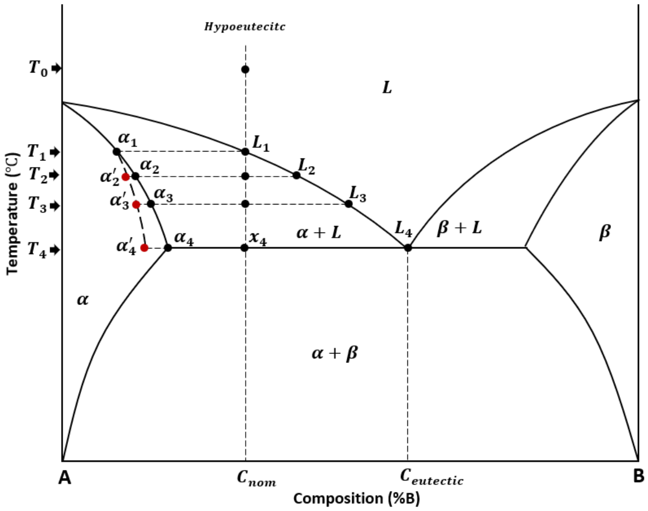

**Figure 20:** Eutectic solidification under non-equilibrium conditions

**Composition out of the eutectic isotherm:**

For alloys with compositions outside the eutectic reaction isotherm, solidification typically does not result in the formation of the eutectic constituent. However, assuming complete diffusion in the liquid and negligeable diffusion in the solid, these alloys may form a small proportion of the eutectic constituent. Due to the departure from equilibrium, some liquid phase may remain when the eutectic temperature is reached. As a result, this remaining liquid undergoes eutectic solidification. For example, the alloy with composition $C_{nom}$, shown in *Figure 21*, would normally be fully solidified by the time temperature $T_3$ is reached. Under non-equilibrium conditions, however, the phase diagram indicates that some liquid phase persists until the eutectic temperature ($T_4$) is reached. At this point, the remaining liquid has reached the eutectic composition, leading to the solidification of the eutectic phase—an event that would not occur under equilibrium conditions.

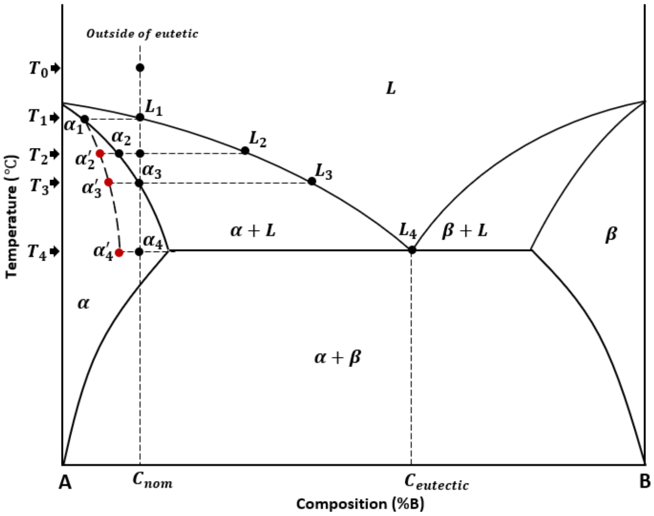

**Figure 21:** Departure from equilibrium for alloy of composition lying outside the eutectic isotherm

### 1.2.3 THE SCHEIL SOLIDIFICATION MODEL

As previously mentioned, equilibrium solidification is not achievable in practice due to the limited diffusion rate in the solid phase. Moreover, calculating the exact diffusion rate in the solid phase at a given temperature is impractical. An approximation of the non-equilibrium solidification process can be obtained using the classical Scheil model [10]. The classical Scheil model is based on several key assumptions:

1) Local equilibrium at the solidification interface.
2) No mass flow into or out of the volume element.
3) Instantaneous diffusion in the liquid phase.
4) Negligible diffusion in the solid phase.

This model predicts the solute concentration as a function of the solid fraction using the following equation:

$$C_S' = KC_0(1 - f_s)^{(K-1)}$$

In this equation, $C_S'$ represents the composition of the solidifying phase at a given weight fraction $f_s$, $C_0$ denotes the initial average composition, and K is the equilibrium partition coefficient obtained from the phase diagram ($K$ = $C_S$ / $C_L$). Based on the assumptions regarding diffusion, even the slightest change in temperature leads to a change in the composition of the solidifying phase, which causes the coring of the solid phase (see *Figure 18*). It is worth noting that the lever rule method is not applicable when using the Scheil solidification model.

Let's now analyze the example presented in *Figure 22*. At point A, the solidifying phase has reached the nominal composition, $C_0$. However, as previously mentioned, under non-equilibrium conditions, a portion of the liquid ($d_{VS} + V_L$) remains unsolidified due to the negligible diffusion in the solid phase (or departure from equilibrium). As solidification progresses, the solidifying phase reaches a composition of $C_S'$ (point B), leading to an increase in the solid fraction from $V_s$ to $V'_s$ and a corresponding decrease in the liquid fraction to $V_L$. Just as under equilibrium conditions, mass balance must be maintained for the Scheil solidification model to be valid. Therefore, the changes in composition and volume fraction of both phases must be proportional. Based on this, the following equation can be defined:

$$(C_L - C'_s) * d_{VS} = V_L * d_{CL}, \text{ where } V_L = 1 - V_s$$

Both sides of this equation correspond to the dashed areas in *Figure 22*. From point B onward, the solidification process will continue until the remaining liquid phase has either fully solidified or reached the eutectic composition ($C_{LE}$), at which point it will solidify into the eutectic constituent.

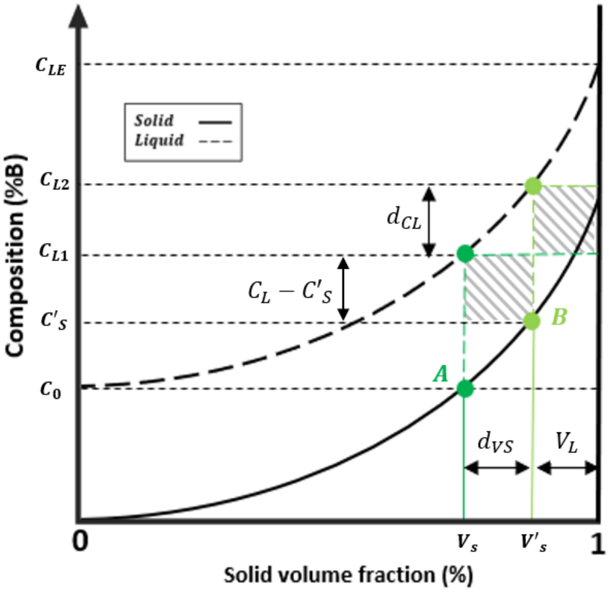

**Figure 22:** Theoretical mass balance for the Scheil solidification model

## 1.3 RAPID SOLIDIFICATION

### 1.3.1 INTRODUCTION TO RAPID SOLIDIFICATION PROCESSING

Rapid solidification processing (RSP) of aluminum alloys has been extensively studied, especially for selective laser melting (SLM) applications, characterized by solute trapping and modifications in growth front morphology. These changes are attributed to the high solidification front velocities (SFVs) of the primary phase. Solute trapping occurs when solute atoms are engulfed by the rapidly advancing solidification front when diffusion in the liquid can no longer be assumed to be complete, limiting segregation [20, 21]. Additionally, high SFVs increase surface tension, stabilizing the interface and altering the growth front morphology.

When applied to HPVDC and especially thin-walled components, the classic Scheil model presented previously predicts a lower eutectic fraction than the equilibrium calculation, but still a higher Al-Si eutectic fraction than the measured value. This discrepancy arises because the model's assumption of local equilibrium at the solidification interface may not hold true at the high cooling rates typical of rapid solidification. At high solidification front velocities, local equilibrium at the growth front is disrupted, leading to solute enrichment in both the solid and liquid phases. From a phase diagram perspective, the liquidus and solidus lines, eutectic composition, and corresponding temperatures deviate from their equilibrium values, making thermodynamic properties dependent on the solidification front velocity.

### 1.3.2 RAPID SOLIDIFICATION MODELS

To address these deviations, specific approaches were adopted to account for the velocity dependence of various phase diagram parameters, such as the solubility of Si and the partition coefficient ($K$). According to Aziz et al. [22], the velocity-dependent partition coefficient ($K_V$) for dilute solutions can be represented as follows:

$$K_V = \frac{\mathrm{K} + \frac{\mathrm{a_0 V}}{\mathrm{D}}}{1 + \frac{\mathrm{a_0 V}}{\mathrm{D}}} \tag{1}$$

In this equation, K represents the partition coefficient at equilibrium (when $V \to 0$). D denotes the diffusion coefficient of the solute element in the growth direction, while $a_0$ is the characteristic distance that solute atoms move (the interface diffusion length), which is approximately equal to the thickness of the solid-liquid interface. For the Al-Si alloy system, $a_0$ is considered to be 1 nm [23]. This model is strictly applicable to dilute solutions. However, Pierantoni et al. [23] found experimentally that for concentrated Al-Si solutions with Si content between 15.5 wt% and 26 wt%, the discrepancies between this model and the observed values are negligible.

It is well known that variations in solidification front velocity, cooling rate, and the Gibbs-Thomson parameter can lead to different microstructural morphologies (*Figure 23*)[24]. In this context, two distinct approaches have been identified for adapting the phase diagram to rapid solidification processing, in addition to the SFV-dependent partition coefficient. The first approach is based on planar growth (Approach 1), while the second is based on dendritic growth (Approach 2).

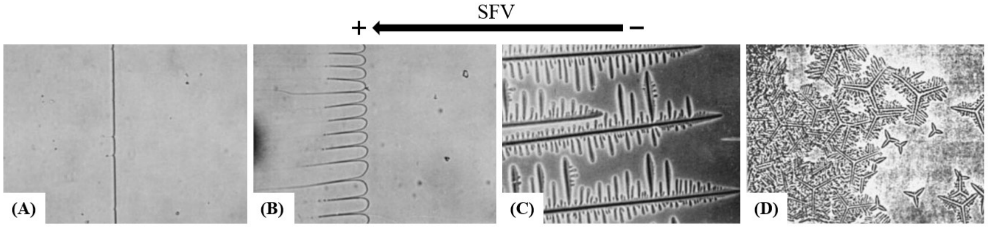

**Figure 23:** Typical microstructure resulting from (A) planar growth, (B) cellular growth, (C) columnar dendritic growth and (C) dendritic growth [25]

**Approach 1:**

Pierantoni et al. [23] developed an empirical method to predict the eutectic growth temperature and composition as functions of the growth rate in the planar growth regime, typical of additive manufacturing processes like SLM. In this approach, the liquidus and solidus lines converge at the $T_0$ line (*Figure 24*). It is assumed that the narrowing between the liquidus and solidus lines is symmetrical around $T_0$, based on the following relation

$$\frac{C_L(V) - C_{T_0}}{C_L(0) - C_{T_0}} = \frac{C_S(V) - C_{T_0}}{C_S(0) - C_{T_0}} \tag{2}$$

In this equation, $C_{T0}$ represents the concentration at the $T_0$ line, corresponding to the interface temperature, while $C_L(0)$ and $C_S(0)$ denote the equilibrium concentrations of the liquidus and solidus, respectively. $C_L(V)$ and $C_S(V)$ refer to the corresponding kinetic concentrations. Once the equilibrium phase diagram is established using $C_L(0)$, $C_S(0)$, and $C_{T0}$, the specific values of $C_L(V)$ and $C_S(V)$ can be determined using *Equation (1)* and *Equation (2)*, since the partition coefficient $K$ is defined as $C_S/C_L$. Consequently, the eutectic fraction $(f_E)$ can be calculated using the following relationship, based on the Lever rule:

$$\mathrm{f_E} = \frac{\mathrm{C_0} - \mathrm{C_S^{max}(V)}}{\mathrm{C}_L(V) - \mathrm{C_S^{max}(V)}} \tag{3}$$

Where $C_S^{max}(V)$ is the maximum solubility of Si in the solid phase, and $C_0$ is the initial composition of the Al-Si alloy being investigated.

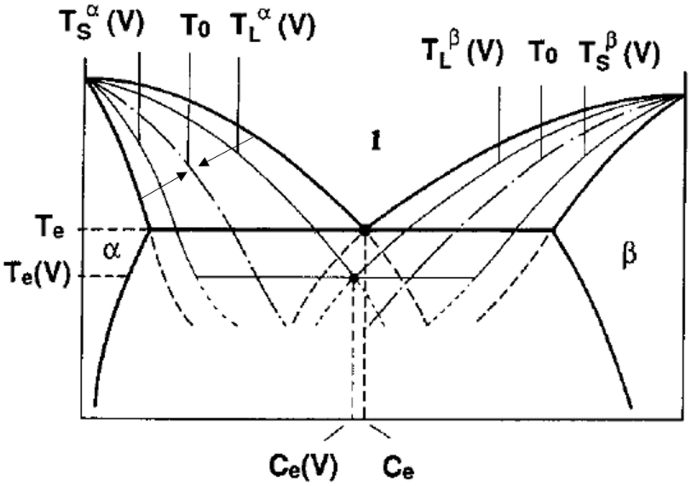

**Figure 24:** Convergence of the solidus and liquidus lines [23]

As depicted in *Figure 24* when considering higher SFVs the eutectic point, the solidus and liquidus shift, affecting the phase proportion for a given nominal composition. Furthermore, the shift of the solidus to the right clearly depicted how solute trapping over coring, resulting in lesser eutectic, even under non-equilibrium conditions.

**Approach 2:**

Kurz, Giovanola and Trivedi developed a model, referred to as the KGT model, to describe microstructural development during processes involving high SFVs [26]. Based on this model, Trivedi et al. [27] applied a physical model for dendritic growth under rapid solidification conditions in the Al-Si alloy system, as follows:

$$\mathrm{m_V} = m\left(1 + \frac{K - K_\mathrm{V} + K_\mathrm{V}\ln\left(\frac{K_\mathrm{V}}{K}\right)}{1 - K}\right) \tag{4}$$

This model assumes that the liquidus and solidus lines in the Al-Si phase diagram are linear, with $m$ representing the liquidus slope in the equilibrium phase diagram and $K$ the equilibrium partition coefficient. *Equation (4)* indicates that, in an equilibrium diagram with constant $m$ and $K$, the parameter $m_V$ varies with the solidification front velocity $V$ through $K_V$. This adjustment ensures that as $K_V$ approaches unity, the slope of the liquidus line aligns with that of the $T_0$ line, where the Gibbs free energy is equal in both the solid and liquid phases. By knowing $K_V$ at each specific solidification front velocity through *Equation (1)* and using the equilibrium phase diagram parameters ($m$ and $K$), the modified liquidus slope $m_V$ can be calculated using *Equation (4)*. Once $m_V$ is determined, the corresponding kinetically modified solidus slope can be calculated as follows [27]:

$$solidus\ line\ slope = \frac{\mathrm{m_V}}{K_\mathrm{V}} \tag{5}$$

Consequently, the Al-Si eutectic fraction ($f_E$) can be approximated using the following relationship based on the lever rule:

$$\mathrm{f_E} = \frac{\mathrm{C_0} - \mathrm{C_S^{max}}(V)}{\mathrm{C}_L - \mathrm{C_S^{max}}(V)} \tag{6}$$

Where $C_S^{max}$ is the maximum solubility of Si in solid, $C_L$ is the solubility of Si in liquid at eutectic temperature and, $C_0$ is the initial composition of the investigated Al-Si alloy, respectively.

In the context of HPDC of magnesium alloys, Berman et al. [28] applied the Kraft model [29] utilizing the velocity dependent partition coefficient relationship, proposed by Aziz et al [21] and Carrard [30], along with numerical simulations and estimated solidification front velocities (SFVs) ranging from approximately 13 mm/s to 144 mm/s, depending on casting thickness and distance from the die surface. However, it is important to note that the reported modeling resolution limitations likely led to an underestimation of the peak velocity. Apart from Berman's work, a non-equilibrium thermodynamics module, known as "modified Scheil with solute trapping," was developed and incorporated into ThermoCalc software version 2022a, specifically for high solidification speed processes such as additive manufacturing. Del Guercio et al. [31] utilized this module in their study on additively manufactured AA2024 alloy. However, it should be noted that this module is tailored for additive manufacturing, where a constant solid-liquid interface thickness and SFVs in the range of 0.5-3.0 m/s are typical. SFVs in this range is only achievable in additive manufacturing processes, therefore the module it is not applicable to HPDC.

## 1.4 THE HPVDC PROCESS

This section provides a detailed overview of the HPDC process, aiming to clarify how process parameters affect material solidification. The goal is to pinpoint the stage at which solidification transitions toward conditions resembling rapid solidification. Additionally, the impact of process parameters on the formation of various microstructural characteristics in HPDC components is thoroughly examined.

### 1.4.1 MAIN STAGES OF THE HPDC PROCESS

As shown in *Figure 25*, the HPDC process consists of three main stages: filling the shot sleeve, injecting the material into the die cavity, and the pressure intensification stage [32].

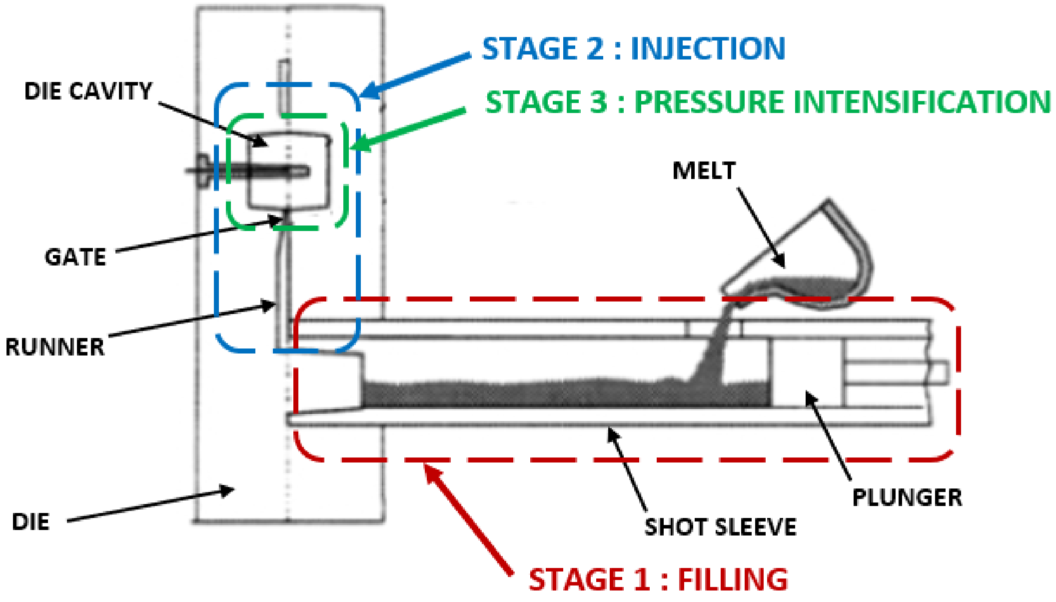

**Figure 25:** The main stages of the high pressure die casting process (cold chamber) [33]

The filling stage begins with transferring the melt from the furnace into the shot sleeve. In the next step, the plunger forces the melt at the injection end of the shot sleeve. Following this, the injection stage begins, where the plunger rapidly pushes the melt into the die cavity. Once the cavity is fully filled, the pressure intensification stage starts. This final stage in the high-pressure die casting process contributes to material feeding during solidification. The pressure intensification promotes complete solidification of the part before it is ejected from the die cavity.

### 1.4.2 OVERVIEW OF THE MICROSTRUCTURE CHARACTERISTICS

HPDC products exhibit a distinctive combination of microstructural characteristics, which are influenced by the process parameters. *Figure 26* illustrates the typical microstructure resulting from the HPDC process for Al-Si and Al-Mg alloys. While these alloy systems lead to different constituents and element distributions, the characteristic microstructural features of the HPDC process are evident in both. The main zones, starting from the centerline, include the core, followed by the segregation band, and the skin layer, which extends up to the die interface. These zones can be differentiated not only by their relative positions but also by their content of the primary aluminium and eutectic phases. Additionally, they vary in the proportion of porosities and externally solidified crystals (ESCs) present. The following sections provide a detailed examination of the relationships between these microstructural characteristics and the three stages of the process.

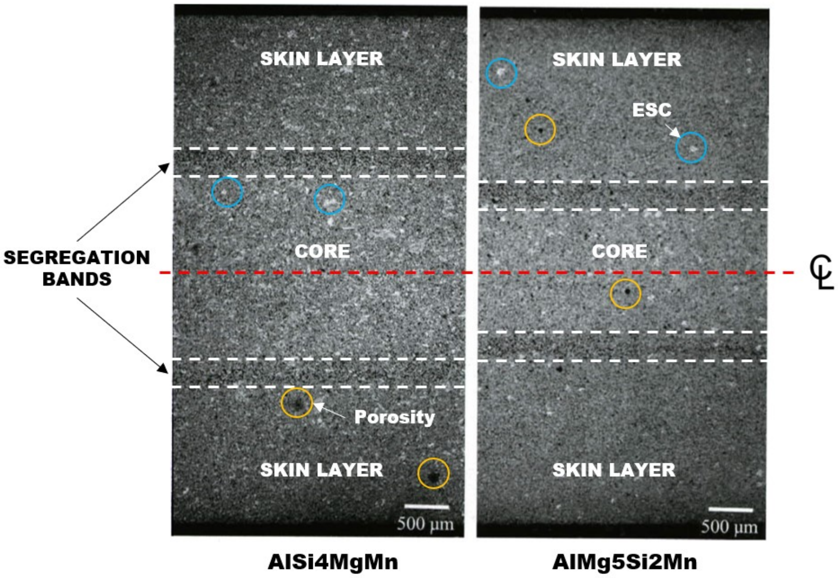

**Figure 26:** Typical microstructural characteristics observed in HPDC components [8]

*Table 2* provides an overview of the relationships between some of the key parameters in the three process stages and the microstructural features of HPDC products. It is clear that the microstructure obtained from the HPDC process results from complicated interaction at during the stages of the process.

**Table 2:** Examples of the influence of the process stages on microstructural characteristics from past studies [8, 34-62].

| Stage | | Parameters | Microstructural characteristics | | | |
|---|---|---|---|---|---|---|
| | | | Porosity | ESCs | Segregation Band | Skin layer |
| 1 | Filling of the shot sleeve | Pouring temp. | | X | | |
| | | Filling rate | X | X | | |
| | | Slow shot velocity | X | X | | |
| 2 | Injection in the die cavity | Melt temp. | X | | | |
| | | Plunger velocity | X | X | X | X |
| | | Runner and gate design | | X | | X |
| | | Mould temp. | | | | X |
| 3 | Pressure Intensification | Intensity | X | X | X | X |
| | | Mould temp. | | X | | X |

### 1.4.3 FILLING OF THE SHOT SLEEVE

In cold chamber die casting, the first step involves pouring molten metal into the shot sleeve. The plunger then accelerates to its slow shot speed (*Figure 27A*). Acceleration and velocity are determined to control the wave formed ahead of the plunger. Afterward, the plunger moves down the shot sleeve until most of the volume of the shot sleeve is filled with melt (*Figure 27B*). This portion of the forming process is referred to as the slow shot stage [34]. Practically, the slow shot stage concludes when the plunger reaches the fast shot set point, which is the travel distance where the plunger transitions into the injection phase.

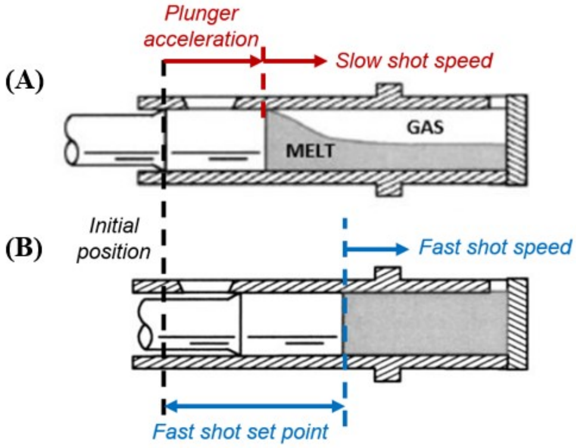

**Figure 27:** The different steps of the filling stage during HPDC. (A) End of the plunger's acceleration. (B) End of the slow shot stage [35]

The key parameters of interest during the filling stage include plunger velocity, filling ratio of the shot sleeve, and the temperatures of the components (plunger, melt, and shot sleeve). Additionally, retention time refers to the duration of the slow shot stage. The interplay of these parameters affects the final microstructure of the castings in two ways:

1. Turbulence in the melt flow in the shot sleeve can lead to the entrapment of gas. As a result, the microstructure of HPDC castings exhibits varying levels of gas porosity, depending on the extent of turbulence the melt experienced while filling the shot sleeve (*Figure 28A*).
2. Heat extraction occurring between the melt and the machine components results in the formation of crystals before injection. These crystals, known as externally solidified crystals (ESCs), are a notable characteristic of HPDC products (*Figure 28B*).

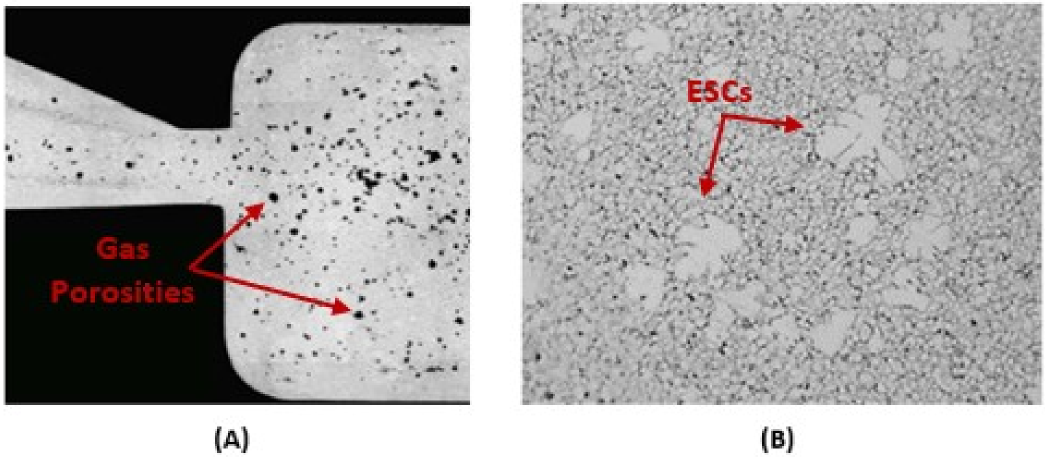

**Figure 28:** Microstructural characteristics resulting from the filling stage: (A) gas porosities [8], (B) externally solidified crystals (ESCs) [36]

**Influence of filling parameters on gas porosities:**

Gas porosities result from gas being entrapped in the melt due to turbulence in the shot sleeve. During the slow shot stage, turbulence occurs as the melt is poured and collides with the shot sleeve walls, before the plunger starts moving and possibly during acceleration as a wave forms ahead of the plunger. Korti [34] numerically demonstrated that the metal impacts both ends of the shot sleeve, creating a return flow that interacts with the incoming material. This wavelike motion, as shown in *Figure 29*, promotes the entrapment of gas.

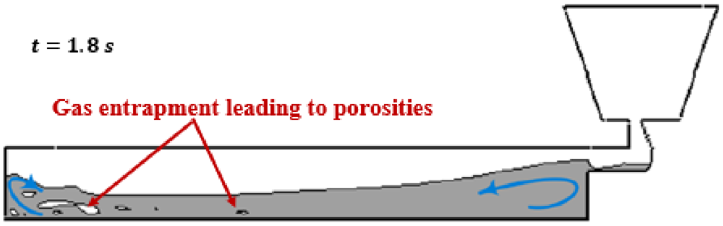

**Figure 29:** CFD ANSYS Fluent simulation of the pouring phase illustrates the moment when gas entrapment occurs due to the metal flow in the shot sleeve [34]

Additionally, their analysis of metal velocity demonstrated that a lower filling ratio in the shot sleeve leads to a more turbulent pouring phase. *Figure 30* shows the evolution of metal velocity during the pouring phase for filling ratios of 45% and 30%. The results indicate that at a 45% filling rate, the metal stabilizes quickly over time. In contrast, the velocity profile at a 30% filling ratio shows no signs of stabilization during the same period. As a result, the melt experiences more disturbance as the plunger pushes the metal down the shot sleeve, which promotes gas entrapment.

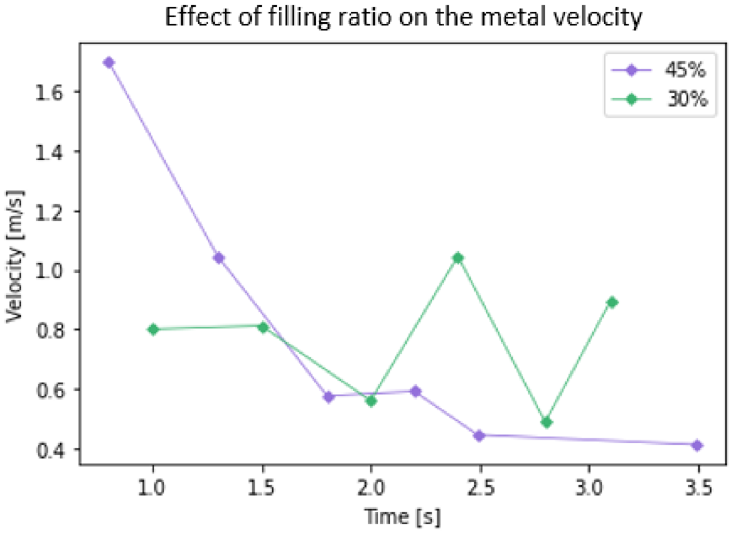

**Figure 30:** Effect of reduced filling ratio on average melt velocity during the pouring phase [34]

To mitigate this effect, they suggested that a settling time can contribute to ensure the melt becomes more stable before the plunger begins pushing. This delay also provides additional time for gas to escape from the melt's free surface. He concluded that a lower filling rate requires a longer settling time, which helps limit the impact of pouring turbulence on the stability of the filling phase, thereby reducing gas entrapment and porosity formation.

Once the metal is poured, the plunger drives it into the shot sleeve. Initially, the plunger generally accelerates before pushing the melt at a constant speed, known as the slow shot speed. During this phase, gas entrapment can occur if rollover of the melt's free surface occurs. This can happen in two ways: either through a wave break (*Figure 31A*) or the impingement of the melt on the shot sleeve ceiling (*Figure 31B*). Both gas entrapment mechanisms are influenced by the plunger acceleration and velocity during the filling phase.

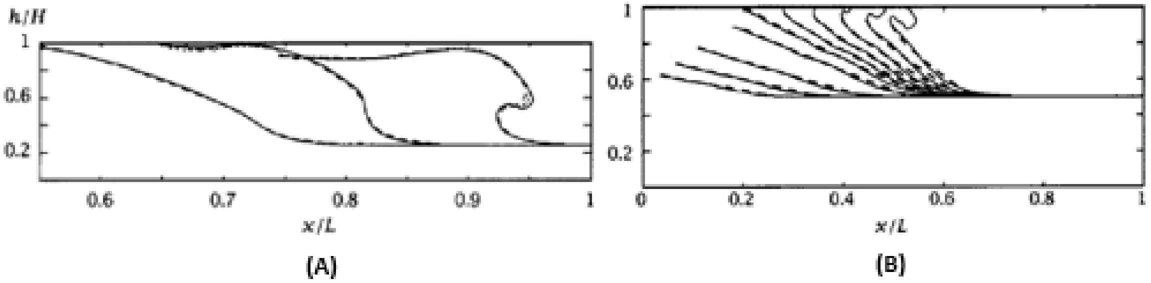

**Figure 31:** VOF finite element simulation of the shot sleeve filling reveals a wave break (A) and a surface rollover (B) caused by the impingement of the metal on the shot sleeve ceiling [35]

Most models to date suggest that gas entrapment during the slow shot stage is primarily due to the level of turbulence in the melt as the plunger begins to move [34, 37]. For example, the model developed by Kohlstädt demonstrates the variability in the amount of trapped gas during the slow shot stage, with plunger velocities ranging from 0.01 to 1 m/s [38]. This variation is believed to result from the position of the wave in the chamber when the plunger starts moving. Specifically, if the wave peak is near the plunger as it begins to move, most of the gas will be pushed ahead of the metal (*Figure 32A*). In contrast, if the wave peak is farther from the plunger, it will eventually collide with the moving plunger, creating turbulence in the melt (*Figure 32B*).

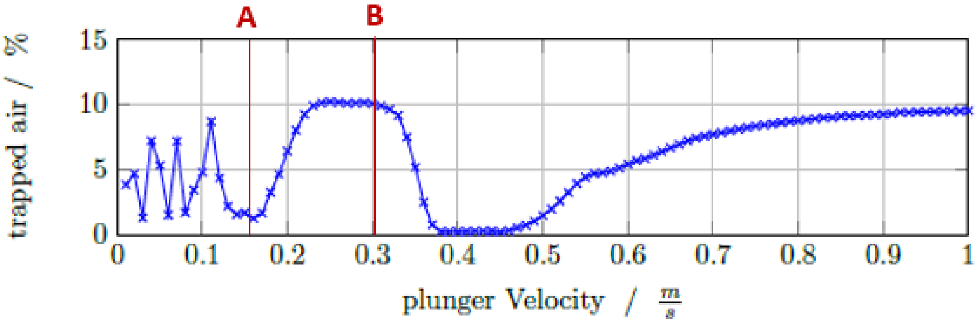

**Figure 32:** CFD model illustrating the influence of plunger velocity during the slow shot stage. The curve shows the percentage of trapped air in the shot sleeve as a function of plunger velocity [38]

The results presented in *Figure 33* from different experimental investigations show that both the porosity area fraction and the maximum velocity of the melt increase with plunger velocity [39-41]. Therefore, it can be concluded that an increase in plunger velocity during the slow shot stage promotes turbulence in the melt, leading to greater gas entrapment, but that the exact relationship between slow shot speed and porosity in the casting remains dependent on the specific machine and application.

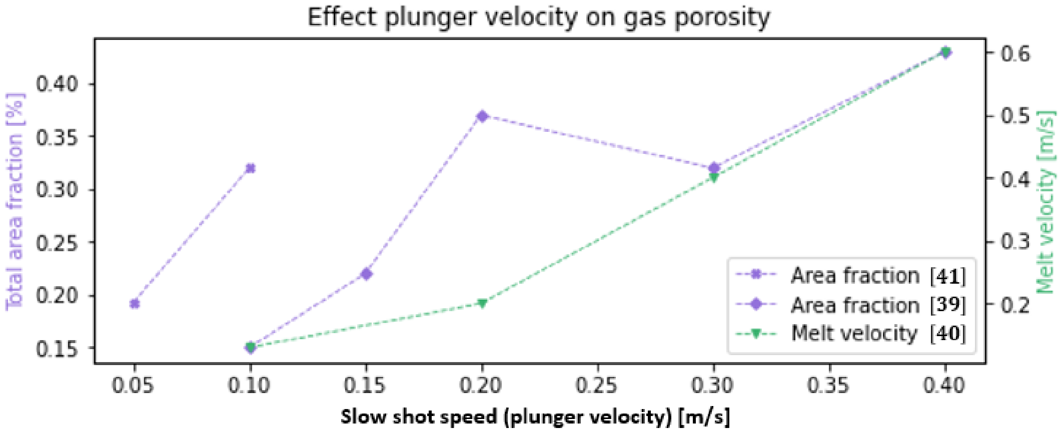

**Figure 33:** Effect of slow shot speed on turbulence intensity and gas porosity [39-41]

While the slow shot stage contributes to gas porosity, a statistical analysis conducted by Tsoukalas estimated the contribution of numerous process parameters on gas porosities (*Table 3*) and suggested that the slow shot stage only explain 1.88% of the variance of gas porosities in the final product in this case [42]. Therefore, the slow shot stage is not critical on the level of gas porosities present in HPDC products.

**Table 3:** Contribution of process parameters to gas porosity in HPDC products [42]

| Stage | Parameter | % |
|---|---|---|
| 1 | Slow shot velocity | 1.88 |
| 2 | Fast shot set point | 9.50 |
|  | Fast shot velocity | 22.01 |
|  | Die cavity filling time | 21.90 |
| 3 | Pressure intensification | 41.83 |

**Influence of filling parameters on ESCs:**

Externally solidified crystals (ESCs) are a crucial microstructural characteristic of HPDC products, as they form early in the process and influence subsequent stages of solidification. Research has demonstrated that ESCs nucleate and grow in thermally undercooled regions of the melt during the slow shot stage. Moreover, ESCs are most likely to crystallize near the plunger's face, the shot sleeve wall, and the free surface of the melt (*Figure 34*) [7, 8, 43].

Since ESCs are a product of solidification, their quantity and size in HPDC castings are influenced by the superheat loss during the slow shot stage. This superheat loss is governed by two main parameters: the initial temperature of the melt (pouring temperature) and retention time, which is directly related to the slow shot speed [44, 45]. Other factors contributing the ESC solidification include the tooling temperature as well as the surface finish and lubrication in the shot sleeve.

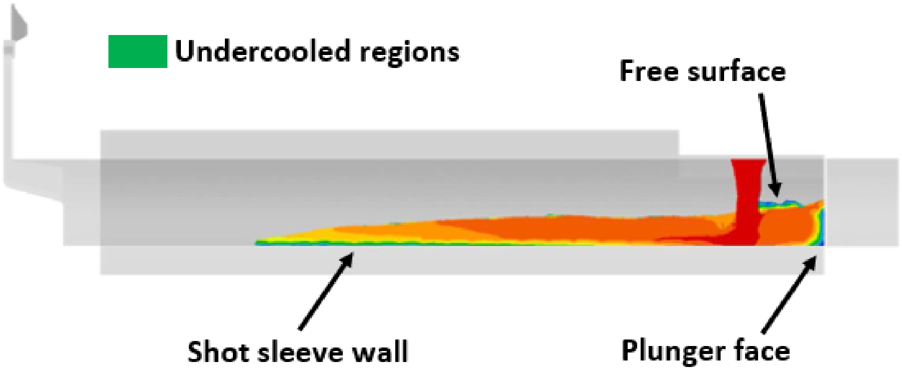

**Figure 34:** Representation of the zones favorable for ESC formation in the shot sleeve [46]

First, in the cold chamber HPDC process, the melt can lose a substantial amount of heat during transportation, resulting in a lower pouring temperature than the holding temperature. To study the impact of the initial melt temperature, researchers often delay the pouring action. For instance, Wu et al. [47] conducted experiments on pouring delays (*Figure 35*) and demonstrated that heat loss prior to pouring leads to a non-linear increase in both the quantity and size of ESCs.

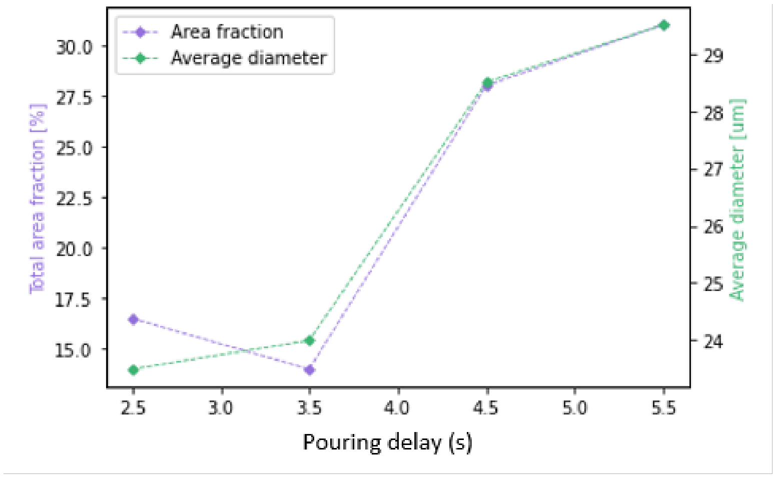

**Figure 35:** Effect of pouring delay on ESC formation during the filling stage [47]

Second, the experimental results from five independent studies are collected in *Figure 36* illustrate the influence of slow shot speed on the total area fraction and diameter of ESCs. It is clear that increasing plunger velocity leads to a reduction in both the quantity and size of ESCs in the final microstructure. These findings suggest that limited retention time inhibits the nucleation and growth of ESCs by decreasing the total superheat loss of the melt. Additionally, Cheng et al. [48] observed that higher slow shot speeds result in a more dispersed distribution of ESCs throughout the casting. However, regardless of the magnitude of the slow shot speed, the sweeping action of the plunger consistently creates a gradient of ESCs in the melt, extending from the plunger's face to the injection end of the shot sleeve. As a result, the gradient of ESCs generated during the filling phase significantly affects the injection stage. This gradient along with sampling locations together with differences such as the pouring temperatures may explain in part the large difference observed between studies.

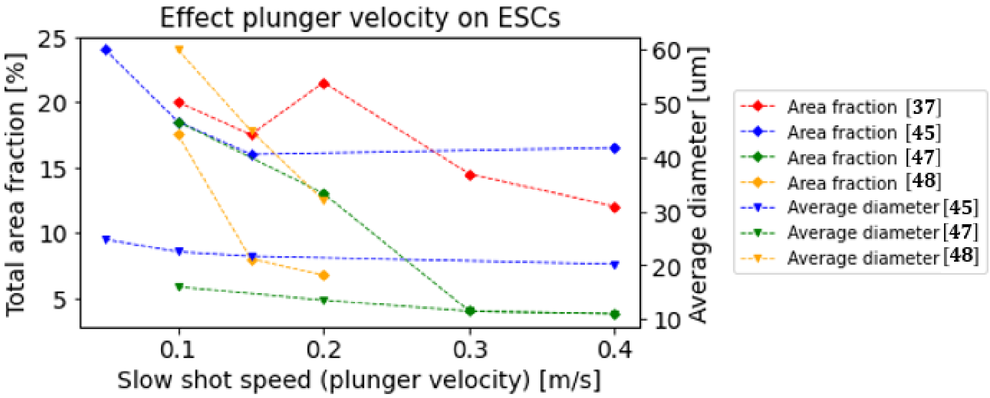

**Figure 36:** Effect of slow shot speed on the total area fraction and average diameter of ESCs [37, 45, 47, 48]

Based on the information presented in this section, it can be concluded that plunger velocity has the greatest influence during the slow shot stage of the HPDC process. It must be slow enough to limit gas entrapment while also being fast enough to prevent the formation of ESCs [34]. It is worth nothing that ESCs solidify directly at the shot sleeve interface are referred to as coldflakes, but are out of the scope of this project.

### 1.4.4 INJECTION IN THE DIE CAVITY

The second step in the HPDC process involves injecting the melt into the die cavity, commonly referred to as the fast shot stage. This stage begins when the plunger reaches the fast shot set point, at which point it accelerates to the fast shot speed, which can be five to ten times faster than the slow shot speed. This acceleration increases turbulence in the melt, resulting in a reduced temperature gradient within the material through increased mixing. The melt is then forced through the runner-gate system until the cavity is completely filled, leading to a high flow rate (*Figure 37*). The runner is the pathway that channels the molten metal from the shot sleeve to the gate, while the gate has a thinner cross-section (in HPDC) and serves as the boundary between the runner system and the die cavity. In practice, the injection phase concludes when pressure begins to increase due to the packing of the melt within the die cavity [32].

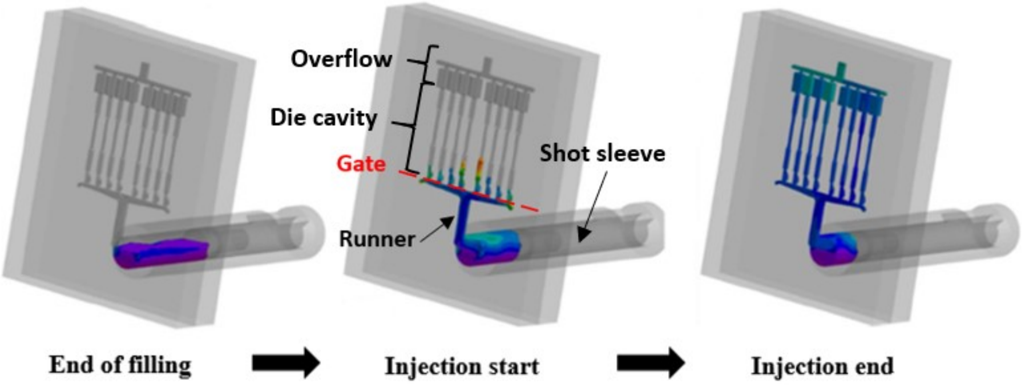

**Figure 37:** Finite element model of the injection phase in the HPDC process [46]

During the injection stage of the process, several key parameters influence performance, including plunger velocity (or fast shot speed), the design of the runner-gate system, the geometry of the die cavity, and the initial mold temperature. Additionally, the ESC gradient in the shot sleeve, generated by the plunger's sweeping action during the filling stage, must also be considered. These factors affect the following microstructural characteristics:

1. The morphology, size, and distribution of ESCs
2. The final size and area fraction of gas porosities
3. The solidification of the skin layer

**Influence of injection parameters on porosities:**

Similar to the filling stage, porosities formed during the injection phase are primarily caused by gas trapped in the melt due to turbulence. These turbulences are generated as the melt is forced into the die cavity considerably more complex than the one presented in *Figure 37*. Key process parameters influencing the intensity of the turbulence include the fast shot speed, runner design, and die cavity geometry. Understanding how these parameters affect metal flow is crucial for minimizing the final proportion of porosities.

By the end of the filling stage, the liquid has already become turbulent due to the plunger's sweeping action. However, Adamane et al. [49] observed that at a fast shot velocity approximately 10 times the slow shot speed, the residual turbulence from the filling stage is insignificant on porosity formation. Additionally, studies by Ghomashchi [50] and Gunasegaram et al. [51], shown in *Figure 38*, indicate that increasing the fast shot speed significantly higher than the slow shot speed leads to a decrease in the area fraction of porosities. Therefore, if the fast shot velocity is sufficiently higher than the slow shot speed, the filling of the shot sleeve has negligible influence on gas porosities. Nevertheless, the absolute amount of porosity is highly dependent on the die design, sampling location or other process parameters.

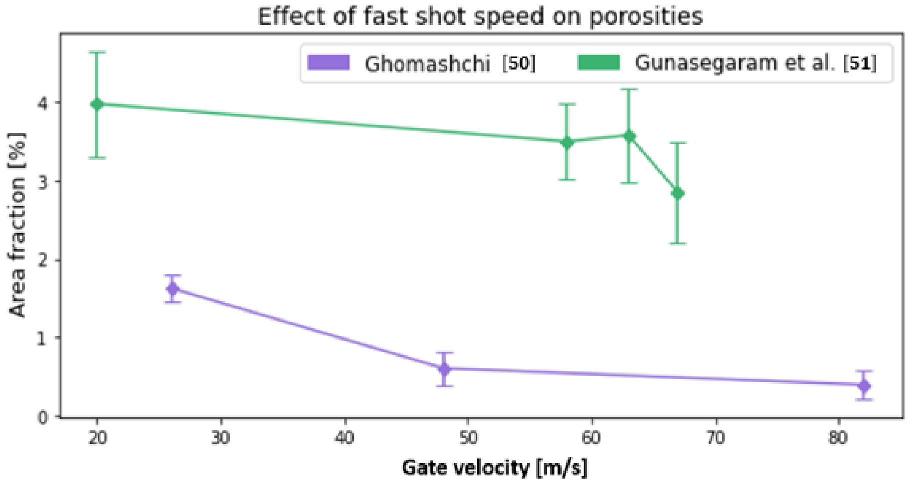

**Figure 38:** Effect of high fast shot speeds on the total area fraction of porosities [50, 51]

Other studies have indeed shown that the design of the runner-gate system and the geometry of the die cavity are significant factors. The runner-gate system must be designed to reduce turbulence, minimize filling time, and shorten the melt flow length [49]. For instance, the gate geometry  aspect ratio can cause a high degree of atomization in the metal flow for a specific range of velocity, leading to a higher level of porosity [52]. Therefore, the plunger velocity has to be adjusted to operates at a gate velocity in a range that results in the optimal material flow. In addition to the runner-gate system, the casting geometry can result in complex metal flow within the die cavity. In such cases, fluid streams can collide during injection, creating additional porosity in those regions [53].

The results shown in *Figure 39* demonstrate that increasing the fast shot speed does not always lead to a reduction in porosity throughout the casting. For example, at location $L_4$ of this specific product, the area fraction of porosity decreases, while at location $L_3$, an increase is observed. Furthermore, the average area fraction of porosity across all locations does not show a clear correlation with fast shot speed. Therefore, it is crucial to understand the impact of fast shot speed on metal flow patterns to effectively limit the gas porosity levels that result from the injection stage of the process.

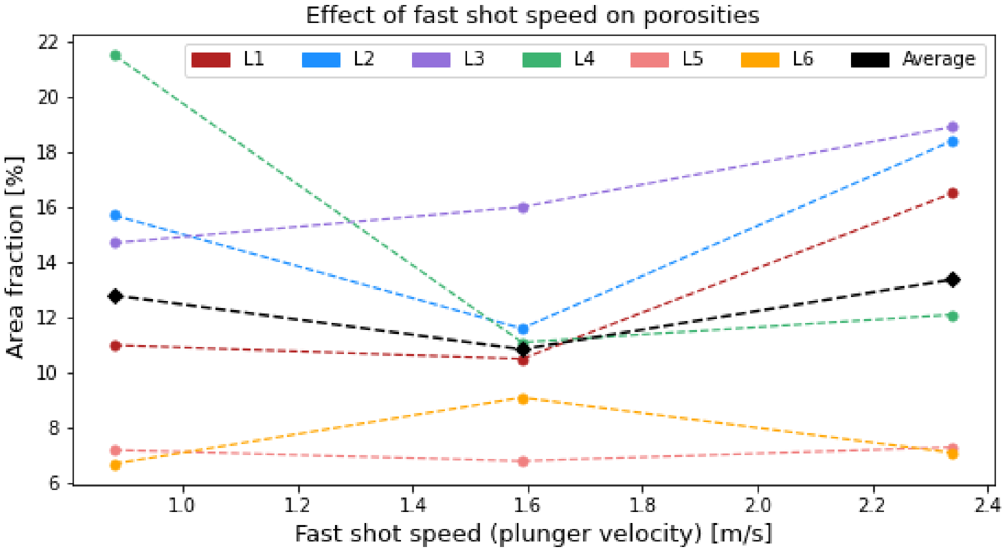

**Figure 39:** Effect of die cavity complexity and fast shot speed on porosities [53]

**Influence of injection parameters on ESCs:**

The final characteristics of the ESCs are heavily dependent on the parameters of the injection phase. It has been demonstrated that this stage of the process significantly influences the distribution, morphology, and average size of the ESCs.

The distribution of ESCs in the final product is influenced in two primary ways. First, the initial gradient of ESCs in the shot sleeve leads to an increasing solid fraction in the injected material over time, resulting in a decreasing gradient of ESCs from the gate to the overflow in HPDC parts [8]. For instance, the specimen shown in *Figure 40* clearly illustrates a higher concentration of ESCs near the gate area, which is the last section to be filled for this specimen geometry.

Second, the combination of temperature variation in the melt and the high flow rate during die filling generates hydrodynamic forces, such as Marangoni and Stoke's motions, which are hypothesized to cause the segregation of ESCs toward the middle section of the casting [54]. The Marangoni motion is caused by the temperature gradient between the die surface and the melt. Stoke's motion relates to gravity and explain the movement of solid particles in a flow of liquid based on their size and the viscosity of the liquid matrix. Stoke's motion becomes more significant as the particles size increases and the viscosity of the liquid matrix decreases. Furthermore, Jiao et al. [55] observed that lower fast shot speeds results in further development of the solid networks between ESCs in the central area of the castings. Conversely, increasing the fast shot speed results in a more dispersed distribution of ESCs. While the exact mechanisms are not fully understood and quantified, regardless of the fast shot speed, ESCs tend to agglomerate in the core section of HPDC products.

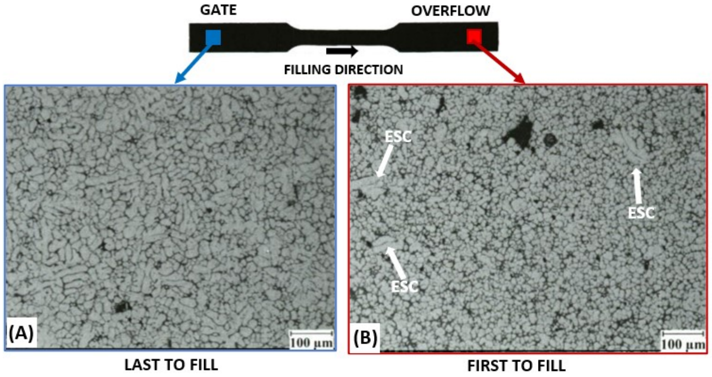

**Figure 40:** ESC gradient resulting from the injection phase of the HPDC process [8]

The size and morphology of ESCs are also influenced by the parameters of the injection phase. Initially, the increased velocity of the plunger causes dendritic ESCs (*Figure 41A*) to be swept into the superheated liquid, resulting in mixing. This mixing can lead to partial remelting of some ESCs before injection [8], in the limited time during which injection occurs (generally less than 100 $ms$ in thin-walled structural high-pressure die casting). When the melt is forced through the thin gate, the high flow rate creates intense shearing of the ESCs. This brief period of intense shear can result in both fragmentation and remelting of the ESCs. Fragmentation alters the morphology from dendritic to elongated trunks (*Figure 41B*), while remelting transforms them into a globular shape (*Figure 41C*). These effects become more pronounced as the solid fraction in the melt increases, leading to a microstructure characterized by a range of sizes and morphologies of ESCs [56].

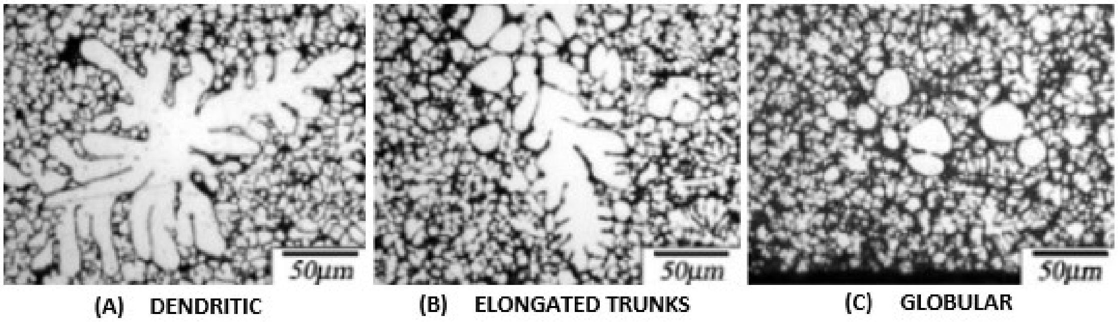

**Figure 41:** Possible ESC morphologies resulting from flow conditions during the injection stage [56]

In addition to influencing their distribution, higher fast shot velocities also influence the quantity and size of ESCs. Similar to the filling stage, increasing the fast shot speed reduces retention time and may decrease the amount of ESCs formed before melt gets into the cavity. While elevated fast shot speeds enhance convection within the melt and facilitates the remelting of ESCs during the initial phase of injection, the duration of this phase and the time available for remelting remains very short. Fast shot speed also determines the intensity of the shear rate to which ESCs are subjected [44], and may therefore have a more significant impact on the size and morphology of individual ESC instances in the casting.

Regarding size variation, Jiao et al. [55] found that higher fast shot speeds lead to a decrease in both the average diameter and area fraction of ESCs (*Figure 42*). However, Zhang et al. [57] observed that this trend holds true except near the surface, where the opposite occurs (*Figure 42*). This could be explained by the influence of higher turbulence level on ESCs distribution.

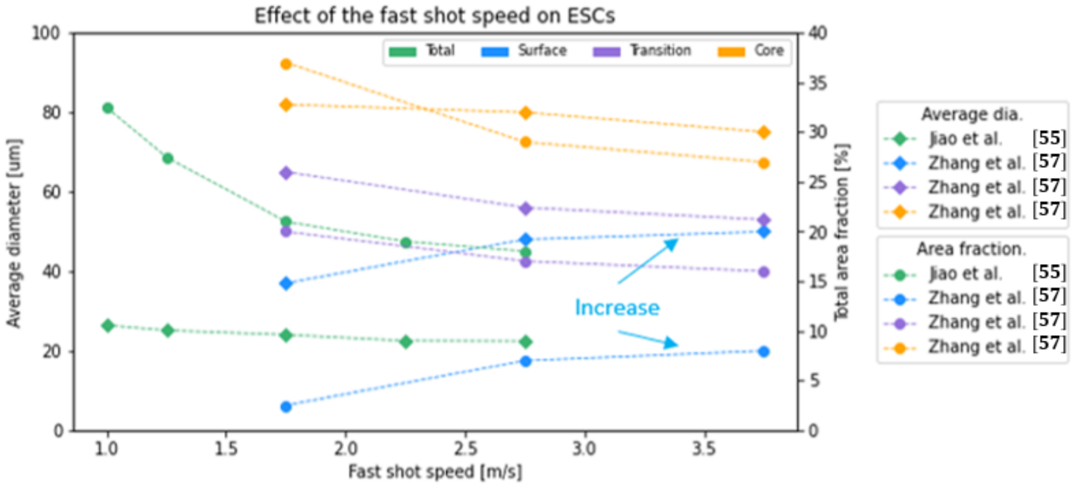

**Figure 42:** Effect of fast shot speed on the average size and distribution of ESCs [55, 57]

**Influence of injection parameters on the skin layer formation:**

One notable characteristic of HPDC is that solidification results in a distinct sub-surface microstructure known as the skin layer. This skin layer is a microstructural feature often identified as being porosity-free and having a finer scale compared to the core or bulk material (*Figure 43*) [58].

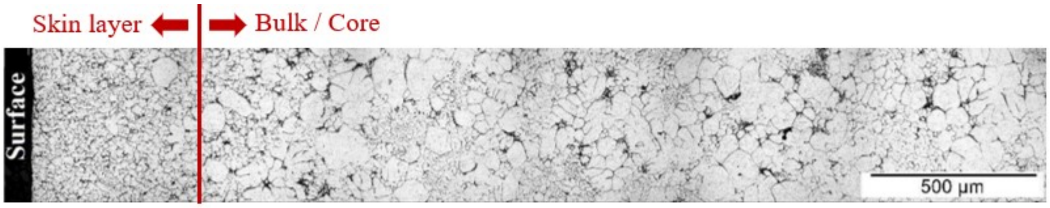

**Figure 43:** Opitcal microscopy image of a cross-sectional view highlighting the distinct transition between the core and skin layer in HPDC products [59]

The characterization of the skin layer in an Al-Si-Mg alloy, as illustrated in *Figure 44*, indicates that its composition and scale can vary. These compositional differences are believed to arise from the local in-cavity conditions during solidification. Otarawanna et al. [8] and Chen et al. [58] hypothesized that the flow, temperature and pressure conditions before and after the effective phase of pressure intensification led to the morphologies depicted in *Figure 44A* and *Figure 44B*, respectively. Additionally, Chen et al. proposed that the α-Al-rich layer (*Figure 44C*) forms as a result of the solidification conditions while pressure intensification is active and effective.

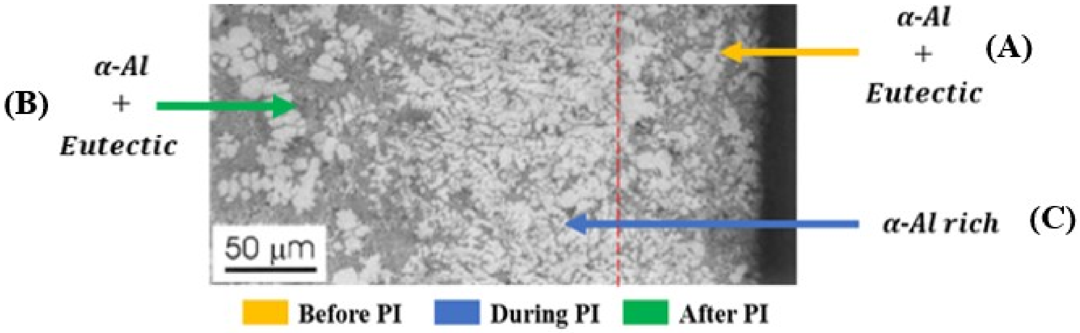

**Figure 44:** Optical microscopy images illustrating the possible compositions within the skin layer in HPDC components [58, 60]

The geometrical complexity of typical die-cast products generally leads to a range of melt-to-die impact conditions throughout the casting, depending also on the runner design. During injection of the melt into the die cavity, the material impinges on the die surface at different angles and velocities, leading to heat transfer from the melt to the die [58]. Chen et al. described three categories on impingement conditions:

1) In areas of direct impingement (*Figure 45A*), heat transfer is significantly greater due to the continuous influx of high-temperature melt. As a result, the local die temperature in these regions becomes elevated during the injection stage. Furthermore, any crystals that form in these areas are believed to be carried away by the flow of the melt. Consequently, regions of direct impingement prevent skin solidification until the end of the pressure intensification stage, as long as the melt continues to flow.

2) In contrast, regions of indirect impingement result in less significant heat transfer to the die during filling (*Figure 45B*) due to near-parallel flow with minimal impact pressure with the die surface. After the melt first contacts the die surface, subsequent impingement on the die wall reduces the intensity of the heat transfer and the temperature does not increase as much as in zones of direct impingement. In addition, if the flow intensity reduction is substantial enough, the melt can achieve effective levels of undercooling before the onset of pressure intensification and a solid network can solidify at the die surface without being washed away (*Figure 44A*). The other variations in skin layer compositions (*Figure 44B* and *Figure 44C*) have been hypothesized to solidify during and after the pressure intensification stage of the HPDC process [8, 58]

3) Finally, some zone in the casting results in very little impingement (*Figure 45C*). These zones represent dead ends in the casting geometry of surface that only comes in contact with the material after it already lost significant amount of heat. Consequently, the die temperature in these zones remain close to its initial value. In this case, solidification is believed to start before pressure intensification and results in a relatively thick solid network at the interface (*Figure 44A*).

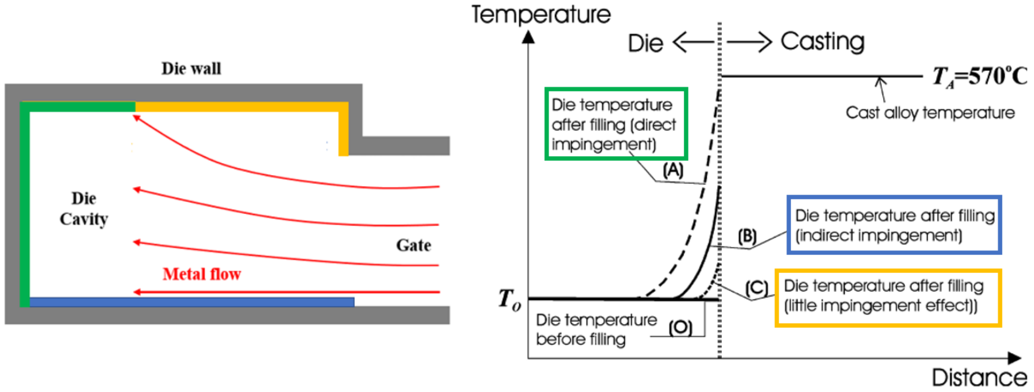

**Figure 45:** Schematic representation of direct (A), indirect (B) and little (C) impingement zones during melt injection into the die cavity [58]

## 1.4.5 PRESSURE INTENSIFICATION STAGE

The final stage of the HPDC process is the pressure intensification phase. At the end of the injection stage, the packing density in the die cavity opposes the plunger motion injecting additional melt. This resistance to the plunger's movement causes an increase in pressure, marking the beginning of the pressure intensification phase (*Figure 46A*). When a given pressure is exceeded, the control logic of the die casting machine switches from velocity (or position) control to pressure control. This is often described as the switchover point. The plunger raises the pressure to a specified level and maintains it to promote proper feeding of material during solidification (*Figure 46C*) [61]. The plunger motion during this stage is generally referred to as the intensification stroke. Depending on the machine configuration, pressure spikes or delays (Figure 46B) may occur as the die casting machine engages successive accumulators.

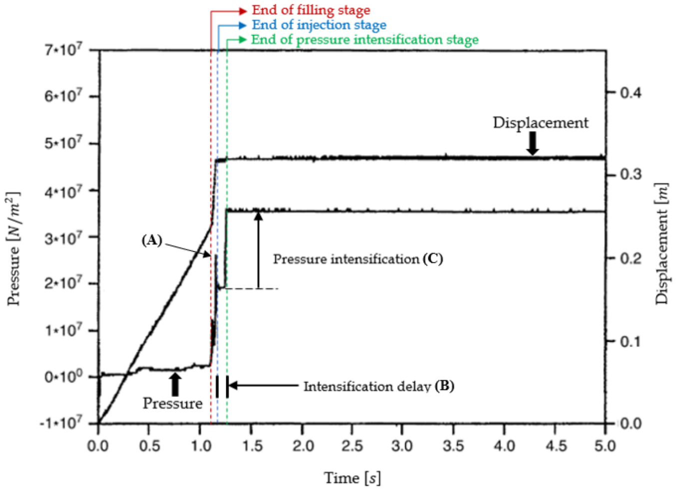

**Figure 46:** Plunger displacement and pressure curves for the HPDC process [61]

In practice, solidification of the thin gate area signifies the end of the effective phase of pressure intensification inside the cavity. As the gates solidify and ESCs concentrate at the gate, the flow of material is impeded and the in-cavity pressure decrease. Once the gate is fully solid, the flow of material ceases, the pressure intensification becomes ineffective, and the remaining liquid continues to solidify [61]. Although the effective phase of pressure intensification may only last much less than 1 second when gates are thin (other die casting variants do utilize thicker gates favouring longer effective intensification), it plays a crucial role in determining the distribution and formation of the microstructural characteristics observed in HPDC products such as shrinkage porosities (*Figure 47*).

During this stage of the process, the key parameters include the intensity of pressure intensification, the design of the runner-gate system, the geometry of the die cavity, and the temperature of the die. Additionally, the accumulation of ESCs throughout the system, resulting from the two previous stages, must be considered.

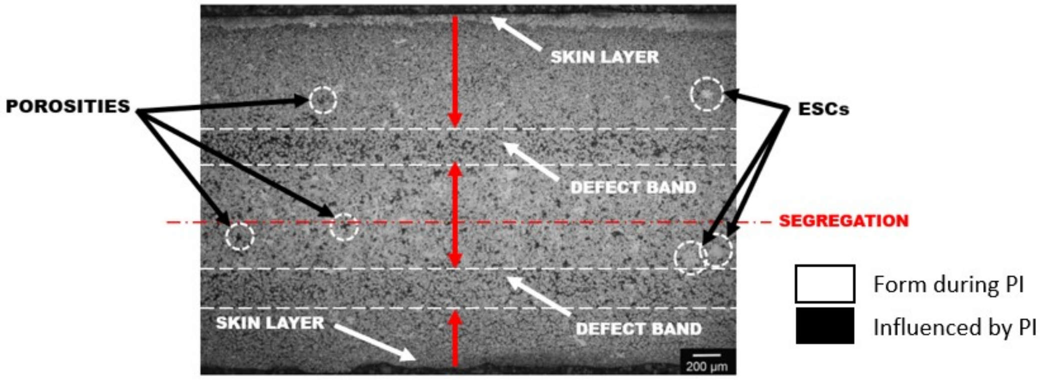

**Figure 47:** Microstructural characteristics of AlMg5Si2Mn alloys resulting from the HPDC process (adapted from [60])

**Influence of pressure intensification on porosities:**

Pressure intensification is the most influential stage of the HPDC process in terms of the distribution and quantity of porosities, especially shrinkage porosities, in the castings. Tsoukalas [42] estimated that pressure intensification accounts for 41.83% of the process's impact on porosity formation. The effectiveness of this stage in reducing porosity depends on factors such as the intensity of the applied pressure, the material's feeding mechanism through the gate, and the evolution of the solid fraction in the gate area. It is important to note that shrinkage porosities result from in-cavity solidification, while gas porosities are introduced during the filling and injection stages of the process.

In general, higher pressure intensification set points increase the effective pressure magnitude and application time on the solidifying material. The greater the pressure, the longer it takes for the gate solidification to overcome the plunger's effort to feed material into the casting (*Figure 48A*) [49].

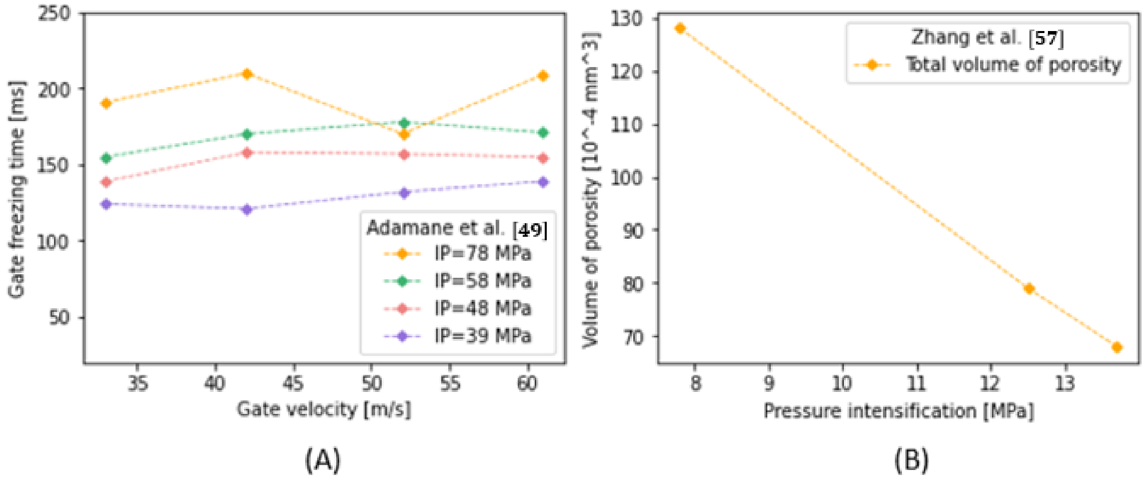

**Figure 48:** (A) Effect of pressure intensification on gate freezing time [49]. (B) Effect of pressure intensification on the porosity volume [57]

Additionally, longer exposure to higher pressure intensification increases the packing density within the cavity, improving the material's feeding during solidification. As a result, a larger proportion of shrinkage porosities are eliminated and gas porosity size is reduced before the casting fully solidifies (*Figure 48B*) [57].

Beyond the intensity of pressure intensification, the final size and distribution of porosities also depend on the design of the runner-gate system and the die cavity geometry. Experiments by Otarawana et al. [62] concluded that the feeding mechanism is influenced by both pressure intensity and gate size. The interaction of these two factors can cause intense shear of the material as it is forced through the gate. This shearing promotes the mechanism causing the migration of the solid particles to the center of the material flow. Consequently, the outside region of the flow becomes a zone with increased liquid fraction (between the die and the center region). The liquid enriched outside layer has a low resistance to shear, which facilitate the transport of material with higher solid fraction toward the end of the injection phase (*Figure 49A*). As a result, both filling and pressure intensification are more effective, which reduces the final proportion of porosity (*Figure 49B*).

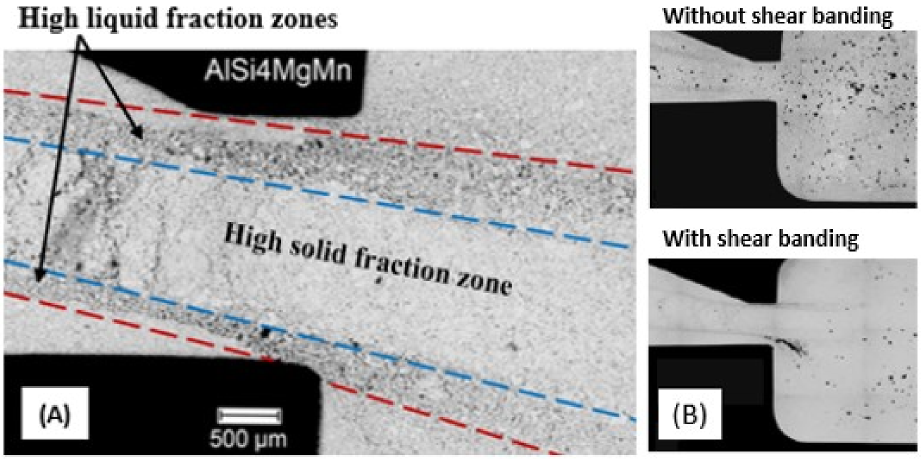

**Figure 49:** Effect of shear on the feeding mechanism:(A) Illustration of the flow pattern resulting from shearing at the gate. (B) Impact of shear during feeding on the final porosity level [62].

Otarawana's results [62] also show that decreasing the gate size is most effective at higher pressure intensification values. As illustrated in *Figure 50*, without any pressure intensification, a 1 $mm$ gate size reduction and same velocity decreased the porosity level by 46.7%. At pressure intensification levels of 13 MPa and 61 MPa, the impact of gate size contributes to a reduction of 78.2% and 77.6%, respectively. These findings suggest that a thinner gate and higher-pressure intensification intensity can be favorable for reducing porosity levels for a given casting geometry. In addition, it supports that intense shear at the gate helps to increase the efficiency of the cavity filling. However, the reduction difference between pressures of 13 MPa and 61 MPa suggest that further increases in pressure would have little additional effect.

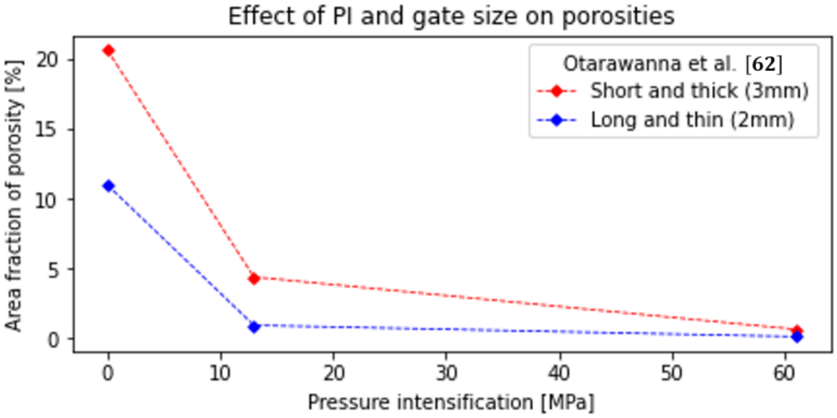

**Figure 50:** Influence of pressure intensification and gate size on feeding [62]

In addition to reducing porosity levels, Otarawanna's experiment [62] demonstrated that the feeding mechanism also affects the microstructural characteristics near the gate area. Specifically, if intense shear occurs and the solid fraction in the flow is too high, late-stage solidification can lead to the formation of cracks, pores, and eutectic pockets (*Figure 51*).

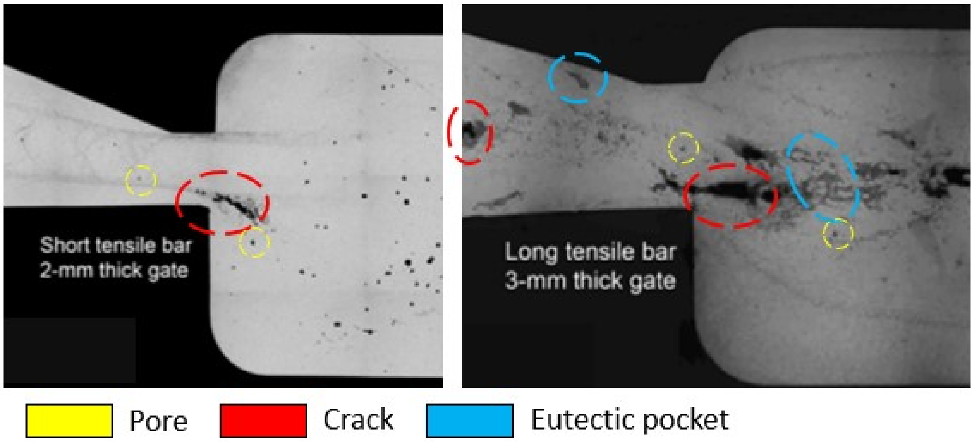

**Figure 51:** Effect of shearing on the near-gate microstructure during late-stage solidification [62]

Although pressure intensification is beneficial for reducing porosity levels, the geometry of the die cavity can create complex flow patterns that result in less effective feeding in certain areas of the casting. For example, Sharifi et al. [45] observed that increasing the intensity of pressure intensification can cause a localized increase in porosity (*Figure 52*), especially in zone not directly aligned with the preferential material flow path. They hypothesized that, while increasing pressure intensification greatly reduces the quantity of porosities, the remaining defects tend to accumulate in last to fill, last to solidify and knit line locations.

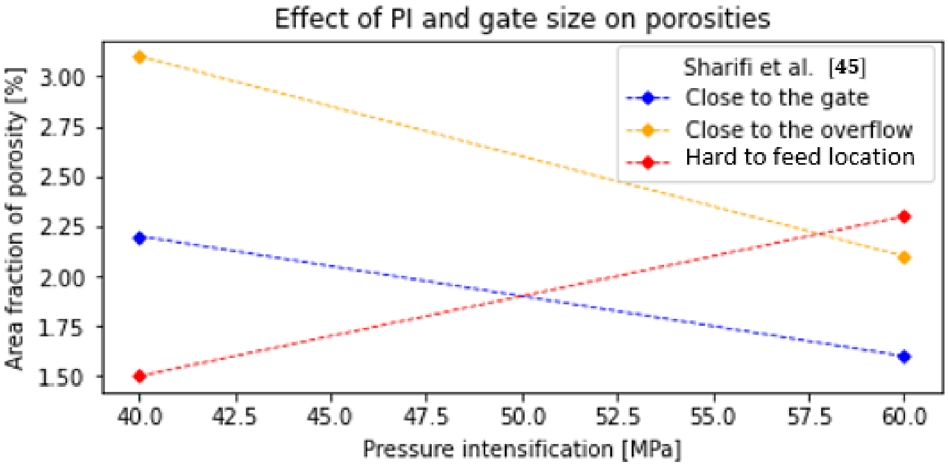

**Figure 52:** Effect of die cavity geometry on material flow and porosity formation [45]

**Influence of ESCs during pressure intensification:**

During the effective phase of pressure intensification, the ESCs are subjected intense pressure. While material flow within the cavity is still occurring, pressure intensification can lead to further fragmentation. Furthermore, increasing the intensity of the pressure results in a 9 to 14 % reduction in both the total area fraction and the average diameter of the ESCs (*Figure 53*) [57].

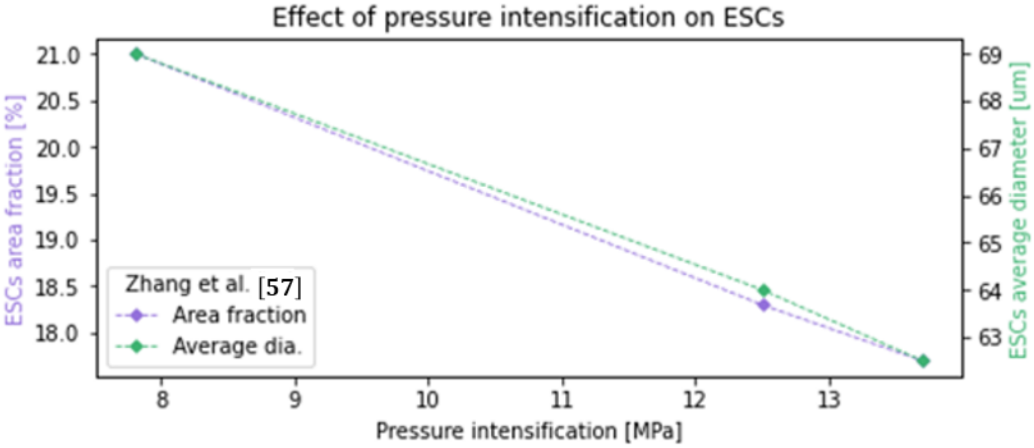

**Figure 53:** Effect of pressure intensification on the size and distribution of ESCs [57]

## 1.4.6 COUPLED FLOW AND SOLIDIFICATION BEHAVIOUR

In addition to the direct impact of pressure intensification and the previous stages on ESCs, their distribution within the die cavity also affects the feeding and solidification of the material. To gain a better understanding, it is essential to consider how the solid fraction influences the material's mechanical response. *Table 4* outlines the two solid fraction limits that result in a change in mechanical response. Both limits cover a wide range as it will vary significantly between locations within a casting as well as between alloy systems.

**Table 4:** The solid fraction thresholds that lead to a change in the mechanical response of the semi-solid material [63-65]

| Name | Limit | Description |
|---|---|---|
| Coherency point | $0.1 \leq f_s^{Ch} \leq 0.3$ | Transmission of stresses between solid particles. Shear strength development in the material. |
| Maximum packing fraction | $0.3 \leq f_s^{Pk} \leq 0.6$ | Dendrites grow and become sufficiently large to interlock such as they can no longer reorient. Shear strength of the material becomes much greater and development of tensile strength can be possible. |

Before the coherency point is reached, the flow of material is considered a suspension of solid crystals in liquid [65]. During this brief period, ESCs can disrupt the flow and feeding of the material in three ways [66].

1. Choking of the flow at the entrance of the runner
2. Choking of the flow at the thinner part of the runner-gate system
3. Choking of the flow in specific location in the die cavity

The various choking mechanisms can lead to pressure drops, halting the feeding of material and locally promoting the formation of a solid network [66]. As indicated in *Table 4*, the formation of these solid networks signifies that the material has reached the coherency point ($f_s^{Ch}$). In this state, dendrite reorientation within the solid network is still possible if pressure is applied. Consequently, the high pressure resulting from forcing material inside the cavity compresses the well-developed ESC networks, forcing liquid out toward the die wall and low solid fraction zones. This mechanism plays a crucial role in the shear banding mechanism, which is believed to cause the segregation/defect band and microstructure variation within the skin layer, as it facilitates the segregation of liquid from the center to the surface of the casting [67].

Finally, when the solid fraction reaches the maximum packing fraction ($f_s^{Pk}$), the strength of the solid networks significantly increases. As a result, the material injected at a later stage of the process is forced through channels of lesser solid fraction (around the solid network). In addition, if the pressure applied on solid networks that reached the maximum packing fraction is too high, shear cracking can occur in the later stages of the solidification process. Such crack may be visible in the final microstructure. Additionally, cracks can still form due to the traditional hot-tearing mechanism, which arises from material shrinkage during solidification [8].

### Formation of the segregation band:

The segregation band (or defect band) is a common microstructural feature observed in HPDC products. It consists of a band-like region of segregation that forms during the injection and pressure intensification phase. Typically, segregation bands follow the contour of the casting; however, they may not be uniform or present in all areas (*Figure 54*) [8].

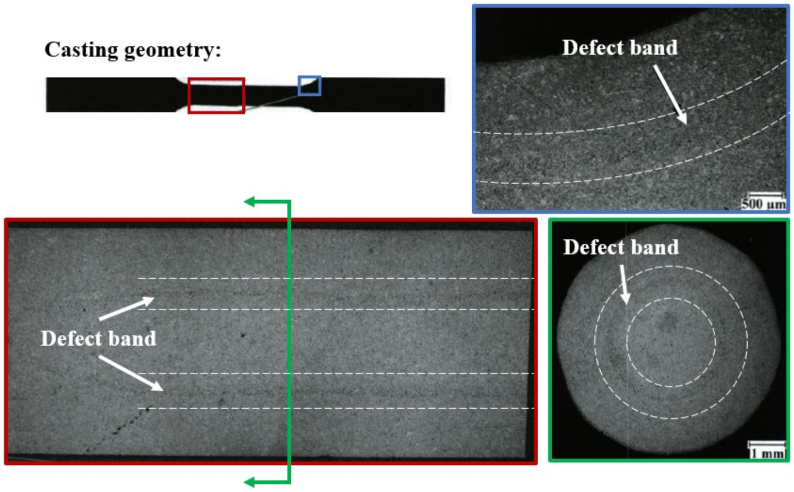

**Figure 54:** Segregation band in AlSi4MgMn cylindrical tensile test specimen prepared by HPDC [8]

For a segregation band to form, the solid fraction in the center section of the casting must be sufficiently high prior to the pressure intensification stage [67, 68]. When this occurs, the liquid material begins injected inside the die cavity is forced through low solid fraction channel between the surface and central solid networks (the segregation bands). As more material is being forced through these channels, shear stresses develop at the interfaces between the solid networks and the liquid flow, causing dilatant shear banding to starts. As depicted in *Figure 55A*, forcing material through these channel causes dilatation. If the surrounding solid network has a solid fraction lower than the maximum packing density, solute rich liquid segregates outside the network toward the band or the die surface. As a result, dilatant shear banding creates band-like region containing a higher proportion of solute-rich liquid (positive macrosegregation) (*Figure 55B*).

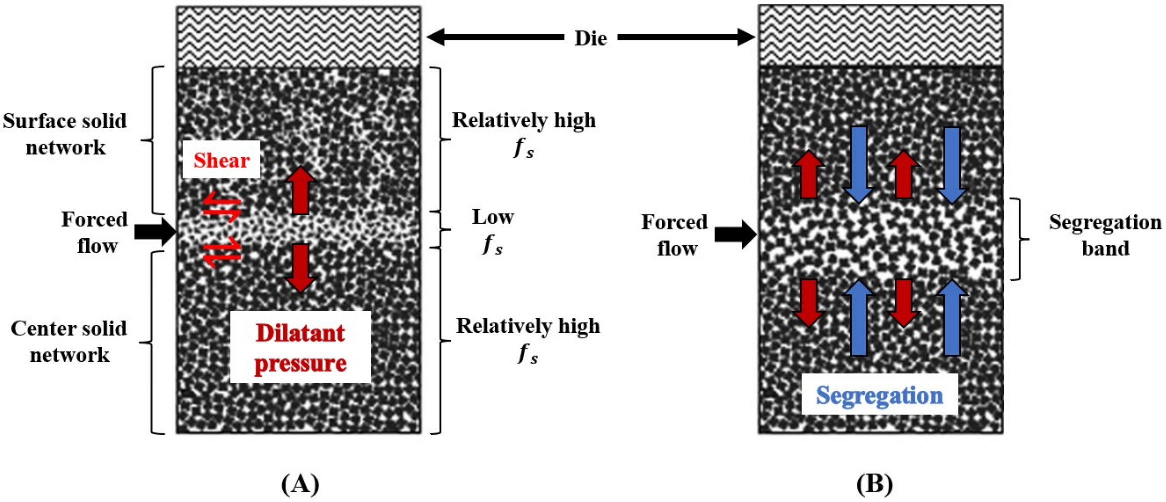

**Figure 55:** Representation of the dilatant shear banding mechanism (adapted from [60])

Upon complete solidification, the dilatant shear banding leads to the formation of band-like zones with a high eutectic proportion between the center and surface solid networks and at the die interface that can readily be observed by low-magnification optical microscopy (*Figure 56*) [8].

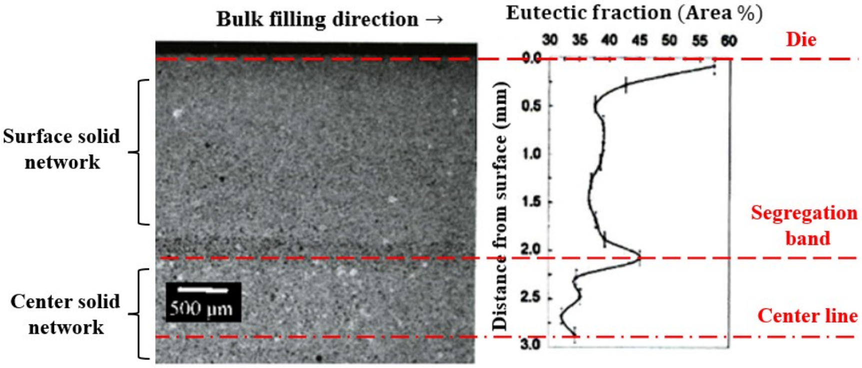

**Figure 56:** Typical segregation band in the microstructure of AlMg5Si2Mn produced by HPDC [8]

Casting conditions can influence both the composition and the position of the segregation band. One of the most significant factors is the die temperature, which can either shift the location of the segregation band or prevent its formation altogether. Gourlay et al. [67] observed in gravity castings that increasing the die temperature moves the position of the segregation band closer to the die interface (*Figure 57A*). Furthermore, it was noted that no segregation band forms when the die temperature exceeds 350°C. This can be explained by the effect of die temperature on the thermal gradient at the die wall and the solidification gradient within the die cavity. A high die temperature would delay the development of a solid network at the surface. If solidification is delayed long enough, it prevents the occurrence of dilatant shear bending between solidifying solid networks.

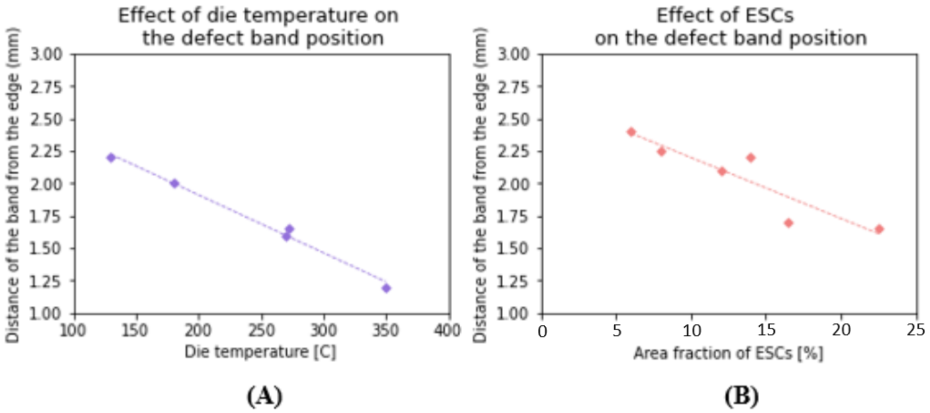

**Figure 57:** (A) Effect of die temperature on the position of the segregation band relative to the surface in gravity castings. (B) Effect of the proportion of ESCs on the position of the segregation band relative to the surface [67]

In addition to die temperature, any parameters that influence the formation of ESCs and their accumulation in the central region of the casting can impact the formation of the segregation band. As previously mentioned, a critical solid fraction in the central section must be reached during the injection stage for a segregation band to form. Therefore, controlling the level of ESCs affects segregation band formation. Moreover, an increased area fraction of ESCs leads to the band moving closer to the die surface (*Figure 57B*) [67]. As more ESCs accumulate in the center region, the central solid networks become thicker. Consequently, the interface between the center and surface solid networks moves closer to the die surface.

Finally, the combination of alloy composition and casting parameters can influence both the structural features and composition of the segregation band. As shown in *Figure 56*, the band typically contains a high proportion of eutectic, but other characteristics can vary significantly. First, the composition of the alloy affects the porosity level in the band. For instance, Al-Mg alloys tend to produce segregation bands with a high proportion of porosity, whereas Al-Si systems result in a porosity-free defect band with a significant proportion of eutectic constituent [8]. Second, the interaction between material flow and pressure intensification during solidification can produce directional features and varied morphologies of eutectic networks (*Figure 58*) [67].

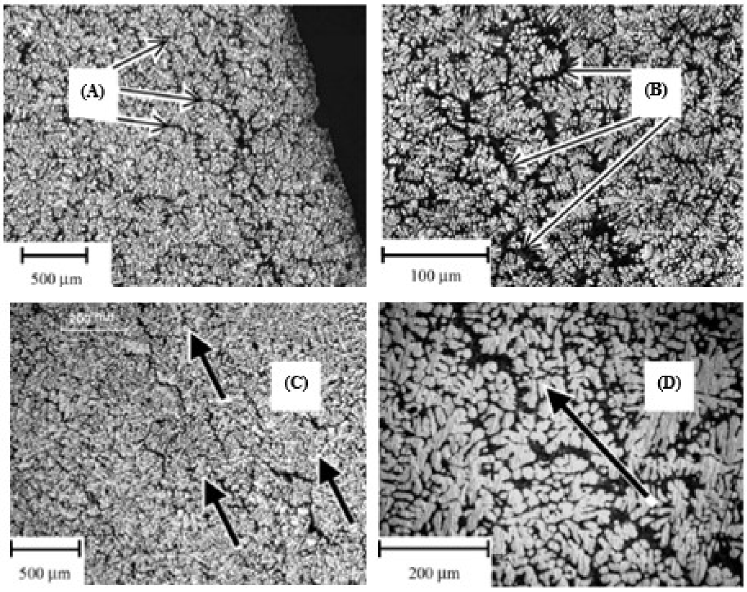

**Figure 58:** (A) Eutectic tributaries leading to the defect band. (B) Interconnected eutectic pathways. (C) and (D) Directional eutectic pathways aligned with the slip path during band formation [67]

**Solidification of the skin layer:**

Despite its well-known existence and technological importance, formation of the skin layer is one of the least studied microstructural characteristics of HPDC products. As mentioned in the segregation band formation section, the in-cavity conditions during solidification are believed to influence the characteristics of the skin layer. Specifically, local conditions that lead to material solidification are affected by the intensity and orientation of the melt's impingement and slipping on the die wall during the injection stage and the effectiveness of the pressure intensification phase [8, 58].

During injection, the temperature, velocity and impact angle of the melt influence the level of impingement with the die wall, which results in varying levels of heat extraction through the die surface. Initially, prior to pressure intensification, zones of indirect impingement can achieve significant levels of undercooling, leading to the solidification of fine primary aluminum and eutectic constituents (*Figure 59A*) [58]. The microstructure of the skin layer in these zones results from rapid solidification, which is driven by higher heat extraction and the inability of the melt flow to displace the solidifying crystals [8].

Second, the formation of the primary aluminum-rich skin layer is believed to solidify during the brief effective phase of pressure intensification (*Figure 59B*). It has been concluded that this type of skin layer is associated with zones experiencing low-impact (LI) direct impingement of the material. However, the exact mechanisms leading to the significantly higher proportion of primary aluminum observed in these areas have yet to be identified.

In contrast, the absence of a skin layer (*Figure 59C*) is associated with zones of high-impact (HI) impingement. In these regions, strong impingement heats up the die surface significantly and sweeps away the solidifying crystals during the injection stage. Consequently, the conditions for solidification are only met after the effective phase of pressure intensification, that is, just prior to the freezing of the gate [58]. As a result, the microstructure in these areas exhibits a coarser primary aluminum and eutectic composition. Given that solidification in these zones occurs after the effective phase of pressure intensification and, heat extraction through the die wall is not as effective as it is during the earlier stages of injection, when the die temperature has not increased yet. This explains the differences in microstructural scale between zones that solidify before and after the effective phase of pressure intensification.

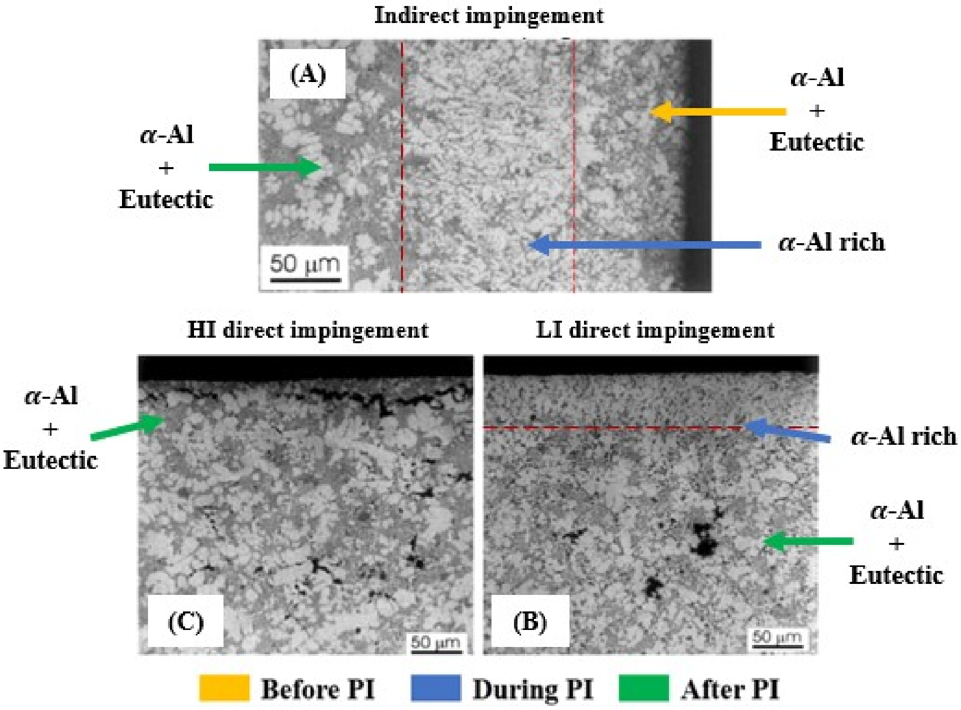

**Figure 59:** Optical microscopy images illustrating the potential skin layer compositions of the Al-11Si-2Cu-1Fe alloy produced via high-pressure die casting (HPDC) [58]

**Conclusion:**

Based on the literature reviewed in this chapter, it is evident that while the relationships between process parameters and porosity and externally solidified crystals have been extensively investigated, our understanding of the in-cavity conditions during High-Pressure Die Casting (HPDC) remains incomplete in terms of rapid phase changes and near-surface microstructure formation. From a solidification standpoint, conventional solidification models are inadequate for predicting the proportions of microstructure constituents. The conventional solidification models do not account for the solidification condition during HPDC. From a process perspective, our knowledge of how turbulent in-cavity material flow influences microstructure formation is still incomplete. The ability of experimentally measuring in cavity conditions is a considerable challenge to achieve. As a result, we need the necessary tools to accurately predict microstructure development during HPDC, which would facilitate efficient design of new high-integrity components.

# CHAPTER 2
# EXPERIMENTAL METHODOLOGY

The discrepancy between phase distributions predicted by conventional solidification models and experimental observations underscores the need for a solution tailored to rapid solidification and turbulent processes. The first part of the experimental methodology focuses on exploring rapid solidification theories and models, with the goal of adapting the conventional equilibrium phase diagram to better reflect the conditions of rapid solidification in Al-Si alloys. The modified phase diagram is then compared to experimental results to assess its accuracy. The second part aims to characterize near-surface microstructure variations within HPDC components and evaluate their impact on bending ductility for simple components. The findings from this analysis will help quantify how local microstructure variations influence performance and can guide further investigations or improvements.

## 2.1 ALLOYS AND CASTING

The castings for this study were produced using high-pressure vacuum die casting (HPVDC) at the National Research Council Canada [69]. The casting cell is equipped with a 530-ton Bühler SC N/53 cold-chamber die casting machine, which featured automated metal ladling, spray functions, and a Fondarex vacuum system. During the experiments, the molten metal was held in an electrically heated crucible furnace, fluxed with a Wedron metal treatment system, and degassed with argon gas. The die face operated at temperatures of approximately 250-260°C, with a relatively small amount of die lubricant applied. The HPDC plates analyzed in this study were manufactured using three different die geometries and alloys. *Table 5* lists the compositions of the Aural™-2 and Aural™-5 alloys used in this investigation. All components have been analysed under as cast conditions (F temper).The specimens from both Aural™-2 and Aural™-5 castings had similar wall thicknesses, measuring 3.0 mm and 2.5 mm, respectively. Both alloys have been used to investigate the consequence of rapid solidification. However, only the Aural™-2 castings, for which the geometries are illustrated in *Figure 60*, were used for the subsurface microstructure analysis. The simple plate (*Figure 60A*) was used to focus on the characterisation of the subsurface variants and the more complex casting

(*Figure 60B*) was used to analyse how the casting geometry influences subsurface microstructure formation.

**Table 5:** Average composition of Aural™-2 and Aural™-5 alloys tested

| **Element** | | **Wt.%** | | | | | | |
|---|---|---|---|---|---|---|---|---|
| | | **Al** | **Si** | **Mg** | **Fe** | **Mn** | **Ti** | **Sr** |
| **Alloy** | Aural™-2 | Bal. | 10.6 | 0.30 | 0.19 | 0.50 | 0.06 | 0.013 |
| | Aural™-5 | Bal. | 7.26 | 0.20 | 0.17 | 0.49 | 0.04 | 0.018 |

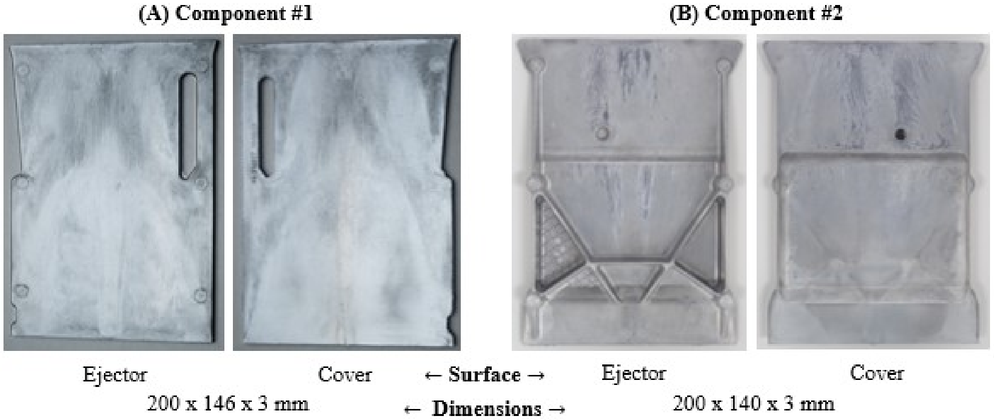

**Figure 60:** HPVDC Aural™-2 castings used for subsurface microstructure characterization

## 2.2 MICROSTRUCTURE CHARACTERISATION

All samples collected from the HPDC components in this project were prepared using standard metallographic grinding and polishing procedures. Following cutting and grinding, polishing was carried out with diamond pastes of particle sizes 6, 3, and 1 μm, each applied for 10 minutes to get the best finish possible without pulling out the intermettallics from the microstructure. A final polishing step was performed using colloidal silica with a particle size of 0.5 μm for 5 minutes. Once prepared, micrographs of the general microstructure and local variations were acquired using a Nikon Eclipse ME600 optical microscope under 200x magnification. All images were processed using a the same image analysis routine to quantify the distribution of the primary constituents within the microstructure. Sample batches from different casting campaigns were analyzed to obtain the necessary statistical representation. This method also enables the categorization of the local microstructure variation types based on the samples' positions within the components.

### 2.2.1 IMAGE ANALYSIS ROUTINE

A Clemex® image analysis routine was employed to segment the microstructure using grayscale thresholding to separate its constituents (*Figure 61A*). The eutectic constituent was identified by its gray appearance in the micrographs, while the aluminum crystals appeared white. To distinguish between the two aluminum crystal populations (alpha-Al and ESC), a threshold of 200 µm² was applied, with externally solidified crystals (ESCs) recognized as white objects larger than 200 µm². Following segmentation (Figure 61B), the analysis routine calculates the area fraction of each constituent within the image, along with the average crystal area for both the primary aluminum phases (α-Al and ESCs) and the eutectic phase. It is important to note that intermetallic phases and porosities were excluded from the analysis, as they fall outside the scope of this project.

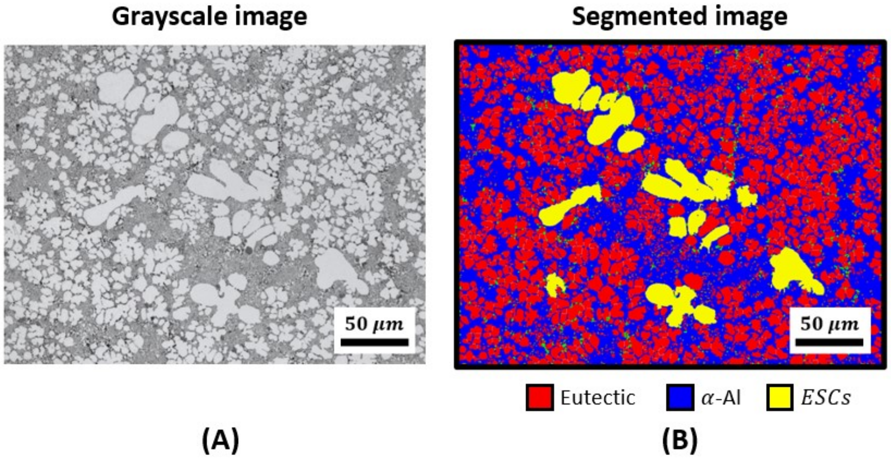

**Figure 61:** Clemex® image analysis routine, (A) after grayscale thresholding, (B) after segmentation

### 2.2.2 RAPID SOLIDIFICATION

To evaluate the experimental eutectic area fraction resulting from rapid solidification, five as-cast plates of each alloy were sectioned into multiple samples. A total of five specimens were prepared from different locations along the material flow in each plate, enabling an assessment of the overall eutectic area fraction in the components. The same sampling strategy has been used for this analysis. Micrographs were captured from the core and skin regions. The images selected for analysis were taken according to the pattern shown in *Figure 62* and analysed with the image analysis routine detailed previously.

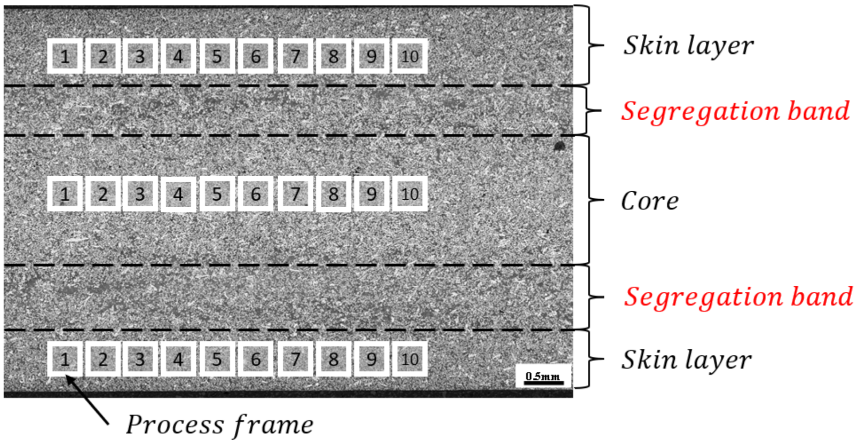

**Figure 62:** Methodology for acquiring micrographs for microstructure characterization in the different regions of the HPVDC Specimens

This study investigates the discrepancy between the experimentally measured eutectic fraction and the predictions from the theoretical equilibrium/Scheil models and new proposed models. To evaluate the eutectic area fraction for each specimen, images from three distinct regions outside the segregation bands were analyzed, and their area fractions were summed, as illustrated in *Figure 62*. This method focuses the analysis on the solidification response of the material. However, it may slightly underestimate the overall eutectic fraction, as segregation bands are enriched in eutectic at the expense of the surrounding areas, as discussed in Section 1.4.6.

The as-cast microstructure in HPDC results from a two-stage solidification process, where solid crystals form at a slower cooling rate under more conventional conditions in the shot sleeve before being injected into the cavity. To account for this filling phase, two adjustments were made. The first adjustment involved modifying the image analysis routine to exclude the contribution of ESCs from the total area fraction, as these crystals did not solidify under rapid solidification conditions. This modification allowed the analysis to focus on calculating the eutectic fraction of the fine, rapidly solidified material only. The second adjustment related to the composition of the liquid phase used in the rapid solidification model. Specifically, it recalculated the composition of the remaining liquid after the ESCs solidified, prior to the injection phase. Evaluating the actual ESCs fraction in the component is a considerable challenge as some ESCs do not enter the die cavity but still consume solute elements as they solidify. For that reason, a solid fraction of 20% wt. ESCs, at a temperature just above the eutectic, was assumed to determine the ESCs composition. While the true ESC fraction in the component may differ from this value, it was used as a reference point for the analysis.

### 2.2.3 SUB-SURFACE MICROSTRUCTURE

The as-cast plates were sectioned into multiple samples for metallographic analysis, taken from regions near the gate, center, and overflow zones to capture the evolution of the sub-surface microstructure along the material flow direction, as shown in *Figure 63*. A preliminary analysis was performed to ensure the sample locations captured all sub-surface variant types. As-polished samples from five plates were used for the microscopy analysis conducted in this study. The through-thickness microstructure was captured from the samples' cross-sections using 350x200 μm images, spanning from the ejector to the cover surface (*Figure 64A*). Additionally, the sub-surface microstructure was captured with 350x20 μm images, extending up to 300 μm from the surface to obtain a better resolution on the gradient (*Figure 64B*). All images were processed with the image analysis detailed in this chapter.

For both the through-thickness and sub-surface characterizations, at least five locations per sample were analyzed for statistical sampling. The objective of this analysis was to assess the change in microstructure composition between the core and the skin layer, as well as the local variations at the die interface (sub-surface).

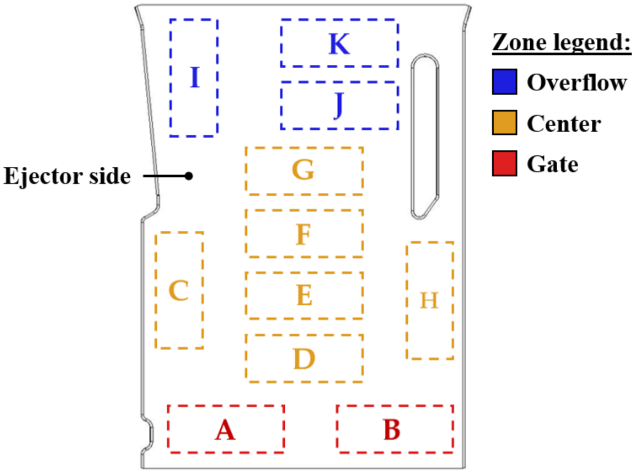

**Figure 63:** Sample positioning on the ejector side of the HPVDC casting

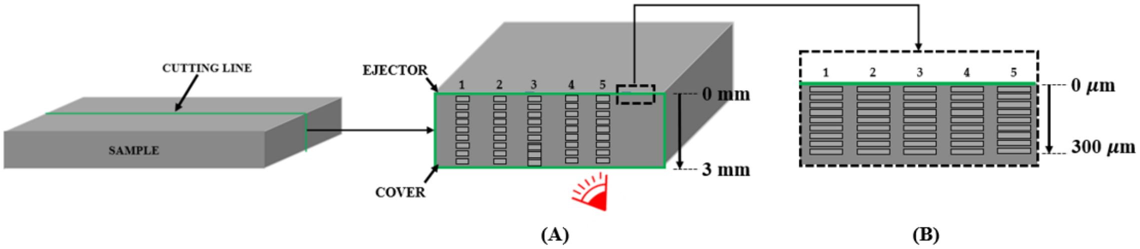

**Figure 64:** Sampling and analysis methodology for the calculation of the main constituents. distribution:(A) through the plate's thickness and (B) in the first 300 $\mu$m from the surface

## 2.2.4 INFLUENCE OF DIE GEOMETRY AND MATERIAL FLOW

The objective of this experiment is to validate the hypothesis of Chen et al. [58] in regard to the role of impingement of the material flow with the die surface on the subsurface microstructure formation. As presented in *Figure 65*, two sections of component #2 (*Figure 60B*) were selected to characterise the subsurface microstructure along the material flow direction. The first location (*Figure 65A*) is considered of simple geometry and is a continuous transition from a flat section of 3 mm to a flat section of 2.5 mm. In the second section selected (*Figure 65B*) the material flow is split in two branches at the junction with the ejector tower, which is assumed to result in a more turbulent material flow.

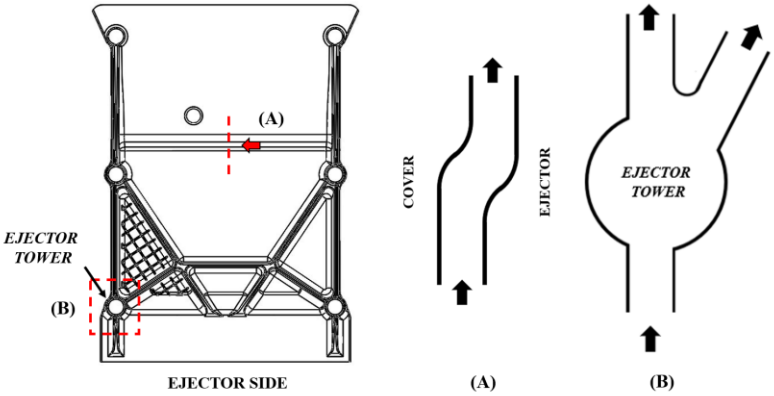

**Figure 65:** Section used for the flow impingement analysis: (A) Simple geometry section, (B) Complex geometry section at the parting plane

## 2.3 RAPID SOLIDIFICATION MODELING

To assess the influence of rapid solidification processing on the area fraction of the main constituents, two rapid solidification models accounting for variations in solidification front velocities (SFV) were identified and have been presented in the literature review chapter of this document. The considered models were programmed with Python. Data from ThermoCalc was used for the calculation of a modified phase diagramme that account for the solidification front velocity (SFV).The first model, proposed by Pierantoni et al. [23], is based on rapid planar growth (approach 1), while the second, from Trivedi et al. [27], is based on rapid dendritic growth (approach 2). To evaluate the validity of these models, eutectic fraction predictions for the Al-Si system were calculated using both approaches. SFV-dependent phase diagrams were generated to determine the eutectic fraction prediction over a wide range of velocities. These predictions were then compared to the experimentally measured eutectic fraction to assess whether either approach is suitable for HPDC applications. The most accurate model was subsequently selected to further investigate the influence of increasing SFV on the composition and distribution of the main constituents.

To define the Al-Si system, the liquidus and solidus lines, eutectic composition, and eutectic temperature from the aTCAl7 database in ThermoCalc (version 2022a) were used. Additionally, *Table 6* presents the physical properties of the Al-Si system necessary for generating the modified phase diagrams taken from the literature.

**Table 6:** Physical properties of the Al-Si system used in the non-equilibrium phase diagram [23]

| Property | Symbol | Value | Units |
|---|---|---|---|
| Diffusion pre-exponential coeff. (Si in Al) | $D_0$ | $1.64 \times 10^{-7}$ | $m^2/s$ |
| Diffusion activation energy (Si in Al) | Q | $25740$ | $J/mole$ |
| Gas constant | R | $8.314$ | $J/(mole.K)$ |
| Solid-liquid interface length | $a_0$ | 1 | nm |

## 2.4 BENDING DUCTILITY PERFORMANCE EVALUATION

The bending performance was evaluated in accordance with the VDA 238-100 Tight Radius Bend Test using an MTS RT100 mechanical testing machine and a VDA test fixture from Zwick/Roell (*Figure 66*). The bend test specifications included a nominal punch radius of 0.4 mm and a roller gap of 6.8 mm, which remained consistent across all tests. Tests were conducted at the National Research Council Canada.

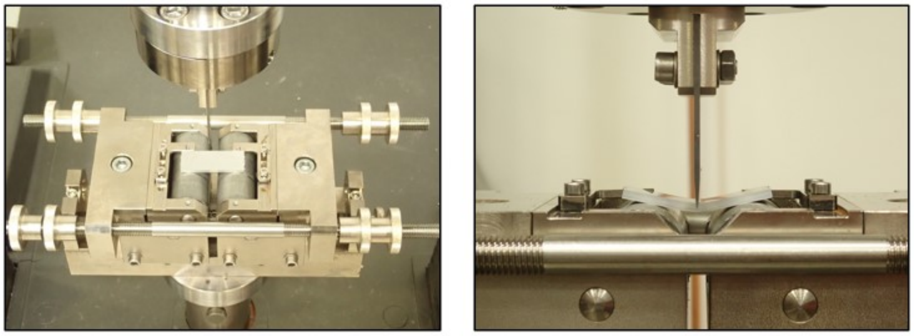

**Figure 66:** VDA bending test set up

The samples used in this experiment were 20x50x3 mm in size and were machined based on the sample locations outlined in *Figure 63*. Subsize samples have been used in order facilitate the inclusion of a single sub-surface variant in the test zone. In total, twelve plates were machined. On each plate, eleven specimens were tested for both the ejector and cover faces.

Following the bending test, the bent samples underwent preparation for optical microscopy using the previously outlined methodology. This analysis aims to establish a correlation between the sub-surface microstructure and the bending performance of each of the samples. Therefore, particular focus was placed on analyzing the distribution of constituents within the first 300 µm from the surface in the bending samples, close to the fracture location.

# CHAPTER 3
# RESULTS AND DISCUSSION

This chapter presents the results for both key issues addressed in this work. The first two sections emphasize the heterogeneity of the microstructure, providing results on the distribution of the main constituents and the characterization of subsurface microstructure variations. The following sections focus on the two primary challenges identified for the project. The rapid solidification approaches discussed in the literature review are compared with the microstructure characterization results to assess their accuracy and identify a model better suited for HPDC applications. Next, the mechanical test results are correlated with subsurface microstructure variations to determine the extent of their influence on performance. Finally, recommendations are made to guide further investigations aimed at bridging the gap between theory and practice.

## 3.1 GENERAL MICROSTRUCTURE CHARACTERISATION

*Figure 67* shows a representative example of the microstructure obtained by HPVDC, highlighting the characteristic regions of the layered microstructure (core, segregation band, and skin layer). As depicted, all the main constituents are clearly distinguishable: externally solidified crystals (ESCs), the primary aluminium phase (α-Al), and the eutectic. Due to the thickness of the castings and the use of vacuum, the amount of porosity was minimal and was not specifically analyzed in this study. Similarly, note that intermetallics are not specifically addressed in this project, but that they are another important feature of the microstructure.

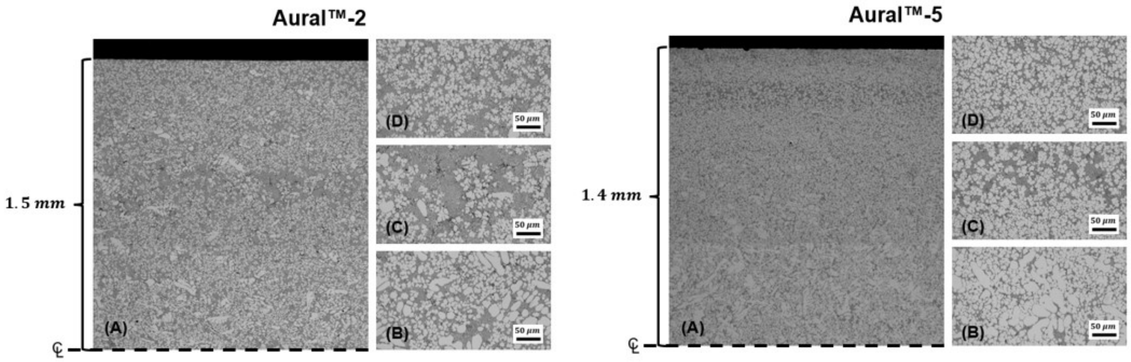

**Figure 67:** Representative microstructure for the HPVDC components: (A) Through thickness microstructure, (B) the core, (C) the segregation band and (D) the skin layer

### 3.1.1 OVERALL EUTECTIC FRACTION

*Table 7* presents the experimental area fractions for the main constituents, along with the adjusted eutectic area fraction that account for the ESCs contribution in consuming the solute element before the material is subjected to rapid solidification conditions. These results are consistent with the literature [8, 70].

**Table 7:** Adjusted main constituents' area fraction based on the optical microscopy image analysis

| **Alloy** | **Liquid Composition** | | **$\alpha$-Al** | **Eutectic** | **ESCs** |
|---|---|---|---|---|---|
| | **Nominal** | ***Adjusted** | | | |
| Aural™-2 | 10.6 | 12.3 | 39.7% | 44.2% | 15.9% |
| | | **Adjusted area fractions* | 47.6% | 52.4% | - |
| Aural™-5 | 7.3 | 8.4 | 49.9% | 34.1% | 15.1% |
| | | **Adjusted area fractions* | 60.0% | 40.0% | - |

*Adjusted according to an assumed ESC fraction of 20%

After excluding the contribution of ESCs, the eutectic fraction increased from 44.2% to 52.4% for Aural™-2, and from 34.1% to 40.0% for Aural™-5. This adjustment accounts for approximately 7% of the eutectic reduction observed under HPDC conditions. Regarding the liquid phase composition adjustment, assuming 20 wt% ESCs solidified just above the eutectic temperature, the solute mass fraction (wt% Si) in the liquid phase increased from 10.6% to 12.3% for Aural™-2 and from 7.3% to 8.4% for Aural™-5.

### 3.1.2 THROUGH THICKNESS DISTRIBUTION

To facilitate result interpretation and characterize microstructure evolution along the material flow direction, samples of the Aural™-2 components illustrated in *Figure 60A* were grouped based on the zones outlined in *Figure 63* (gate, center, and overflow). The decrease in the area fraction of ESCs from the gate to the overflow as well as from the core to the skin layer can be seen in *Figure 68A*. The former is attributed to an increasing solid fraction in the injected material, originating from ESCs accumulating towards the rear end of the shot sleeve, near the plunger face [4]. The latter is a consequence of ESC migration towards the centerline during injection. This migration is believed to result flow dynamics mechanism such as the Stoke's and Marangoni's motions developing in the nonuniform gravity and temperature fields within the highly constrained flow of material [54]. The combined influence of these mechanisms leads to a notable reduction in area fraction within the skin layer. In the current characterization, the skin layer regions in the gate, center, and overflow zones exhibit respective average ESC area fractions of 4.1%, 1.4%, and 1.1%. This finding suggests a potential variation of up to 74% in ESC area fraction within the skin layer of the plate. Note that the error bars in Figure 68 represent the full range of constituent area fractions at each location, rather than the standard deviation, in order to illustrate the complete variability.

Regarding the average individual crystal size distribution of the ESCs, *Figure 68B* reveals that ESC sizes range from 206 μ$m^2$ to 879 μ$m^2$, with no discernible difference between zones and regions. This consistency is coherent with the understanding that ESC modification arises from the intense shear in the runner and gate during injection. Consequently, there is no segregation of ESCs based on size and shape, leading to the stable average ESC size observed in *Figure 68B*.

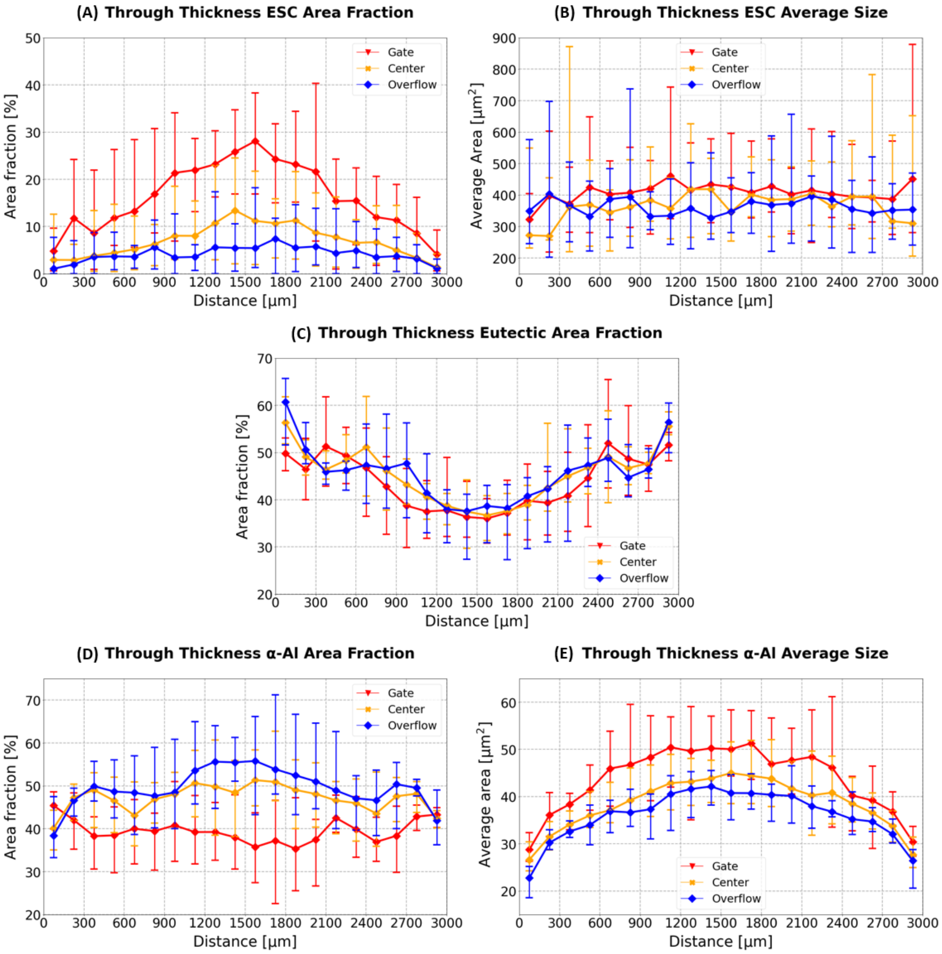

**Figure 68:** Through-thickness distribution of the main constituents: (A) Area fraction of ESCs, (B) Average ESC size, (C) Eutectic area fraction, (D) α-Al area fraction and (E) Average α-Al area

*Figure 68C* presents the through-thickness distribution of eutectic for the three zones considered. The eutectic distribution within the thickness of the samples fluctuates from the skin layer to the core, but appears consistent across all zones, indicating that microstructure variation in the core results from the balance between ESCs and the α-Al phase. Segregation bands are also discernible by the eutectic plateau or peak in regions spanning from 250 to 1000 μm and 2000 to 2750 μm from the cover surface. The defect band in the ejector side seems to shift toward the core as we approach the overflow, while the position of the second defect band remains stable. This observation indicates asymmetrical filling and/or solidification conditions along the center-line. It is expected as the gate and overflow are not centered.

Finally, there is a sharp increase in the eutectic area fraction from the edge of the segregation band to the die interface in some zones. This rise peaks near the ejector surface at 49.8%, 56.3%, and 60.7% in the gate, center, and overflow zones, respectively. Conversely, the maximum eutectic area fraction near the cover surface reaches 51.2%, 55.5%, and 56.4% for the same zones. With ranges of 10.9% and 5.2% for the ejector and cover surfaces, respectively, it is evident that the process leads to asymmetrical conditions in the die cavity. These observations highlight the variability in microstructure composition within the skin layer along both the material flow and through-thickness directions.

As a consequence of the ESC and eutectic distributions, the area fraction of fine α-Al shown in *Figure 68D* increases along the material flow direction in the region encompassing the defect bands and the core (250 to 2750 μm), and an increase is noticeable within the skin layers (0 to 250 μm and 2750 to 3000 μm). These results are consequential to the ESCs and eutectic distribution presented in *Figure 68A*. They underscore the tendency of ESCs to agglomerate in the core region, closer to the gate, as well as the substantial increase in eutectic proportion within the skin layer.

Regarding the average α-Al crystal size distribution, *Figure 68E* clearly demonstrates refinement in both the material flow and through-thickness directions. The average α-Al crystal size decreases from 50 to 41 $\mu m^2$ in the core and from 30 to 23 $\mu m^2$ in the skin layer.

Overall, the observations stemming from this characterization reveal significant variations in the distribution of main constituents within the part. Moreover, the constituent distribution within the skin layers throughout the plate implies a notable alteration in sub-surface microstructure composition, potentially impacting the uniformity of bending performance throughout the plate.

## 3.2 SUB-SURFACE MICROSTRUCTURE CHARACTERISATION

To better understand the impact of turbulent filling on skin layer solidification, samples of the Aural™-2 components illustrated in *Figure 60A* were analyzed to identify potential sub-surface variations within the skin layer.The samples' locations are illustrated in *Figure 69B*. For clarity, in this study, the term "skin layer" refers to the microstructure situated between the segregation band and the die interface, while "sub-surface" denotes a portion of the microstructure within the skin layer in direct contact with the die interface. Consequently, a "sub-surface variant" denotes any recurring sub-surface variation in the microstructure that may arise from fluctuations in local flow or thermal conditions.

Based on *Figure 68*, it was determined that the edge of the segregation band is situated approximately 250 µm from the die interface. Consequently, the sub-surface characterization was conducted within the first 300 µm to capture the constituent distribution within the skin layer region. *Figure 69* illustrates representative examples of the various sub-surface variants and their respective locations; all observed within a single plate.

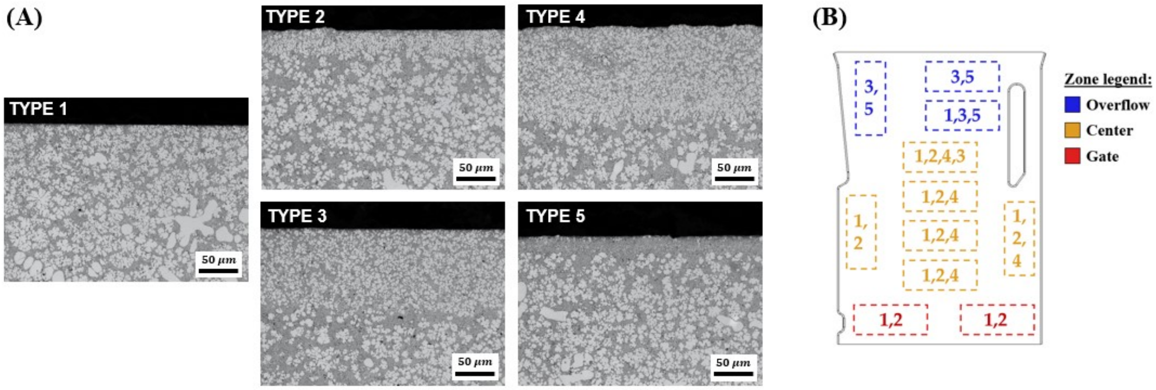

**Figure 69:** Representative sub-surface microstructure variants observed within a single HPVDC Aural™-2: (A) variants micrographs and (B) variants typically observed at each of the test locations on the ejector and cover faces

The sub-surface variant type 1 (*Figure 70*) serves as the reference for absence of sub-surface variation, given its consistent microstructure throughout the entire skin layer. This variant is the most prevalent and has been observed in all locations of the plate except those close to the overflow. According to current understanding, this variant solidifies in zones of direct impingement or high turbulence, where the flow of material applies significant pressure on the die surface during filling. Strong impingement has been observed to limit the formation of a solidified layer or even prevent solidification at the interface altogether [58, 60]. The area fraction of the main constituents for this type of sub-surface variant varies accordingly with the results presented in *Figures 68* and *Figure 70*.

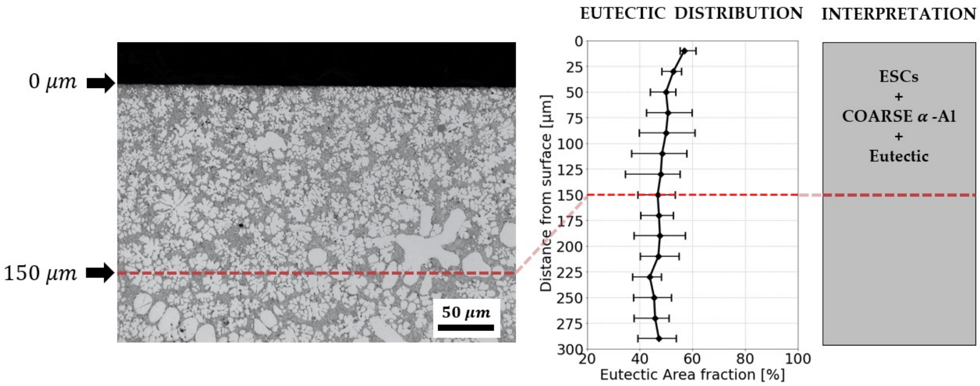

**Figure 70:** Representation and interpretation of the sub-surface variant type 1

The sub-surface variant type 2 (*Figure 71*) is distinguished by an accumulation of α-Al at the die interface. It is typically observed in zones of moderate impingement. The α-Al density at the interface and the presence of a minor defect band suggests the occurrence of dilatant shear banding. This formation could be attributed to the impact of pressure intensification on a solid network with low solid fraction, which develops in moderate impingement zones during injection.

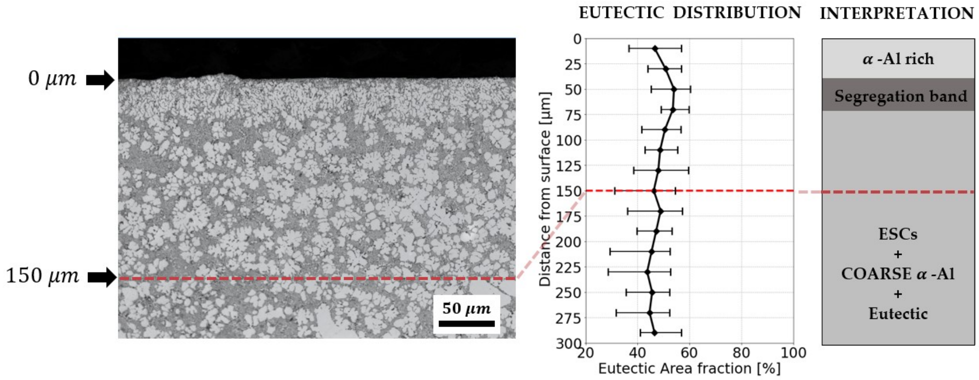

**Figure 71:** Representation and interpretation of the sub-surface variant type 2

The sub-surface variant Type 3 (*Figure 72*) exhibits a relatively thick layer of refined α-Al phase and eutectic followed by a minor segregation band. The initiation of the refined layer from the die interface suggests a variation in thermal conditions that fosters nucleation and solidification at specific locations within the plate. Drawing from the impingement hypothesis proposed by Chen [58]. this sub-surface variant could solidify in zones of low impingement. Under such conditions, a refined and cohesive solid network may form on the surface prior to the pressure intensification phase, thereby resulting in the presence of a minor segregation band between the sub-surface variant and the bulk of the skin layer.

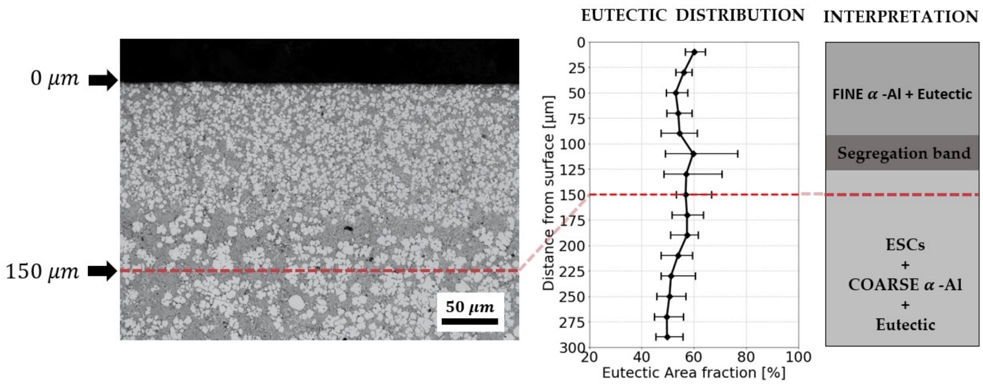

**Figure 72:** Representation and interpretation of the sub-surface variant type 3

The sub-surface variant type 4 (*Figure 73*) combines characteristics observed in types 2 and 3, featuring a refined layer of α-Al followed by an accumulation of coarser α-Al crystals. Notably, in samples where this sub-surface variant was observed, the refined layer consistently lies between the die interface and the accumulation of α-Al crystals. This observation supports the notion that the refined layer at the interface solidifies prior to pressure intensification. Moreover, the locations where sub-surface variants 3 and 4 were observed suggest that the α-Al rich layer is more likely to form toward the gate or high α-Al area fraction zones (*Figure 65B*).

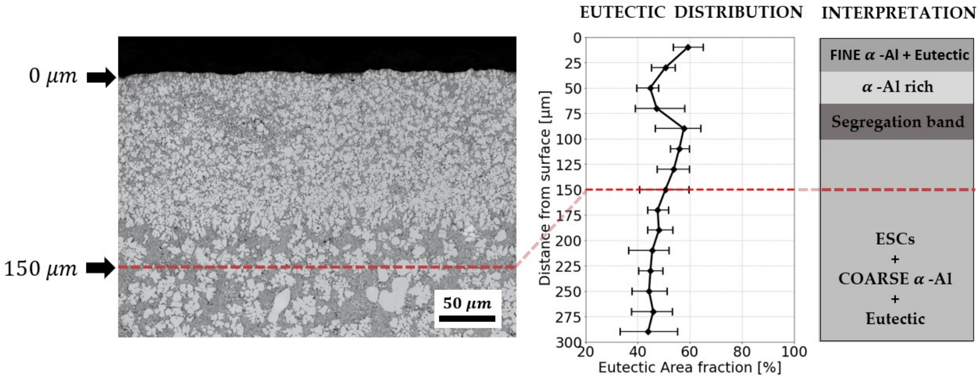

**Figure 73:** Representation and interpretation of the sub-surface variant type 4

Finally, type 5 (*Figure 74*) is characterized by a relatively thin layer of almost pure eutectic at the die interface. Regarding its location within the plate, this variant has only been observed in samples near the overflow (*Figure 63*, I and K). It is likely a consequence of inadequate liquid feeding during the latter stages of injection in zones where solidification shrinkage pulls the solid away from the die interface. It is important to highlight that although this sub-surface variant has been observed previously, there have been no conclusive studies published on its formation.

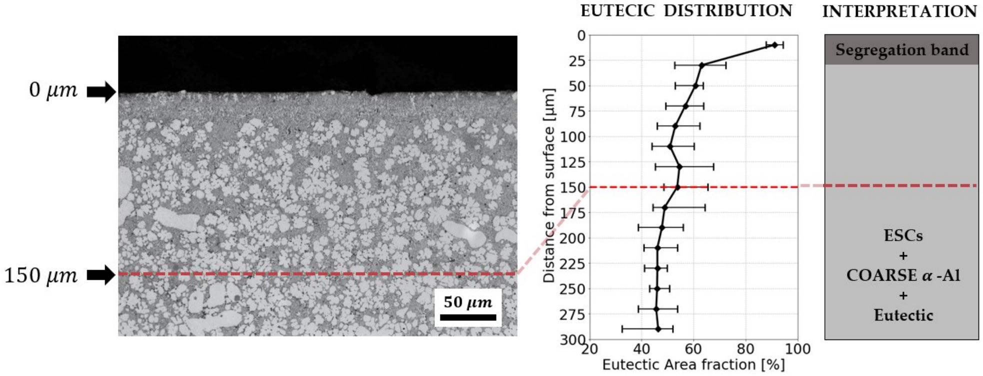

**Figure 74:** Representation and interpretation of the sub-surface variant type 5

The microstructure within the skin layer therefore exhibits significant variation in terms of constituent area fraction and structural organization. Taking into account the findings of this study and those observed by Otarawanna et al. [62] it appears that sub-surface microstructure variations are strongly correlated with the level of impingement of the material flow (or turbulence level) and the role of dilatant shear in the segregation of the liquid phase. Moreover, it is noteworthy that the variation within the skin layer seems to be confined within the first 150 μm from the surface. In the eutectic distributions presented in *Figures 70-74*, the standard deviation within the first 150 µm is 2.16 times higher than in the rest of the skin layer. Based on the microstructure characterization conducted in this study, it is apparent that even geometrically simple HPDC parts are prone to significant local microstructure alterations within the skin layer.

## 3.3 INFLUENCE OF TURBULENCE AND DIE GEOMETRY

As previously discussed, the formation of the subsurface microstructure appears to be strongly influenced by the impingement of material flow against the die surface [60, 64]. While the intensity of material flow is primarily governed by the action of the plunger, the extent of impingement is largely determined by the die geometry. In *Figure 60A*, the component used in the prior experiment features a completely flat design. In contrast, the more geometrically complex component shown in *Figure 30B* is better suited for evaluating Chen's hypothesis, which proposes a correlation between impingement and subsurface microstructure formation.

*Figure 75* presents the subsurface microstructure at different locations within the simple Aural™-2 geometry section (*Figure 65A*). Location A3 is the only one showing a distinct variant of subsurface microstructure, suggesting that it is the only area where impingement is negligible. Specifically, a refined layer of aluminum crystals and eutectic can be observed at the interface (*Figure 69A, Type 3*). This variant is believed to solidify before the intensification of pressure (*Figure 59A*). Furthermore, the type of variant observed at this location correlates with the findings for the casting in *Figure 69*, as most samples taken at similar distances from the overflow exhibited the same subsurface microstructure. Based on the geometry and material flow direction, *Figure 75* show that the position A3 has negligeable impingement while position A2 is the only zone of direct impingement. However, in this geometry, both zones of direct and indirect impingement display the same subsurface microstructure, which is believed to solidify after pressure intensification (*Figure 59C*).

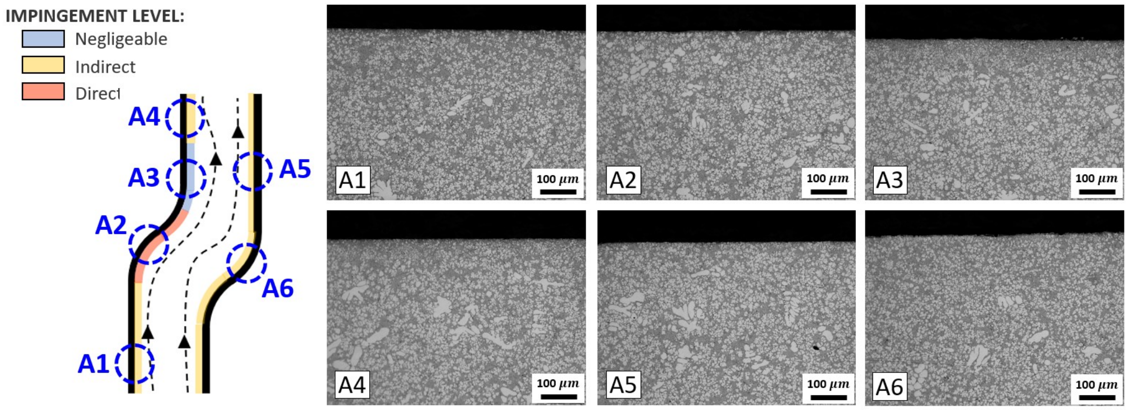

**Figure 75:** Subsurface microstructure evolution along the material flow for a simple geometry section

*Figure 75* illustrates the subsurface microstructure at various locations within the same complex geometry section (*Figure 65B*). As in the case of the simple geometry section, both the direct and indirect impingement zones show no significant variation in subsurface microstructure. Notably, the regions of negligeable impingement display a subsurface variant that is rich in aluminum (*Figure 69A, Type 2*). This variant is thought to solidify during pressure intensification, particularly in regions where the solid fraction lies between the coherency point and the maximum packing density. When the pressure applied to the solidifying network is sufficiently high, the solid particles are compacted, causing the liquid to segregate from the network in areas with a lower solid fraction. Additionally, location B8 (ejector tower) stands out as a high-turbulence zone, given is relatively large volume, and being the only area where porosities are visible.

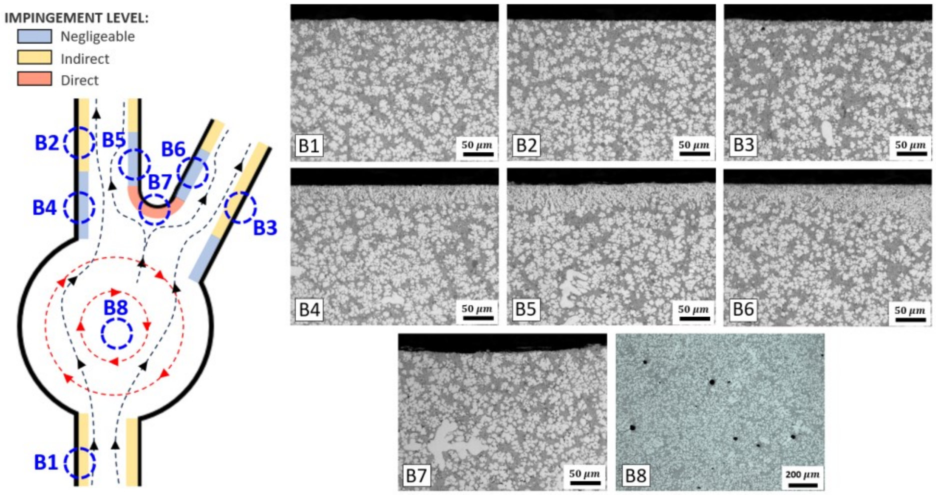

**Figure 76:** Subsurface microstructure evolution along the material flow for a complex geometry section

The observed subsurface variations strongly suggest that geometry plays a significant role in influencing subsurface microstructure formation. Changes in transition and direction can redirect material flow away from the die surface, thereby reducing the level of impingement in specific areas. For instance, in *Figure 77*, an accumulation of aluminum crystals begins immediately after the transition between zones of direct and negligible impingement. This suggests a change in interface conditions within that region.

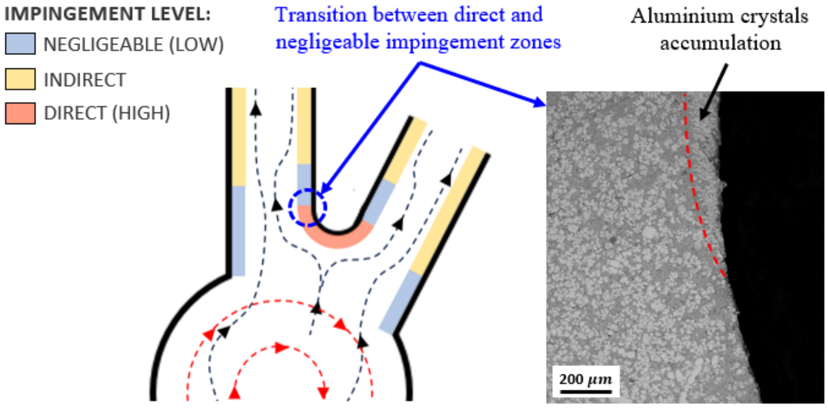

**Figure 77:** Microstructure at the transition between zones of direct and negligeable impingement

These observations clearly indicate that die geometry plays a significant role in shaping the subsurface microstructure. Changes in geometry appear to create zones of negligible (or low) impingement, which foster conditions conducive to solidification at the interface before pressure intensification occurs. While the impingement levels outlined by Chen are somewhat subjectively assigned to the different zones within the geometry herein, it is clear that subsurface microstructure variations are most pronounced in regions where impingement is at its relative minimum within the die cavity.

Additionally, the differences in subsurface microstructure between the two locations further support the idea that local solid fraction and pressure are key factors in the formation of subsurface variants (*Figure 69*, Types 1 to 4). As shown in *Figure 68*, an increase in aluminum crystals has been observed in specimens closer to the gate. Moreover, since in-cavity pressure is controlled by the plunger, any increase in pressure is likely to be more effective closer to the gate than at the overflow. As a result, it is more favorable for the aluminum-rich subsurface layer to be observed nearer the gate rather than the overflow.

## 3.4 RAPID SOLIDIFICATION MODEL

As discussed in the literature review section, conventional models (Equilibrium and Scheil) are not suitable for HPDC as they predict a eutectic fraction around 80%, while the experimental area fraction of the samples analysed in this project is around 52.4% (*Table 7*).

Using the Thermo-Calc database for the Al-Si binary system and the physical parameters listed in *Table 6*, eutectic fraction predictions were calculated for appropriate solidification front velocity (SFV) ranges for both approaches. For an AlSi10 alloy, *Figure 71* shows that the eutectic fraction ranges from 80.8% to 70.9% for Approach 1 (model based on planar growth, section 1.3.2), and from 80.6% to 39.1% for Approach 2 (based on dendritic growth). Based on these results, Approach 2 provides a range of eutectic area fractions and SFVs that are consistent with experimental observations [28, 71-73]. Given the clearly dendritic nature of the as-cast microstructure in HPDC specimens, Approach 2 is deemed the most suitable method for predicting eutectic fractions in HPDC. In contrast, Approach 1 exhibits discrepancies between predicted eutectic fractions and SFVs when compared to experimental results in both HPDC and additive manufacturing [28, 31, 71-76], indicating that this approach is not suitable.

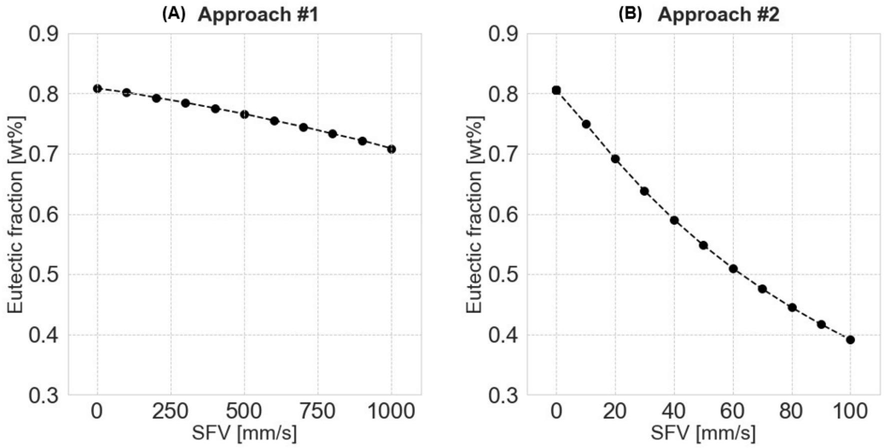

**Figure 78:** Effect of the SFV on the eutectic fraction: (A) approach based in planar growth and (B) approach based on dendritic growth

### 3.3.1 EFFECT OF THE SFV ON THE PHASE DIAGRAM

Based on approach 2, *Figure 79* illustrates the effect of solidification front velocity on the shifts in the liquidus, solidus, and eutectic isotherms for SFVs ranging from 0 mm/s to 200 mm/s. The model predicts a distinct deviation from equilibrium conditions, with an increase in Si content and a decrease in eutectic temperature as the solidification front velocity increases.

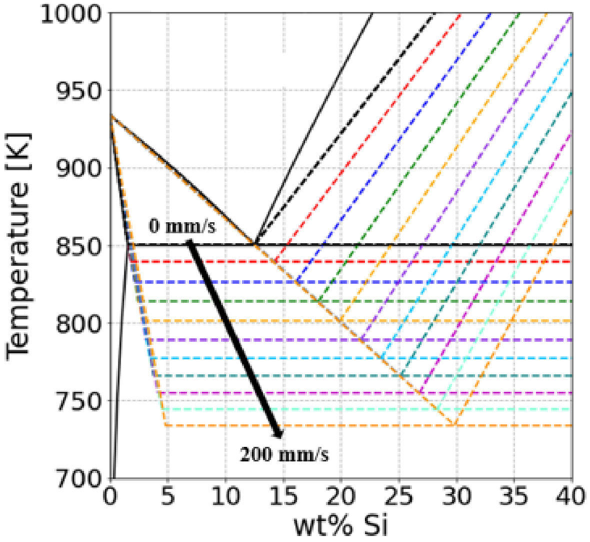

**Figure 79:** Modified Al-Si binary phase diagram for solidification front velocities ranging from 0 mm/s to 200 mm/s

*Figure 80A* and *Figure 80B* show a shift of eutectic composition and temperature from 12.5% to 29.8% and 850.5 $K$ to 734.1 $K$, respectively. This result is consistent with experiments made by S. Marola et al. [77] which has observed that an increase in growth velocity and the associated cooling rate for copper mould and selective laser melting processes result in a shift of the eutectic point towards higher Si content. Furthermore*, Figure 80C* show that the solubility of silicon in aluminium increases from ~1.6% to ~4.8%. This result supports that higher SFV result in solute trapping which lead to the super-saturation of the primary aluminium phase.

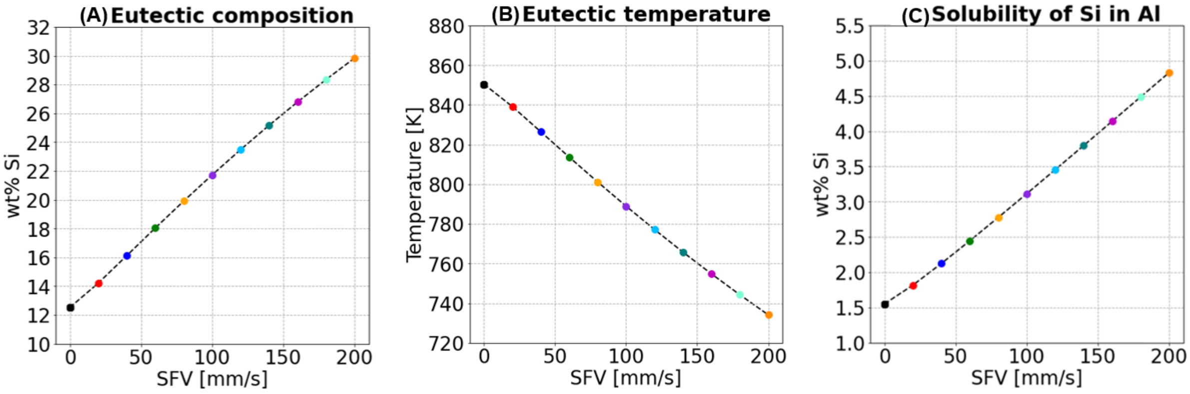

**Figure 80:** Predicted effect of the solidification front velocity on the eutectic composition (A), the eutectic temperature (B) and the maximum solubility of silicon in aluminium (C)

### 3.3.2 ACCURACY OF THE RAPID SOLIDIFICATION MODEL

To evaluate the accuracy of the proposed model, the lever rule and adjusted liquid phase composition were applied to assess the distribution and composition of the α-Al and eutectic phases. *Figure* 81 shows the estimated eutectic fractions as a function of solidification front velocity, using the modified phase diagram and the adjusted liquid composition. The experimental adjusted eutectic area fractions of 52.4% for Aural™-2 and 40.0% for Aural™-5 correspond to solidification front velocities of approximately 90 mm/s and 55 mm/s, respectively. These findings align with the solidification front velocity (SFV) range predicted by Berman et al. [28] for HPDC Mg alloys.

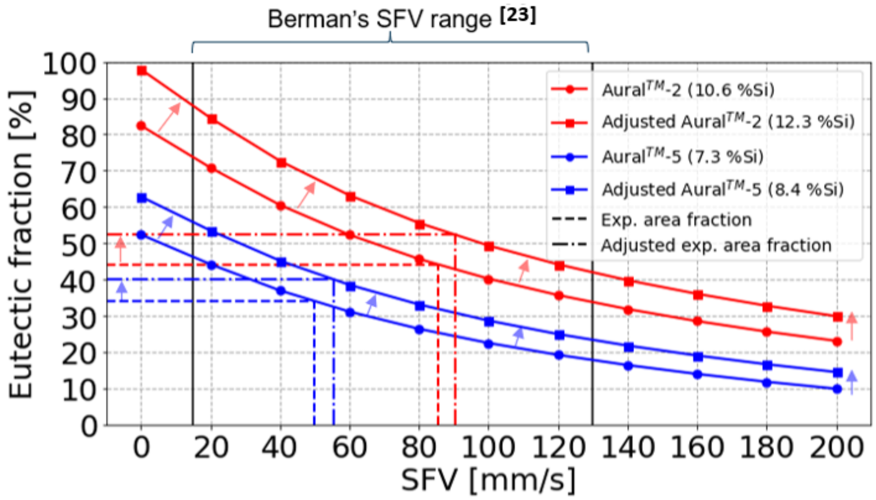

**Figure 81:** Eutectic fraction variation as a function of solidification front velocities ranging from 0 mm/s to 200 mm/s

The mass fraction calculation results presented in *Figure 82A* and *Figure 82B* demonstrate the shift in element distribution across the considered SFV range. The figures show a reduction in the eutectic aluminum content by 53.6 wt% for Aural™-2 and 37.5 wt% for Aural™-5, along with a decrease in silicon content by 3.1 wt% and 3.3 wt%, respectively. These findings suggest that the reduction in eutectic volume fraction observed in HPDC is largely due to the shift of aluminum content from the eutectic to the primary phase.

Conversely, there is an approximate increase of 3.1 wt% and 3.3 wt% in silicon content within the primary aluminum phase for Aural™-2 and Aural™-5. This shift supports the silicon trapping hypothesis and indicates that rapid solidification processes influence solute element diffusion. Based on these observations, the proposed rapid solidification model offers a more accurate prediction of constituent distribution associated with the Si alloying element in processes such as HPDC.

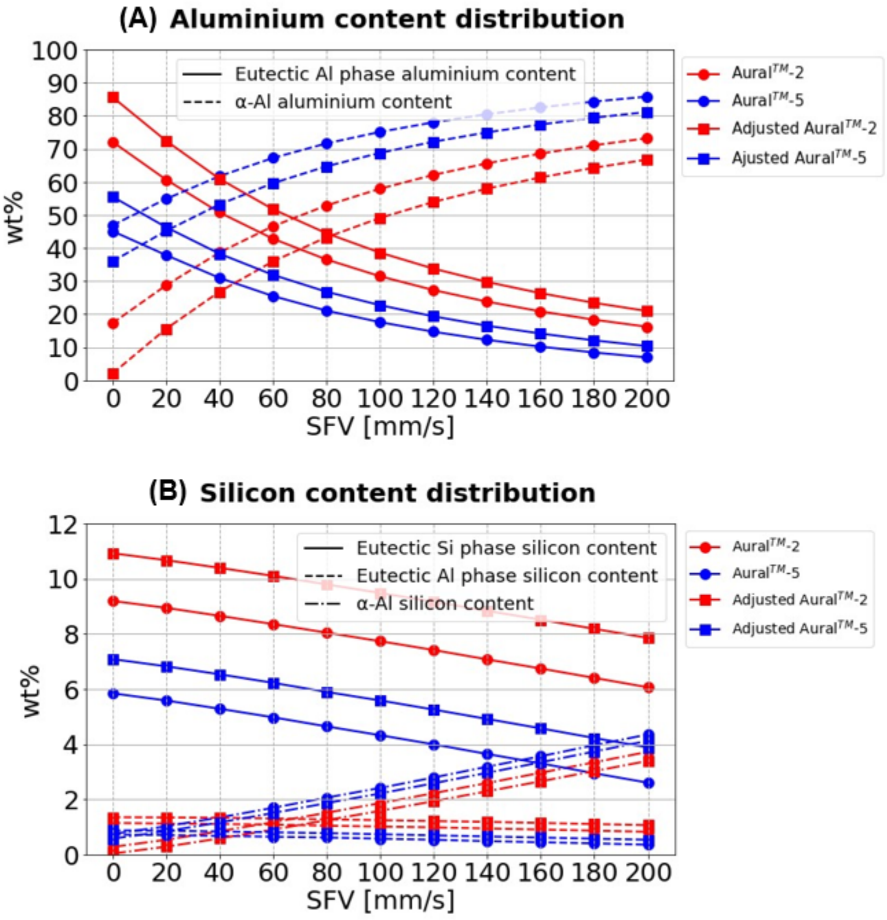

**Figure 82:** Main constituents' composition as a function of solidification front velocities ranging from 0 mm/s to 200 mm/s: (A) Aluminium content distribution and (B) Silicon content distribution

The estimated solidification front velocities in *Figure 81* for the alloys under study lead to a predicted maximum silicon solubility of 2.95% and 2.37% for Aural™-2 and Aural™-5, respectively. This higher predicted Si content compared to conventionally-solidified alloys is likely related to recent observations of nano Si clusters within aluminum grains in HPDC Al-Si alloys after heat treatment [78-81].

Similarly, the estimated solidification front velocities lead to predicted eutectic temperature depressions of 33.6℃ and 55.5℃ for Aural™-2 and Aural™-5, respectively. In other words, the model predicts eutectic solidification at temperatures significantly lower than conventional models.

### 3.3.3 EFFECT OF PRESSURE ON THE AL-SI PHASE DIAGRAM

While it is well-established that pressure influences solidification, rapid solidification does not necessarily involve the intense pressures characteristic of High-Pressure Die Casting (HPDC). Consequently, the primary focus has been on the solidification front velocity. However, it is important to assess the extent to which pressure may impact solidification, particularly in terms of shifting the eutectic point. HPDC involves very high transient pressures applied by the plunger ranging from 40 to 120 MPa during part of the solidification process. [82] *Figure 83* illustrates the influence of pressure on eutectic composition and temperature, compared to results obtained for the solidification front velocity (SFV) for the Al-Si system. It is evident that the pressure range encountered during stage 3 in HPDC is insufficient to significantly affect the eutectic composition, and thus cannot account for the phase proportion discrepancies observed between theory and practice. Pressure appears to have a notable impact only at values exceeding 1000 MPa.

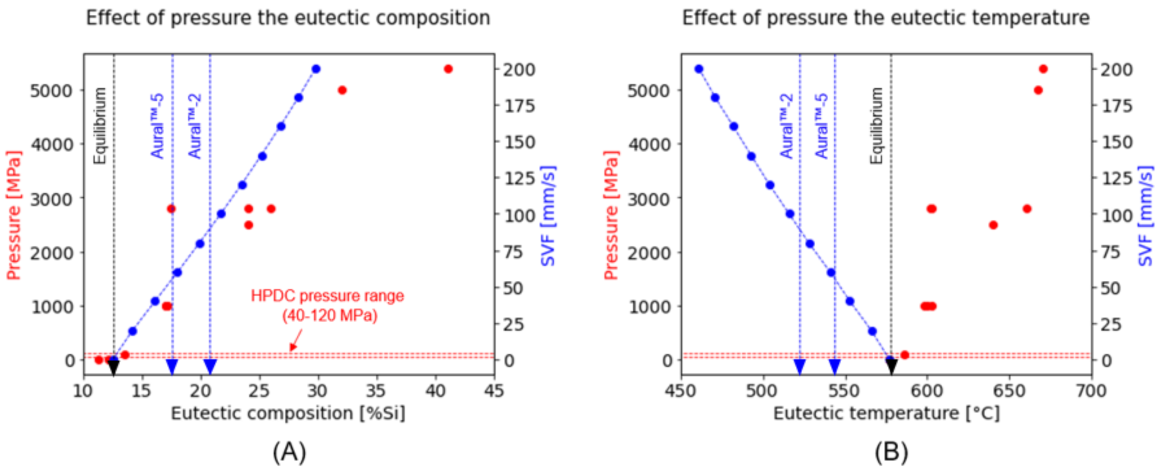

**Figure 83:** Comparison of the effect of pressure and solidification front velocity on the eutectic point. (A) effect on eutectic composition, (B) effect on eutectic temperature [83-87]

## 3.4 BENDING DUCTILITY PERFORMANCE

The metallographic observations in section 3.2 are particularly intriguing when considering bending performances, as the sub-surface microstructure is believed to have the most significant influence on this test. *Figure 84* presents VDA bending results grouped by zone for samples from all locations outlined in *Figure 63*. Results for samples in the gate zone are in red, center in yellow and close to the overflow in blue.Note that all results are measured angles, no correction was made to account for thickness.

For the ejector surface (*Figure 84A*), it is evident that bending performance improves along the material flow direction, as both the bending angle and the maximum load increase from the gate to the overflow. However, the results for the cover surface are more diffuse, with less clear distinctions between the zones (*Figure 84B*).

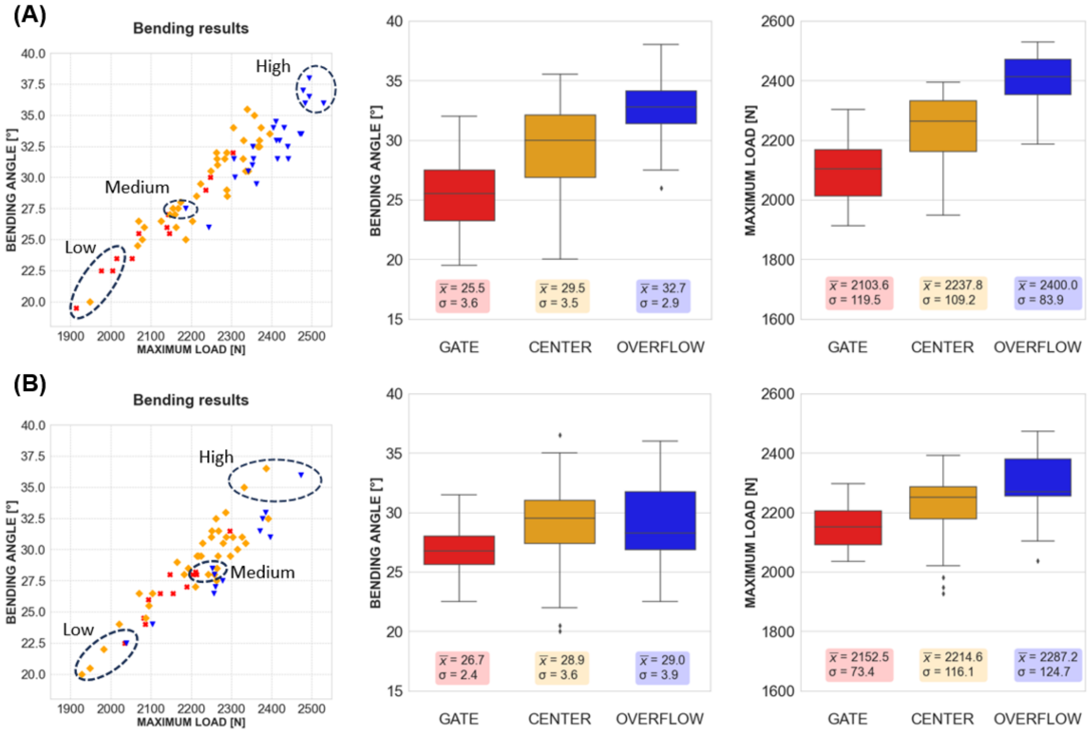

**Figure 84:** VDA bending results from specimen in all considered location: (A) show the performance within the ejector surface and (B) the cover surface

In an effort to evaluate the impact of sub-surface microstructure variations on bending results, we have identified three subsets of bent samples based on their bending performances (low, medium, high) for visual assessment. *Figure 85* presents representative micrographs for all three performance groups on both surfaces.

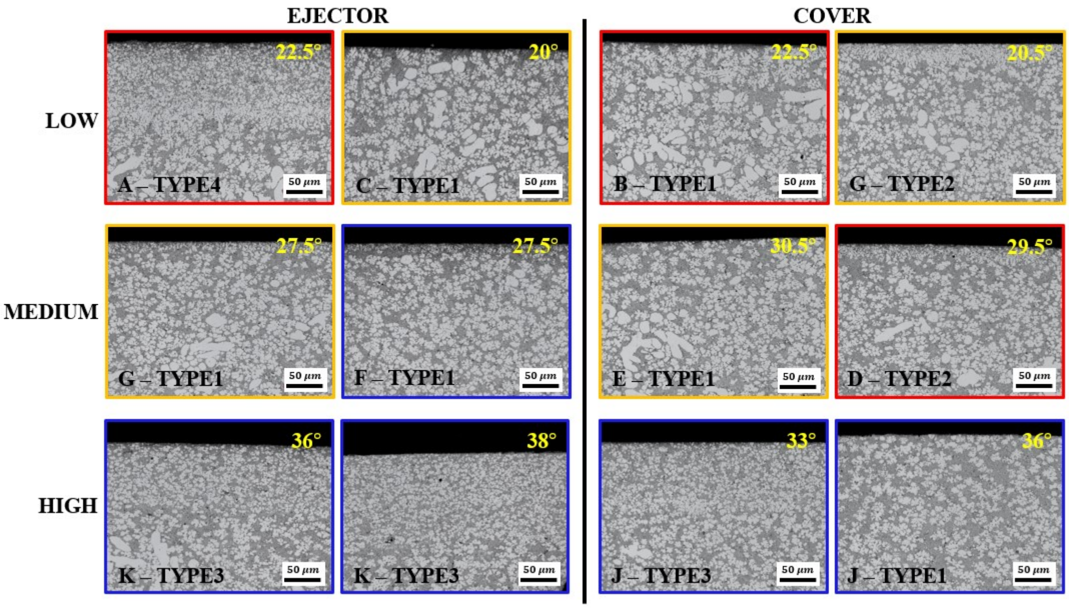

**Figure 85:** Representative sub-surface microstructure for all performance groups.

Optical microscopy observations have revealed that most lower and medium performance specimens exhibit an absence of sub-surface variation (type 1), making it challenging to distinguish between the two groups. However, it has been noted that some low-performance samples from the ejector surface display sub-surface variants 2 and 4 (*Figure 71* and *Figure 73*). Upon examining the micrographs presented in *Figure 86*, it appears that these types of sub-surface variants (type 2 and 4) are detrimental to bending performance. Metallographs in *Figure 86* also show lamination type of defects at the surface, which likely contributed to degraded bending performance. The propagation of cracks through the weak plane between the refined layer and the α-Al accumulation aligns with observations regarding the solidification sequence of the different layers. Furthermore, cracks originating from the α-Al-rich layer suggest that the compacted crystal structure is conducive to crack initiation.

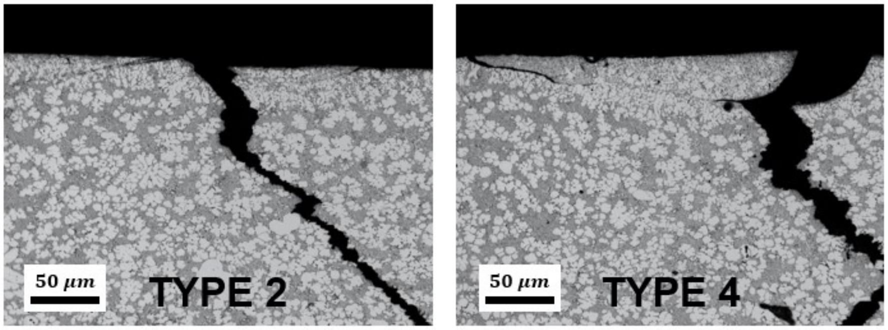

**Figure 86:** Micrograph showing the detrimental effect of the sub-surface variants 2 and 4 on crack propagation during VDA bending test

Many of the high-performance samples from the cover surface exhibit a consistent sub-surface variation characterized by a refined α-Al layer mixed with eutectic (*Figure 72,* Type 3). Conversely, high-performance specimens from the ejector surface display either a layer of refined α-Al or an absence of sub-surface variant. The subjective nature of identifying sub-surface microstructure variants alone is insufficient to fully explain the observed variations in bending performances across the plate since an absence of sub-surface variation has been observed in specimens from all performance groups. It is likely that the size and area fraction of the main constituents are more significant factors than the mere presence of a sub-surface variant. Therefore, in an effort to objectively characterize the sub-surface microstructure of each subset, the eutectic area fraction, average α-Al crystal area, and ESC area fraction have been calculated within the first 150 μm of each sample. Results from this analysis are presented in *Figure 87*, clearly illustrating a distinction between the performance groups. The low-performance group is characterized by a significant decline in eutectic content, a coarser α-Al phase, and a higher proportion of ESCs. Conversely, the medium-performance group exhibits a more stable eutectic content, a slightly finer α-Al phase, and considerably fewer ESCs.

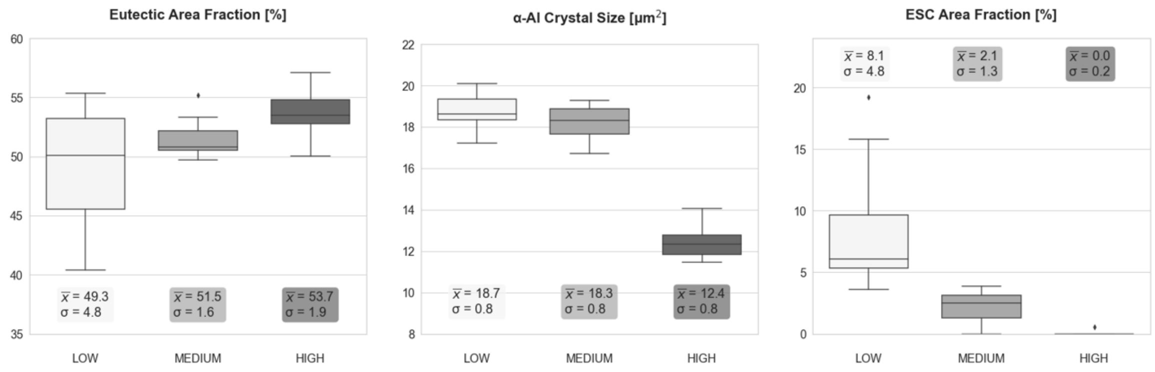

**Figure 87:** Main constituents' distribution within the first 150 $\mu m$ from the interface of both surfaces

All in all, the distinction between low and medium performance samples in terms of bending angle can be primarily attributed to the ESC content within the skin layer and the presence of detrimental sub-surface variants. Conversely, high-performance samples are characterized by a pronounced refinement of the α-Al phase mixed with eutectic (type 4) and an absence of ESCs. These findings suggest that the average size of α-Al crystals and the distribution of ESCs within the skin layer are the most influential factors affecting the homogeneity of bending performance across the plate.

## 3.5 RECOMMENDATIONS

### 3.5.1 RAPID SOLIDIFICATION MODEL

As demonstrated in this project, a phase diagram dependent on solidification front velocity appears to more accurately predict the eutectic fraction in HPDC than conventional solidification models. However, the proposed model has several limitations that need to be addressed in order to develop a comprehensive solution for the rapid solidification occurring inside the die cavity.

From a modeling perspective, the linearization of the liquidus and solidus curves introduces inaccuracies when predicting phase compositions, particularly above the eutectic point (both temperature and composition). Additionally, since the model is adapted to rapid dendritic growth, it cannot predict solidification patterns below the eutectic isotherm. Moreover, as the model is limited to the binary Al-Si system, it is not suitable for the solidification of intermetallic compounds. Although silicon is the major alloying element in the alloys under investigation (Aural™-2 and Aural™-5), other elements such as magnesium and manganese also play a critical functional role on service properties through their impact on precipitation (age hardening) and intermetallics. The model investigated herein focuses on silicon only, and extension would be required to better capture the heterogeneous distributions of other alloying elements in as-cast microstructures

Another point of interest is that eutectic temperature depression at high solidification velocities also has implications on HPDC process modelling. Most commercial simulations use equilibrium or Scheil calculations to describe the alloy. Conditions leading to a decreased eutectic temperature could change the enthalpy and solid fraction curves as a function of temperature, and therefore the predicted flowability. Integrating the proposed model in large-scale HPDC flow simulations was however out of the scope of the current study.

Finally, to test the generality of the model, the first step would be to test it with hypereutectic alloys and other binary systems, such as Al-Mg. The next step would involve developing appropriate equations to account for different growth morphologies, thus enabling the inclusion of eutectic and intermetallic solidification in the model. Finally, while challenging, experimental evaluation of the actual solidification front velocities during the process will be crucial for accurately assessing the model's performance.

### 3.5.2 SUBSURFACE MICROSTRUCTURE FORMATION

The results presented in this project clearly demonstrate the significant influence of the local subsurface microstructure on the mechanical performance of the casting in bending. Additionally, the characterization method used can effectively identify local changes in the main constituents within the microstructure, allowing for the identification of various subsurface variants present within a casting. However, while an exploratory effort was made on irregular geometries, most of the results in this work were based on simple flat plate castings. Replicating the study with more complex or larger castings could help validate the range of subsurface variants that can result from HPDC.

Beyond characterization, the next step in improving casting quality is to gain a deeper understanding of melt-die behavior. The local conditions that drive the solidification of the observed subsurface microstructure variants are not yet fully understood and quantification remains experimentally challenging. In practice, evaluating in-cavity conditions during the process is both challenging and costly. However, numerical simulation offers a promising solution, enabling valuable insights into the solidification conditions within the die, particularly at the die-melt interface. Exploring numerical models could help identify critical parameters—such as temperature, pressure, velocity, and heat flux—that influence the formation of various subsurface microstructure variants.

# CONCLUSION

## The eutectic area fraction in HPDC

The objective of this thesis was to address two critical problematics relating to the HPDC process of Al-Si aluminium alloys. The first problematic aimed at providing a model to better predict the eutectic fraction resulting from HPDC as the experimental results showed a discrepancy up to 40% with the conventional solidification models (equilibrium and Scheil). The study first focused on the rapid solidification of Aural™-2 and Aural™-5 alloys from thin-walled high-pressure vacuum die cast plates. The Al-Si eutectic fraction in the as-cast AlSiMnMg alloys was assessed using optical and scanning electron microscopy techniques, alongside analytical modeling of rapid solidification.

Key conclusions from the study include:

1. Conventional solidification models are inadequate to predict eutectic fractions for rapid solidification processes such as HPDC
2. Utilizing an SFV-dependent partition coefficient to calibrate the model significantly improves the accuracy of predicting the Al-Si eutectic fraction.
3. The observed reduction in eutectic content during rapid solidification is attributed to a substantial shift of aluminum from the eutectic to the primary constituents.
4. Accurate estimation of the eutectic fraction at the design stage remains challenging due to the current limitations in predicting local solidification front velocities.
5. The range of SFV over which the proposed method is applicable remains unclear due to experimental constraints.

Finally comparison of the conventional as well as two rapid solidification models based on planar and dendritic growth also highlights the lack of a general model suitable for a wide range of conditions, such as those encountered during a single cycle in high-pressure die casting.

### The influence of sub-surface variation on bending ductility

Local variations within the as-cast microstructure of an HPVDC plate were investigated with specific focus on the near-surface regions. The aim was to characterize possible sub-surface microstructure variants within a single plate and assess their influence on local bending performances.

While the specimens were simple flat plates, the process still generated a variety of near-surface characteristics. The following conclusions can be drawn on the influence of sub-surface variants on bending performances:

1. The presence of ESCs in the skin layer negatively impacts local bending performance.
2. Sub-surface variants with a refined layer of α-Al mixed with eutectic contribute to enhanced bending performance.
3. The α-Al rich layer has detrimental consequences, promoting crack initiation at the surface and within the sub-surface by creating a weak plane between the solid network present at the interface.
4. At a given location on the part, a subset of different sub-surface variants can be found in successive individual parts, highlighting the stochastic factors in die filling.

Based on these findings, sub-surface characteristics plays a clear role on the bending performances of HPVDC thin-walled components. As evidenced in the literature and the preliminary work herein on two irregular geometrical features, more complex geometries could lead to a wider range of microstructures as melt impact angles on the die cavity vary and the flow pattern becomes more intricate. Continued investigation on more representative prototypes or industrial scale specimens could refine our understanding of the mechanisms at play in microstructure formation. This knowledge could allow us to identify factors that could help predict, and eventually control, variations within a single component at the design and process setup stages.

## Publications

Results presented in the sections 3.1 and 3.2 are taken from a conference paper presented during the 2024 NADCA International Die Casting Congress and Exposition event [88]. In addition, the rapid solidification analysis is part of a journal paper currently undergoing the publication process.

# REFERENCES

[1] M. Guo, M. Sun, J. Huang, et S. Pang, "A comparative study on the microstructures and mechanical properties of Al-10Si-0.5 Mg alloys prepared under different conditions," *Metals*, vol. 12, no. 1, p. 142, 2022.

[2] G. G. Wang et J. Weiler, "Recent developments in high-pressure die-cast magnesium alloys for automotive and future applications," *Journal of Magnesium and Alloys*, vol. 11, no. 1, pp. 78-87, 2023.

[3] D. S. Cantú-Fernández, J. J. Taha-Tijerina, A. González, P. G. Hernández, et B. Quinn, "Mechanical Properties of a Structural Component Processed in High-Pressure Die Casting (HPDC) with a Non-Heat-Treated Aluminum Alloy," *Metals*, vol. 14, no. 3, p. 369, 2024.

[4] Q. Sun *et al.*, "Formation mechanism of the microstructural heterogeneity in a die-cast Al-Mg-Si alloy and its effect on mechanical properties," *Materials Characterization*, vol. 213, p. 114004, 2024.

[5] G. Timelli et A. Fabrizi, "The effects of microstructure heterogeneities and casting defects on the mechanical properties of high-pressure die-cast AlSi9Cu3 (Fe) alloys," *Metallurgical and Materials Transactions A*, vol. 45, pp. 5486-5498, 2014.

[6] H. Zheng, Y. Jiang, F. Liu, et H. Zhao, "Microstructure heterogeneity optimization of HPDC Al-Si-Mg-Cu alloys by modifying the characteristic of externally solidified crystals," *Journal of Alloys and Compounds*, vol. 976, p. 173167, 2024.

[7] H. Laukli, O. Lohne, S. Sannes, H. Gjestland, et L. Arnberg, "Grain size distribution in a complex AM60 magnesium alloy die casting," *International Journal of Cast Metals Research*, vol. 16, no. 6, pp. 515-521, 2003.

[8] S. Otarawanna, C. Gourlay, H. Laukli, et A. Dahle, "Microstructure formation in AlSi4MgMn and AlMg5Si2Mn high-pressure die castings," *Metallurgical and Materials Transactions A*, vol. 40, pp. 1645-1659, 2009.

[9] V. der Automobilindustrie, "VDA 238-100 Plate Bending Test for Metallic Materials," *VDA: Berlin, Germany*, 2010.

[10] W. Kurz, D. Fisher, et M. Rappaz, "Fundamentals of solidification," 2023.

[11] T. Vossel, N. Wolff, B. Pustal, et A. Bührig-Polaczek, "Influence of die temperature control on solidification and the casting process," *International Journal of Metalcasting*, vol. 14, pp. 907-925, 2020.

[12] J. R. Davis, *Alloying: understanding the basics*: ASM international, 2001.

[13] F. N. Rhines, "Phase diagrams in metallurgy: their development and application," *(No Title)*, 1956.

[14] I. Nová, J. Machuta, et I. Skalický, "Influence of Pressure on Al-Si Alloys System," *Manufacturing Technology*, vol. 17, no. 4, pp. 543-549, 2017.

[15] S. H. Avner, *Introduction à la métallurgie physique*: Cégep de Trois-Rivières, 1987.

[16] S. D. McDonald, A. K. Dahle, J. A. Taylor, et D. H. StJohn, "Eutectic grains in unmodified and strontium-modified hypoeutectic aluminum-silicon alloys," *Metallurgical and materials transactions A*, vol. 35, pp. 1829-1837, 2004.

[17] M. Day et A. Hellawell, "The microstructure and crystallography of aluminium—silicon eutectic alloys," *Proceedings of the Royal Society of London. Series A. Mathematical and Physical Sciences*, vol. 305, no. 1483, pp. 473-491, 1968.

[18] K. Al-Omari, A. Roósz, A. Rónaföldi, et Z. Veres, "Effect of Forced Melt Flow on Al–Si Eutectic-Alloy Microstructures," *Crystals*, vol. 12, no. 5, p. 731, 2022.

[19] M. Li, N. Omura, Y. Murakami, I. Matsui, et S. Tada, "A comparative study of the primary phase formation in Al–7 wt% Si and Al–17 wt% Si alloys solidified by electromagnetic stirring processing," *Materials Today Communications*, vol. 24, p. 101146, 2020.

[20] M. J. Aziz, "Dissipation-theory treatment of the transition from diffusion-controlled to diffusionless solidification," *Applied physics letters*, vol. 43, no. 6, pp. 552-554, 1983.

[21] M. J. Aziz et T. Kaplan, "Continuous growth model for interface motion during alloy solidification," *Acta metallurgica*, vol. 36, no. 8, pp. 2335-2347, 1988.

[22] M. J. Aziz, "Model for solute redistribution during rapid solidification," *Journal of Applied Physics*, vol. 53, no. 2, pp. 1158-1168, 1982.

[23] M. Pierantoni, M. Gremaud, P. Magnin, D. Stoll, et W. Kurz, "The coupled zone of rapidly solidified Al□ Si alloys in laser treatment," *Acta metallurgica et materialia*, vol. 40, no. 7, pp. 1637-1644, 1992.

[24] R. Trivedi et E. Sunseri, "Non-plane front solidification," dans *Casting*: ASM International, 2008, pp. 299-306.

[25] S. Chandra et B. C. Rao, "A study of process parameters on workpiece anisotropy in the laser engineered net shaping (LENSTM) process," *Journal of Physics D: Applied Physics*, vol. 50, no. 22, p. 225303, 2017.

[26] W. Kurz, B. Giovanola, et R. Trivedi, "Theory of microstructural development during rapid solidification," *Acta metallurgica*, vol. 34, no. 5, pp. 823-830, 1986.

[27] R. Trivedi et W. Kurz, "Dendritic growth," *International Materials Reviews*, vol. 39, no. 2, pp. 49-74, 1994.

[28] T. D. Berman, Z. Yao, E. Deda, L. Godlewski, M. Li, et J. E. Allison, "Measuring and Modeling Microsegregation in High-Pressure Die Cast Mg–Al Alloys," *Metallurgical and Materials Transactions A*, vol. 53, no. 7, pp. 2730-2742, 2022.

[29] T. Kraft, M. Rettenmayr, et H. Exner, "An extended numerical procedure for predicting microstructure and microsegregation of multicomponent alloys," *Modelling and Simulation in Materials Science and Engineering*, vol. 4, no. 2, p. 161, 1996.

[30] M. Carrard, M. Gremaud, M. Zimmermann, et W. Kurz, "About the banded structure in rapidly solidified dendritic and eutectic alloys," *Acta metallurgica et materialia*, vol. 40, no. 5, pp. 983-996, 1992.

[31] G. Del Guercio *et al.*, "Cracking behaviour of high-strength AA2024 aluminium alloy produced by Laser Powder Bed Fusion," *Additive Manufacturing*, vol. 54, p. 102776, 2022.

[32] Y. Lui, W. B. Lee, et B. Ralph, "A reclassification of the die-filling stages in pressure die-casting processes," *Journal of materials processing technology*, vol. 57, no. 3-4, pp. 259-265, 1996.

[33] S. Gulizia, M. Jahedi, et E. Doyle, "Performance evaluation of PVD coatings for high pressure die casting," *Surface and Coatings Technology*, vol. 140, no. 3, pp. 200-205, 2001.

[34] A. I. N. Korti et S. Abboudi, "Effects of shot sleeve filling on evolution of the free surface and solidification in the high-pressure die casting machine," *International Journal of Metalcasting*, vol. 11, no. 2, pp. 223-239, 2017.

[35] J. Lo´ pez, F. Faura, J. Herna´ ndez, et P. Go´ mez, "On the critical plunger speed and three-dimensional effects in high-pressure die casting injection chambers," *J. Manuf. Sci. Eng.*, vol. 125, no. 3, pp. 529-537, 2003.

[36] Y. Zhou, Z. Guo, et S.-M. Xiong, "Effect of runner design on the externally solidified crystals in vacuum die-cast Mg-3.0 Nd-0.3 Zn-0.6 Zr alloy," *Journal of Materials Processing Technology*, vol. 267, pp. 366-375, 2019.

[37] A. Jalili Nikroo, M. Akhlaghi, et M. Ahmadi Najafabadi, "Simulation and analysis of flow in the injection chamber of die casting machine during the slow shot phase," *The International Journal of Advanced Manufacturing Technology*, vol. 41, pp. 31-41, 2009.

[38] S. Kohlstädta, M. Vynnyckya, S. Goekec, et A. Gebauer-Teichmannb, "On determining the critical velocity in the high-pressure die casting machine's shot sleeve using CFD,"

[39] Q.-l. Wang et S.-m. Xiong, "Vacuum assisted high-pressure die casting of AZ91D magnesium alloy at different slow shot speeds," *Transactions of Nonferrous Metals Society of China*, vol. 24, no. 10, pp. 3051-3059, 2014.

[40] T. Wang, J. Huang, H. Fu, K. Yu, et S. Yao, "Influence of process parameters on filling and feeding capacity during high-pressure die-casting process," *Applied sciences*, vol. 12, no. 9, p. 4757, 2022.

[41] X. Jiao *et al.*, "Influence of slow-shot speed on PSPs and porosity of AlSi17Cu2. 5 alloy during high pressure die casting," *Journal of Materials Processing Technology*, vol. 268, pp. 63-69, 2019.

[42] V. Tsoukalas, "The effect of die casting machine parameters on porosity of aluminium die castings," *International Journal of Cast Metals Research*, vol. 15, no. 6, pp. 581-588, 2003.

[43] T. Zhang, W. Yu, C. Ma, Y. Zhou, et S. Xiong, "Effects of runner design and pressurization on the microstructure of a high-pressure die cast Mg-3.0 Nd-0.3 Zn-0.6 Zr alloy," *International Journal of Minerals, Metallurgy and Materials*, vol. 29, no. 7, pp. 1310-1316, 2022.

[44] B.-S. Wang et S.-M. Xiong, "Effects of shot speed and biscuit thickness on externaly solidified crystals of high-pressure diet cast AM60B magnesium alloy," *Transactions of Nonferrous Metals Society of China*, vol. 21, no. 4, pp. 767-772, 2011.

[45] P. Sharifi, J. Jamali, K. Sadayappan, et J. Wood, "Quantitative experimental study of defects induced by process parameters in the high-pressure die cast process," *Metallurgical and Materials Transactions A*, vol. 49, pp. 3080-3090, 2018.

[46] K. Dou, E. Lordan, Y. Zhang, A. Jacot, et Z. Fan, "A complete computer aided engineering (CAE) modelling and optimization of high pressure die casting (HPDC) process," *Journal of Manufacturing Processes*, vol. 60, pp. 435-446, 2020.

[47] M.-w. Wu, X.-b. Li, Z.-p. Guo, et S.-m. Xiong, "Effects of process parameters on morphology and distribution of externally solidified crystals in microstructure of magnesium alloy die castings," *China Foundry*, vol. 15, pp. 139-144, 2018.

[48] C. Bi, S. Xiong, X. Li, et Z. Guo, "Development of a fluid-particle model in simulating the motion of external solidified crystals and the evolution of defect bands in high-pressure die casting," *Metallurgical and Materials Transactions B*, vol. 47, pp. 939-947, 2016.

[49] A. R. Adamane, L. Arnberg, E. Fiorese, G. Timelli, et F. Bonollo, "Influence of injection parameters on the porosity and tensile properties of high-pressure die cast Al-Si alloys: a review," *International journal of metalcasting*, vol. 9, pp. 43-53, 2015.

[50] M. Ghomashchi, "High-pressure die casting: effect of fluid flow on the microstructure of LM24 die-casting alloy," *Journal of materials processing technology*, vol. 52, no. 2-4, pp. 193-206, 1995.

[51] D. Gunasegaram, B. Finnin, et F. Polivka, "Melt flow velocity in high pressure die casting: its effect on microstructure and mechanical properties in an Al–Si alloy," *Materials science and technology*, vol. 23, no. 7, pp. 847-856, 2007.

[52] S. Schneiderbauer, S. Pirker, C. Chimani, et R. Kretz, "Studies on flow characteristics at high-pressure die-casting," Dans *IOP Conference Series: Materials Science and Engineering*, 2012, vol. 27, no. 1, p. 012067: IOP Publishing.

[53] H. Cao, C. Shen, C. Wang, H. Xu, et J. Zhu, "Direct observation of filling process and porosity prediction in high pressure die casting," *Materials*, vol. 12, no. 7, p. 1099, 2019.

[54] S. Ji, Y. Wang, D. Watson, et Z. Fan, "Microstructural evolution and solidification behavior of Al-Mg-Si alloy in high-pressure die casting," *Metallurgical and Materials Transactions A*, vol. 44, pp. 3185-3197, 2013.

[55] X. Jiao *et al.*, "Characterization of externally solidified crystals in a high-pressure die-cast AlSi10MnMg alloy and their effect on porosities and mechanical properties," *Journal of Materials Processing Technology*, vol. 298, p. 117299, 2021.

[56] H. Laukli, L. Arnberg, et O. Lohne, "Effects of grain refiner additions on the grain structures in HPDC A356 castings," *International Journal of Cast Metals Research*, vol. 18, no. 2, pp. 65-72, 2005.

[57] T.-t. Zhang, W.-b. Yu, C.-s. Ma, W.-t. Chen, L. Zhang, et S.-m. Xiong, "The effect of different high pressure die casting parameters on 3D microstructure and mechanical properties of AE44 magnesium alloy," *Journal of Magnesium and Alloys*, vol. 11, no. 9, pp. 3141-3150, 2023.

[58] Z. Chen, "Skin solidification during high pressure die casting of Al–11Si–2Cu–1Fe alloy," *Materials Science and Engineering: A*, vol. 348, no. 1-2, pp. 145-153, 2003.

[59] M. Eslami, M. Payandeh, F. Deflorian, A. E. Jarfors, et C. Zanella, "Effect of segregation and surface condition on corrosion of rheo-HPDC Al–Si alloys," *Metals*, vol. 8, no. 4, p. 209, 2018.

[60] S. Otarawanna, C. Gourlay, H. Laukli, et A. Dahle, "Formation of the surface layer in hypoeutectic Al-alloy high-pressure die castings," *Materials Chemistry and Physics*, vol. 130, no. 1-2, pp. 251-258, 2011.

[61] S. Sulaiman, A. Hamouda, et D. Gethin, "Experimental investigation for metal-filling system of pressure diecasting process on a cold chamber machine," *Journal of Materials Processing Technology*, vol. 119, no. 1-3, pp. 268-272, 2001.

[62] S. Otarawanna, H. Laukli, C. Gourlay, et A. Dahle, "Feeding mechanisms in high-pressure die castings," *Metallurgical and Materials transactions A*, vol. 41, pp. 1836-1846, 2010.

[63] N. L. Veldman, A. K. Dahle, D. H. StJohn, et L. Arnberg, "Dendrite coherency of Al-Si-Cu alloys," *Metallurgical and Materials Transactions A*, vol. 32, pp. 147-155, 2001.

[64] L. Arnberg, G. Chai, et L. Backerud, "Determination of dendritic coherency in solidifying melts by rheological measurements," *Materials Science and Engineering: A*, vol. 173, no. 1-2, pp. 101-103, 1993.

[65] A. K. Dahle, Y. C. Lee, M. D. Nave, P. L. Schaffer, et D. H. StJohn, "Development of the as-cast microstructure in magnesium–aluminium alloys," *Journal of light metals*, vol. 1, no. 1, pp. 61-72, 2001.

[66] Q. Han et J. Zhang, "Fluidity of alloys under high-pressure die casting conditions: flow-choking mechanisms," *Metallurgical and Materials Transactions B*, vol. 51, pp. 1795-1804, 2020.

[67] C. M. Gourlay, A. K. Dahle, et H. I. Laukli, "Segregation band formation in Al-Si die castings," *Metallurgical and Materials Transactions A*, vol. 35, pp. 2881-2891, 2004.

[68] J. Beech et H. Jones, "Solidification Processing 1997," Dans *4 th Decennial International Conference on Solidification Processing*, 1997, p. 1997.

[69] G. A., "Digital twin integrating cell data for HPDC process modelling," présenté à Die Casting Congress & Exposition (NADCA), October 2 2024.

[70] S. G. Gariépy A. Tu, M.O. ; Samuel, E., "Local microstructure-properties model for HPVDC Aural™-2 using image analysis and machine learning," présenté à NADCA Die Casting Congress & Tabletop, MI, USA, September 13-15 2022.

[71] A. Ktari et M. El Mansori, "On the improvement of castings quality in hybrid low-pressure sand-casting (LPSC) process in a fully integrated CAE environment," *The International Journal of Advanced Manufacturing Technology*, vol. 127, no. 5, pp. 2309-2326, 2023.

[72] X. Jiao *et al.*, "Fracture behavior of a high pressure die casting AlSi10MnMg alloy with varied porosity levels," *Journal of Materials Research and Technology*, vol. 25, pp. 1129-1140, 2023.

[73] T. Ajantiwalay, R. Michi, C. Roach, A. Shyam, A. Plotkowski, et A. Devaraj, "Influence of microstructural heterogeneities on small-scale mechanical properties of an additively manufactured Al-Ce-Ni-Mn alloy," *Additive Manufacturing Letters*, vol. 3, p. 100092, 2022.

[74] D. W. Heard, J. Boselli, R. Rioja, E. A. Marquis, R. Gauvin, et M. Brochu, "Interfacial morphology development and solute trapping behavior during rapid solidification of an Al–Li–Cu alloy," *Acta materialia*, vol. 61, no. 5, pp. 1571-1580, 2013.

[75] Y. Tian, R. Gauvin, et M. Brochu, "Microstructure evolution and rapid solidification behavior of blended nickel-based superalloy powders fabricated by laser powder deposition," *Metallurgical and Materials Transactions A*, vol. 47, pp. 3771-3780, 2016.

[76] D. W. Heard, R. Gauvin, et M. Brochu, "Non-equilibrium solute partitioning in a laser re-melted Al–Li–Cu alloy," *Acta materialia*, vol. 61, no. 19, pp. 7432-7436, 2013.

[77] S. Marola *et al.*, "A comparison of Selective Laser Melting with bulk rapid solidification of AlSi10Mg alloy," *Journal of Alloys and Compounds*, vol. 742, pp. 271-279, 2018.

[78] M. Liu, H. Fu, L. Tian, W. Xiao, Q. Peng, et C. Ma, "Nucleation and growth mechanisms of nano-scaled Si precipitates in Al-7Si supersaturated solid solution," *Materials & Design*, vol. 121, pp. 373-382, 2017.

[79] R. Chen, Q. Xu, Z. Jia, et B. Liu, "Precipitation behavior and hardening effects of Si-containing dispersoids in Al–7Si–Mg alloy during solution treatment," *Materials & Design*, vol. 90, pp. 1059-1068, 2016

.

[80] F. Lasagni, B. Mingler, M. Dumont, et H. P. Degischer, "Precipitation kinetics of Si in aluminium alloys," *Materials Science and Engineering: A*, vol. 480, no. 1-2, pp. 383-391, 2008.

[81] K. Nakagawa, T. Kanadani, L. Anthony, et H. Hashimoto, "Microstructural changes at the initial stage of precipitation in an aluminum–silicon alloy," *Materials transactions*, vol. 46, no. 4, pp. 779-783, 2005.

[82] "NADCA Standards for high intergrity and structural die casting process," vol. 403, 2018.

[83] J. Murray et A. McAlister, "The Al-Si (aluminum-silicon) system," *Bulletin of alloy phase diagrams*, vol. 5, no. 1, pp. 74-84, 1984.

[84] H. Mii, M. Senoo, et I. Fujishiro, "Solid solubility of Si in Al under high pressure," *Japanese Journal of Applied Physics*, vol. 15, no. 5, p. 777, 1976.

[85] M. B. Djurdjević, S. Manasijević, Z. Odanović, et N. Dolić, "Calculation of liquidus temperature for aluminum and magnesium alloys applying method of equivalency," *Advances in materials science and engineering*, vol. 2013, no. 1, p. 170527, 2013.

[86] A. Batishev, "Solidification of metals and alloys under pressure," Cambridge, Cambridge International Science Publishers, 2002.

[87] A. Shinyaev, "Thermodynamic Calculation of Phase Equilibria in the Aluminum-Silicon System at High Pressures," *Zhur. Fiz. Khim.*, vol. 46, no. 11, pp. 2926-2928, 1972.

[88] X. Tremblay, A. Gariépy, et M. Javidani, "Influence of Subsurface Microstructure Variations on Bending Ductility of Aural™-2 HPVDC Thin-Walled Components," présenté à NADCA Die Casting Congress & Exposition, Indianapolis, 2024.